

# **Development of a range of air-to-air heat pipe heat recovery heat exchangers**

By

Alex Meyer

Thesis presented in partial fulfillment of the requirements for the degree  
Master of Science in Engineering at the University of Stellenbosch

Thesis supervisor: R.T. Dobson

September 2004

**Department of Mechanical Engineering**  
University of Stellenbosch

To my parents, Bill and Nina Meyer,  
For your unfailing love and support...

## DECLARATION

I, Alex Meyer, the undersigned, hereby declare that the work contained in this thesis is my own original work and has not previously, in its entirety or in part, been submitted at any university for a degree.

.....

Signature of Candidate

..... day of ..... 2004

## ABSTRACT

As the demand for less expensive energy is increasing world-wide, energy conservation is becoming a more-and-more important economic consideration. In light of this, means to recover energy from waste fluid streams is also becoming more-and-more important. An efficient and cost effective means of conserving energy is to recover heat from a low temperature waste fluid stream and use this heat to preheat another process stream. Heat pipe heat exchangers (HPHEs) are devices capable of cost effectively salvaging wasted energy in this way.

HPHEs are liquid-coupled indirect transfer type heat exchangers except that the HPHE employs heat pipes or thermosyphons as the major heat transfer mechanism from the high temperature to the low-temperature fluid. The primary advantage of using a HPHE is that it does not require an external pump to circulate the coupling fluid. The hot and cold streams can also be completely isolated preventing cross-contamination of the fluids. In addition, the HPHE has no moving parts.

In this thesis, the development of a range of air-to-air HPHEs is investigated. Such an investigation involved the theoretical modelling of HPHEs such that a demonstration unit could be designed, installed in a practical industrial application and then evaluated by considering various financial aspects such as initial costs, running costs and energy savings.

To develop the HPHE theoretical model, inside heat transfer coefficients for the evaporator and condenser sections of thermosyphons were investigated with R134a and Butane as two separate working fluids. The experiments on the thermosyphons were undertaken at vertical and at an inclination angle of  $45^\circ$  to the horizontal. Different diameters were considered and evaporator to condenser length ratios kept constant. The results showed that R134a provided for larger heat transfer rates than the Butane operated thermosyphons for similar temperature differences despite the fact that the latent heat of vaporization for Butane is higher than that of R134a. As an example, a R134a charged thermosyphon yielded heat transfer rates in the region of 1160 W whilst the same thermosyphon charged with Butane yielded heat transfer rates in the region of 730 W at  $23^\circ\text{C}$ .

Results also showed that higher heat transfer rates were possible when the thermosyphons operated at 45°. Typically, for a thermosyphon with a diameter of 31.9 mm and an evaporator to condenser length ratio of 0.24, an increase in the heat transfer rate of 24 % could be achieved.

Theoretical inside heat transfer coefficients were also formulated which were found to correlate reasonably well with most proposed correlations. However, an understanding of the detailed two-phase flow and heat transfer behaviour of the working fluid inside thermosyphons is difficult to model. Correlations proposing this behaviour were formulated and include the use of R134a and Butane as the working fluids. The correlations were formulated from thermosyphons of diameters of 14.99 mm, 17.272 mm, 22.225 mm and 31.9 mm. The evaporator to condenser length ratio for the 31.9 mm diameter thermosyphon was 0.24 whilst the other thermosyphons had ratios of 1. The heat fluxes ranged from 1800-43500 W/m<sup>2</sup>. The following theoretical inside heat transfer coefficients were proposed for vertical and inclined operations

$$\phi = 90^\circ \quad h_{ei} = 3.4516 \times 10^5 Ja^{-0.855} Ku^{1.344}$$

$$\phi = 45^\circ \quad h_{ei} = 1.4796 \times 10^5 Ja^{-0.993} Ku^{1.3}$$

$$\phi = 90^\circ \quad h_{ci} = 4.61561 \times 10^9 Re_i^{0.364} \left[ k_l / \left[ \frac{v_l^2}{g} \left( \frac{\rho_l}{\rho_l - \rho_v} \right) \right]^{1/3} \right]^{-2.05}$$

$$\phi = 45^\circ \quad h_{ci} = 3.7233 \times 10^{-5} Re_i^{0.136} \left[ k_l / \left[ \frac{v_l^2}{g} \left( \frac{\rho_l}{\rho_l - \rho_v} \right) \right]^{1/3} \right]^{1.916}$$

The theoretically modelled demonstration HPHE was installed into an existing air drier system. Heat recoveries of approximately 8.8 kW could be recovered for the hot waste stream with a hot air mass flow rate of 0.55 kg/s at an inlet temperature of 51.64 °C and outlet temperature of 35.9 °C in an environment of 20 °C. Based on this recovery, energy savings of 32.18 % could be achieved and a payback period for the HPHE was calculated in the region of 3.3 years.

It is recommended that notwithstanding the accuracies of roughly 25 % achieved by the theoretically predicted correlations to that of the experimental work, performance

parameters such as the liquid fill charge ratios, the evaporator to condenser length ratios and the orientation angles should be further investigated.

## OPSOMMING

As gevolg van die groeiende aanvraag na goedkoper energie, word die behoud van energie 'n al hoe belangriker ekonomiese oorweging. Dus word die maniere om energie te herwin van afval-vloeierstrome al hoe meer intensief ondersoek. Een effektiewe manier om energie te herwin, is om die lae-temperatuur-afval-vloeierstroom (wat sou verlore gaan) se hitte te gebruik om 'n ander vloeierstroom mee te verhit. Hier dien dit dan as voorverhitting van die ander, kouer, vloeierstroom. Hittepyp hitteruilers (HPHR's) is lae-koste toestelle wat gebruik kan word vir hierdie doel.

'n HPHR is 'n vloeistof-gekoppelde indirekte-oordrag hitteruiler, behalwe vir die feit dat dié hitteruiler gebruik maak van hittepype (of hittebuise) wat die grootste deel van sy hitteoordragsmeganisme uitmaak. Die primêre voordele van 'n HPHR is dat dit geen bewegende dele het nie, die koue- en warmstrome totaal geïsoleer bly van mekaar en geen eksterne pomp benodig word om die werkvloeier mee te sirkuleer nie.

In hierdie tesis word 'n ondersoek gedoen oor die ontwikkeling van 'n bestek van lug-tot-lug HPHR's. Hierdie ondersoek het die teoretiese modellering van so 'n HPHR geverg, sodat 'n demonstrasie eenheid ontwerp kon word. Hierdie demonstrasie eenheid is geïnstalleer in 'n praktiese industriële toepassing waar dit geëvalueer is deur na aspekte soos finansiële voordele en energie-besparings te kyk.

Om die teoretiese HPHR model te kon ontwikkel, moes daar gekyk word na die binne-hitteoordragskoëffisiënte van die verdamper- en kondensordeursneë, asook R134a en Butaan as onderskeie werksvloeiers. Die eksperimente met die hittebuis is gedoen in die vertikale en 45° (gemeet vanaf die horisontaal) posisies. Verskillende diameters is ook ondersoek, maar met die verdamper- en kondensor-lengteverhouding wat konstant gehou is. Die resultate wys dat R134a as werksvloeier in die hittebuis voorsiening maak vir groter hitteoordragstempo's in vergelyking met Butaan as werksvloeier by min of meer dieselfde temperatuur verskil – dít ten spyte van die feit dat Butaan 'n hoër latente-hitte-tydens-verdampings eienskap het. As voorbeeld gee 'n R134a-gelaaide hittebuis 'n hitteoordragstempo van omtrent 1160 W terwyl dieselfde hittebuis wat met Butaan gelaai is, slegs ongeveer 730 W lewer by 23 °C.

Die resultate wys ook duidelik dat hoër hitteoordragstempo's verkry word indien die hittebuis bedryf word teen 'n hoek van 45°. 'n Tipiese toename in hitteoordragstempo is ongeveer 24 % vir 'n hittebuis met 'n diameter van 31.9 mm en 'n verdamper- tot kondensor-lengteverhouding van 0.24.

Teoretiese binne-hitteoordragstempo's is ook geformuleer. Dié waardes stem redelik goed ooreen met die meeste voorgestelde korrelasies. Nieteenstaande die feit dat gedetailleerde twee-fase-vloei en die hitteoordragsgedrag van die werksvloei binne hittebuise nog nie goed deur die wetenskaplike wêreld verstaan word nie. Korrelasies wat hierdie gedrag voorstel is geformuleer en sluit weereens die gebruik van R134a en Butaan as werksvloeiërs in. Die korrelasies is geformuleer vanaf hittebuis met diameters van onderskeidelik 14.99 mm, 17.272 mm, 22.225 mm en 31.9 mm. Die verdamper- tot kondensor-lengteverhoudings vir die 31.9 mm deursnit hittebuis was 0.24 terwyl die ander hittebuise 'n verhouding van 1 gehad het. Die hitte-vloede het gewissel van 1800-45300 W/m<sup>2</sup>. Die volgende teoretiese geformuleerde binne-hitteoordragstempo's word voorgestel vir beide vertikale sowel as nie-vertikale toepassing

$$\phi = 90^\circ \quad h_{ei} = 3.4516 \times 10^5 Ja^{-0.855} Ku^{1.344}$$

$$\phi = 45^\circ \quad h_{ei} = 1.4796 \times 10^5 Ja^{-0.993} Ku^{1.3}$$

$$\phi = 90^\circ \quad h_{ci} = 4.61561 \times 10^9 Re_i^{0.364} \left[ k_l / \left[ \frac{v_l^2}{g} \left( \frac{\rho_l}{\rho_l - \rho_v} \right) \right]^{1/3} \right]^{-2.05}$$

$$\phi = 45^\circ \quad h_{ci} = 3.7233 \times 10^5 Re_i^{0.136} \left[ k_l / \left[ \frac{v_l^2}{g} \left( \frac{\rho_l}{\rho_l - \rho_v} \right) \right]^{1/3} \right]^{1.916}$$

Die wiskundig-gemodelleerde demonstrasie HPHR is geïnstalleer binne 'n bestaande lugdroër-sisteem. Drywing van om en by 8.8 kW kon herwin word vanaf die warm-afval-vloeiërstroming met 'n massa vloei van 0.55 kg/s teen 'n inlaattemperatuur van 51.64 °C en 'n uitlaattemperatuur van 35.9 °C binne 'n omgewing van 20 °C. Na aanleiding van hierdie herwinning, kan energiebesparings van tot 32.18 % verkry word. Die HPHR se installasiekoste kan binne 'n berekende tydperk van ongeveer 3.3 jaar gedolg word deur hierdie besparing.



Verdamper- tot kondensator-lengteverhouding, vloeistofvulverhouding en die oriëntasiehoek vereis verdere ondersoek, aangesien daar slegs 'n akkuraatheid van 25 % verkry is tussen teoretiese voorspellings en praktiese metings.

To my parents, Bill and Nina Meyer,  
For your unfailing love and support...

## ACKNOWLEDGEMENTS

First and foremost I would like to thank the Lord for helping me throughout my studying career. To my parents, for their unfailing love and support throughout my life. The opportunities you provided for me are sincerely appreciated.

To my promoter, Mr. R.T. Dobson, your help and support throughout the thesis are appreciated. I thank you for your drive in helping with the task without which the thesis could not have been completed.

To Mr. Dick Hübner, Mr. Theo von Driel and Mr. Christof Senk of Yucon Coil and Mr. Ralph Raad (Jr.) of Continental Fan Works (CFW): your financial support and willingness to help in the demonstration of a heat recovery system were invaluable in the completion of the thesis.

Finally, to Mr. C.J. Zietzman, your technical help, support and patience in the experimental set-ups are appreciated.

# TABLE OF CONTENTS

DECLARATION.....	I
ABSTRACT .....	II
OPSOMMING .....	V
ACKNOWLEDGEMENTS .....	IX
TABLE OF CONTENTS .....	X
LIST OF FIGURES .....	XIII
LIST OF TABLES.....	XVI
NOMENCLATURE .....	XVII
<b>1 INTRODUCTION.....</b>	<b>1.1</b>
<b>2 LITERATURE STUDY .....</b>	<b>2.1</b>
2.1 Historical Development of Heat Pipes.....	2.1
2.2 Thermosyphons.....	2.4
2.2.1 Thermosyphon characteristics .....	2.6
2.2.2 Performance limitations and critical parameters of thermosyphons.....	2.9
2.2.3 Applications.....	2.14
2.3 Heat Pipe Heat Exchangers (HPHEs).....	2.17
2.4 Air Drying.....	2.20
<b>3 THERMAL MODELING .....</b>	<b>3.1</b>
3.1 Single Thermosyphon .....	3.1
3.1.1 Heat transfer resistance across the evaporator and condenser walls.....	3.2
3.1.2 Evaporator internal heat transfer resistance .....	3.3
3.1.3 Condenser internal heat transfer resistance .....	3.6
3.1.4 Outside heat transfer resistance .....	3.9
3.2 Thermosyphon Heat Exchanger Model.....	3.10
3.2.1 Unfinned individual tube configuration.....	3.10
3.2.2 Plate finned tube bundle configuration .....	3.12
3.2.3 Plain individually finned tube configuration.....	3.15
3.3 Air Drier Model .....	3.17
<b>4 DESIGN OF A DEMONSTRATION HPHE.....</b>	<b>4.1</b>
4.1 Design Criteria and Specifications .....	4.1
<b>5 EXPERIMENTAL WORK .....</b>	<b>5.1</b>
5.1 Experimental Determination of the Thermosyphon Thermal Characteristics .....	5.1
5.1.1 Thermosyphon description.....	5.1
5.1.2 Thermosyphon experimental set-up .....	5.2

5.1.3	Thermosyphon experiments undertaken .....	5.9
5.2	Investigation into the Temperature Distribution of a HPHE .....	5.12
5.2.1	HPHE description.....	5.12
5.2.2	HPHE experimental set-up .....	5.13
5.2.3	HPHE experiments undertaken .....	5.16
5.3	Economic Analysis Experiments on a Demonstration HPHE .....	5.18
5.3.1	CFW/Yucon HPHE description .....	5.18
5.3.2	CFW/Yucon HPHE experimental set-up.....	5.18
5.3.3	CFW/Yucon HPHE experiments undertaken.....	5.20
5.4	Equipment, Instrumentation and Calibrations .....	5.22
5.4.1	Equipment and instrumentation used .....	5.22
5.4.2	Calibrations .....	5.23
<b>6</b>	<b>RESULTS .....</b>	<b>6.1</b>
6.1	General Experimental Results .....	6.1
6.1.1	Thermosyphon laboratory experiments .....	6.1
6.1.2	Demonstration experiments on the CFW/Yucon HPHE .....	6.3
6.2	Multi-Variable linear Regression Techniques for the Heat Transfer Coefficients .....	6.5
6.2.1	5/8"-Thermosyphon Results: R134a .....	6.5
6.2.2	3/4"-Thermosyphon Results: R134a .....	6.8
6.2.3	7/8"-Thermosyphon Results: R134a .....	6.9
6.2.4	5/4"-Thermosyphon Results: R134a .....	6.11
6.2.5	5/8"-Thermosyphon Results: Butane .....	6.13
6.2.6	3/4"-Thermosyphon Results: Butane .....	6.15
6.2.7	7/8"-Thermosyphon Results: Butane .....	6.17
6.2.8	5/4"-Thermosyphon Results: Butane .....	6.18
6.3	Performance Correlating Equations for Thermosyphons.....	6.20
6.4	Inside Temperature Distribution of a HPHE and Comparison with the Mathematical Model .....	6.27
6.5	Demonstration Experiments on the CFW/Yucon HPHE .....	6.30
<b>7</b>	<b>DISCUSSIONS AND CONCLUSIONS.....</b>	<b>7.1</b>
<b>8</b>	<b>RECOMMENDATIONS .....</b>	<b>8.1</b>
<b>9</b>	<b>REFERENCES.....</b>	<b>9.1</b>



# LIST OF FIGURES

<b>Figure 2.1</b> The Perkins Boiler (Lock, 1992) .....	2.1
<b>Figure 2.2</b> Thermosyphon heat exchanger proposed by Gay (Lock, 1992) .....	2.2
<b>Figure 2.3</b> Thermosyphon and heat pipe operation .....	2.5
<b>Figure 2.4</b> Closed and open thermosyphons .....	2.5
<b>Figure 2.5</b> Loop thermosyphon operation .....	2.6
<b>Figure 2.6</b> Heat transfer characteristics for different thermosyphons (Faghri, 1995) .....	2.7
<b>Figure 2.7</b> Typical thermosyphon chiller arrangement (Maidment and Eames, 2001) .....	2.16
<b>Figure 2.8</b> A commercial HPHE (Colmac Coil, 2000) .....	2.18
<b>Figure 2.9</b> A typical air drier unit .....	2.21
<b>Figure 3.1</b> Thermal resistance model of a thermosyphon .....	3.1
<b>Figure 3.2</b> The tube bundle configurations, (a) Aligned, (b) Staggered .....	3.10
<b>Figure 3.3</b> Plate finned tube bundle Configuration .....	3.13
<b>Figure 3.4</b> The Plate-and-tube Control Volume, (a) Plan View, (b) Cut-away View .....	3.13
<b>Figure 3.5</b> Plain individually finned tube configuration .....	3.16
<b>Figure 3.6</b> Plain Individually finned tube control volume .....	3.16
<b>Figure 3.7</b> The drier unit model and corresponding psychometric chart .....	3.19
<b>Figure 4.1</b> Row configuration for the CFW/Yucon HPHE .....	4.4
<b>Figure 4.2</b> Flow diagram for the HPHE computer simulation program .....	4.5
<b>Figure 5.1</b> The thermosyphon support structure .....	5.3
<b>Figure 5.2</b> Thermosyphon heating and cooling water tank systems .....	5.4
<b>Figure 5.3</b> Thermosyphon temperature measurement positions .....	5.5
<b>Figure 5.4</b> Connectivity of the charging device to the thermosyphon .....	5.6
<b>Figure 5.5</b> The charging device .....	5.6
<b>Figure 5.6</b> Connectivity of the charging device to the thermosyphon .....	5.7
<b>Figure 5.7</b> The thermosyphon experimental set-up .....	5.8
<b>Figure 5.8a</b> Experimental heat loss for the 5/8"-Thermosyphon .....	5.10
<b>Figure 5.8b</b> Experimental heat loss for the 3/4"-Thermosyphon .....	5.10
<b>Figure 5.9</b> Theoretical heat losses for the thermosyphons with $T_{amb} = 20\text{ }^{\circ}\text{C}$ .....	5.11
<b>Figure 5.10</b> The HPHE used in the inside temperature distribution experiments .....	5.13
<b>Figure 5.11</b> Temperature and velocity measurement matrix (front view) .....	5.14
<b>Figure 5.12a</b> The HPHE wind tunnel set-up .....	5.14
<b>Figure 5.12b</b> The HPHE wind tunnel set-up (side view) .....	5.15
<b>Figure 5.13</b> Theoretical heat losses for the HPHE .....	5.17
<b>Figure 5.14a</b> The HPHE installed onto the drier unit .....	5.19
<b>Figure 5.14b</b> The reducer sections from the HPHE to the ducting .....	5.19
<b>Figure 5.15</b> Theoretical heat losses for the demonstration HPHE .....	5.21
<b>Figure 5.16</b> Calibration curve for the charge measuring device .....	5.23
<b>Figure 6.1</b> Typical measured temperatures and heat transfer rates for the 3/4"-Thermosyphon .....	6.2
<b>Figure 6.2</b> Measured temperatures and heat transfer rates for the laboratory tested HPHE .....	6.3
<b>Figure 6.3</b> Readings for the industrial testing of the CFW/Yucon HPHE .....	6.4

<b>Figure 6.4</b> Energy balances for the 5/8"-Thermosyphon operating with R134a charged at 50 % liquid fill charge ratio .....	6.6
<b>Figure 6.5</b> Energy balances and inside evaporator and condenser heat transfer coefficients for the 5/8"- Thermosyphon operating with R134a charged at 25 % and operating vertically and at 45° .....	6.7
<b>Figure 6.6</b> Energy balances and inside evaporator and condenser heat transfer coefficients for the 3/4"- Thermosyphon operating with R134a charged at 50 % and operating vertically and at 45° .....	6.9
<b>Figure 6.7</b> Energy balances and inside evaporator and condenser heat transfer coefficients for the 7/8"- Thermosyphon operating with R134a charged at 50 % and operating vertically and at 45° .....	6.11
<b>Figure 6.8</b> Energy balances and inside evaporator and condenser heat transfer coefficients for the 5/4" - Thermosyphon operating with R134a charged at 50 % and operating vertically and at 45° .....	6.13
<b>Figure 6.9</b> Energy balances and inside evaporator and condenser heat transfer coefficients for the 5/8"- Thermosyphon operating with Butane charged at 50 % and operating vertically and at 45° .....	6.14
<b>Figure 6.10</b> Energy balances and inside evaporator and condenser heat transfer coefficients for the 3/4"- Thermosyphon operating with Butane charged at 50 % and operating vertically and at 45° ..	6.16
<b>Figure 6.11</b> Energy balances and inside evaporator and condenser heat transfer coefficients for the 7/8"- Thermosyphon operating with Butane charged at 50 % and operating vertically and at 45° ..	6.17
<b>Figure 6.12</b> Energy balances and inside evaporator and condenser heat transfer coefficients for the 5/4"- Thermosyphon operating with Butane charged at 50 % and operating vertically and at 45° ..	6.19
<b>Figure 6.13</b> Energy balances for the combined thermosyphon data sets operating vertically and inclined	6.22
<b>Figure 6.14</b> Evaporator inside heat transfer coefficients for the combined thermosyphon data sets operating vertically and inclined .....	6.22
<b>Figure 6.15a</b> Comparison between theoretically determined evaporator inside heat transfer coefficients for vertical operation .....	6.23
<b>Figure 6.15b</b> Comparison between theoretically determined evaporator inside heat transfer coefficients for inclined operation .....	6.23
<b>Figure 6.16</b> Condenser inside heat transfer coefficients for the combined thermosyphon data sets operating vertically and inclined .....	6.25
<b>Figure 6.17a</b> Comparison between theoretically determined condenser inside heat transfer coefficients for vertical operation .....	6.26
<b>Figure 6.17b</b> Comparison between theoretically determined condenser inside heat transfer coefficients for inclined operation .....	6.26
<b>Figure 6.18</b> Maximum heat transfer rates for the combined thermosyphon data sets operating vertically and inclined charged .....	6.27
<b>Figure 6.19</b> Inside temperature distributions of the manifolded rows of the laboratory tested HPHE at different hot and cold air mass flow rates .....	6.28
<b>Figure 6.20</b> Comparison between the evaporator and condenser heat transfer rates and the mathematical model of the laboratory tested HPHE at different mass flow rates .....	6.29
<b>Figure 6.21</b> Heat recovery of the demonstration HPHE .....	6.30
<b>Figure 6.22</b> kWhr Meter Readings for the drier unit operation with and without the demonstration HPHE installed .....	6.32
<b>Figure 6.23</b> Drier unit inside temperatures with and without the HPHE installed .....	6.32



<b>Figure 6.24</b> Comparison between the mathematical model and experimentally determined heat transfer rates using the in-field CFW/Yucon HPHE .....	6.34
<b>Figure 7.1</b> Comparison between theoretically determined evaporator inside heat transfer coefficients (smaller copy of Figure 6.15).....	7.4
<b>Figure 7.2</b> Comparison between theoretically determined evaporator inside heat transfer coefficients (smaller copy of Figure 6.17).....	7.5
<b>Figure 7.3</b> Heat transfer rates for a HPHE at specified air mass flow rates compared to the mathematical model (copy of Figure 6.20b).....	7.6
<b>Figure 7.4</b> Comparison between the mathematical model and the experimentally determined heat transfer rates for the CFW/Yucon HPHE (Copy of Figure 6.24) .....	7.7
<b>Figure C.1</b> Main window for the HPHE computer program.....	C.1
<b>Figure C.2</b> Physical inputs for the HPHE computer program.....	C.2
<b>Figure C.3</b> Unfinned thermosyphon tube bank configuration for the HPHE computer program.....	C.3
<b>Figure C.4</b> Individually finned thermosyphon tube bank configuration for the HPHE computer program.....	C.3
<b>Figure C.5</b> Plate-and-tube bank configuration for the HPHE computer program.....	C.4
<b>Figure C.6</b> Error window for the HPHE computer program.....	C.4
<b>Figure C.7</b> Results window for the HPHE computer program.....	C.5
<b>Figure C.8</b> Main window for the air drier computer program.....	C.6
<b>Figure C.9</b> The physical inputs window for the air drier computer program.....	C.7
<b>Figure C.10</b> Results window for the air drier computer program.....	C.7

# LIST OF TABLES

<b>Table 2.1</b> HPHE configuration (Zhang and Zhuang, 2003).....	2.19
<b>Table 4.1</b> Design specifications for the CFW/Yucon HPHE.....	4.2
<b>Table 4.2</b> Design inputs for the CFW/Yucon HPHE.....	4.3
<b>Table 4.3</b> CFW/Yucon HPHE results from the computer simulation program.....	4.4
<b>Table 5.1</b> Detailed characteristics of the experimental thermosyphons .....	5.2
<b>Table 5.2</b> Characteristics of the HPHE .....	5.12
<b>Table 6.1</b> Average percentage differences of equation 6.34 and 6.35 with respect to correlations presented in Section 3.1.....	6.24
<b>Table 6.2</b> Demonstration of the attainable heat recovery .....	6.30
<b>Table 6.3</b> Energy savings for the installed CFW/Yucon HPHE .....	6.33
<b>Table A.1</b> Thermophysical properties of lighter fluid mixture.....	A.2
<b>Table B.1</b> Data values for a 3/4"-Thermosyphon experiment.....	B.1
<b>Table B.2</b> Data values for the laboratory HPHE experiments.....	B.9

# NOMENCLATURE

## Symbols

$A$	Area	[m <sup>2</sup> ]
$A_{fr}$	Frontal area of the tube bundle	[m <sup>2</sup> ]
$A_{cva}$	Area exposed to the air stream in control volume	[m <sup>2</sup> ]
$A_{cvc}$	Minimum free flow area of control volume	[m <sup>2</sup> ]
$A_{cvf}$	Fin surface area exposed to the air stream	[m <sup>2</sup> ]
$A_{cvfr}$	Frontal area of the control volume	[m <sup>2</sup> ]
$Bo$	Bond number, $d_i/\sqrt{\sigma/g(\rho_l - \rho_v)}$	
$C$	Wallis' constant, 0.8	
$C_k$	Kutateladze Constant, $\sqrt{3.2}$	
$c_p$	Specific heat	[J/kgK]
$C_w$	Empirically determined constant, 0.7-1	
$d$	Diameter	[m]
$e$	Fin height	[m]
$F$	Pressure factor	
$Fr$	Froude number, $[\dot{q}_e/\rho_l h_{fg}]^2 [\rho_l/d_i g(\rho_l - \rho_v)]$	
$f_\phi$	Inclination adjustment factor	
$f$	Correction factor, friction factor	
$f_p$	Enhancement factor	
$g$	Gravitational constant, 9.81	[m/s <sup>2</sup> ]
$G$	Mass velocity	[kg/m <sup>2</sup> s]
$h$	Heat transfer coefficient, Enthalpy	[W/m <sup>2</sup> K], [J/kg]
$h_{fg}$	Latent heat of vaporization	[J/kg]
$h_z$	Local heat transfer coefficient	[W/m <sup>2</sup> K]
$j$	Colburn factor	
$Ja$	Jacob number, $c_{pl}(T_w - T_{sat})/h_{fg}$	
$k$	Thermal conductivity, Mass transfer coefficient	[W/mK], [kg/sm <sup>2</sup> Pa]
$Ku$	Kutateladze number, $\dot{q}_e/\left[\rho_v h_{fg} (\sigma g(\rho_l - \rho_v)/\rho_v^2)^{0.25}\right]$	
$L$	Length	[m]
$L_m$	Bubble length scale	
$\dot{m}$	Mass flow rate	[kg/s]

$mf$	Mass fraction	[%]
$mv$	Volume fraction	%]
$M$	Merrit number, $\rho_l \sigma h_{fg} / \mu_l$	
$n$	Wall heat flux exponent	
$N_p$	Number of tubes per row	
$N_r$	Number of tube rows	
$N_u$	Nusselt number	
$\bar{N}_{ud}^{\geq 10}$	Nusselt number for 10 or more tube bank rows	
$\bar{N}_{ud}^{<10}$	Nusselt number for fewer than 10 tube bank rows	
$\bar{N}_{ud}^1$	Nusselt number for one row of tubes	
$\bar{N}_{uz}^*$	Local modified Nusselt number	
$N_{\mu f}$	Viscosity number	
$P$	Pressure	[Pa]
$P_f$	Fin Pitch	[m]
$P_L$	Dimensionless longitudinal pitch	
$Pr$	Prandtl number	
$P_T$	Dimensionless transverse pitch	
$P_{ws}$	Saturated water vapour pressure	[Pa]
$\dot{q}$	Heat flux	[W/m <sup>2</sup> ]
$\dot{Q}$	Heat transfer rate	[W]
$\dot{Q}_{elec}$	Electrical work	[W]
$\dot{Q}_{fan}$	Fan work	[W]
$\dot{Q}_{loss}$	Heat losses	[W]
$r$	Recirculation ratio	[%]
$R^2$	Correlation coefficient	
$R$	Thermal resistance, Gas constant	[°C/W],[kJ/(kmol.K)]
$R_a$	Rayleigh number	
$Re$	Reynolds number	
$Re_{\phi}$	Adjusted Reynolds number	
$s$	Spacing between two fins	[m]
$S_L$	Longitudinal pitch of tube bank	[m]
$S_t$	Transverse pitch of tube bank	[m]

$S_T$	Standton number	
$T$	Temperature	[°C]
$\bar{T}$	Average Temperature	[°C]
$t$	Wall thickness	[m]
$V$	Velocity, Volume	[m/s], [m <sup>3</sup> ]
$\bar{V}$	Adjusted velocity, Average velocity	[m/s]
$V^*$	Dimensionless superficial velocity	
$V^+$	Liquid fill ratio	[%]
$V_o$	Velocity of fluid in the empty cross section	[m/s]
$We$	Weber number, $\rho_1 V_l^2 L / \sigma$	
$X$	Dimensionless liquid pool parameter	

### ***Subscripts and superscripts***

$a$	Ambient
$air$	Dry Air
$aligned$	Aligned
$ave$	Average
$c$	Condenser, Cold
$cond$	Condenser
$crit$	Critical
$CC$	Combined Convection
$cface$	Condenser face
$cv$	Control Volume
$db$	Dry bulb
$e$	Evaporator, Exit
$eface$	Evaporator face
$evap$	Evaporator
$f$	Liquid, fin
$fo$	Fin outside
$h$	Hot, Hydraulic
$i$	Inside, inlet
$in$	Inlet
$KU$	Kutatededze
$l$	Liquid, length

<i>max</i>	Maximum
<i>NB</i>	Nucleate boiling
<i>NC</i>	Natural convection
<i>o</i>	Outside, outlet
<i>s</i>	surface
<i>sat</i>	Saturated
<i>stag</i>	Staggered
<i>tot</i>	Total
<i>v</i>	Vapour
<i>w</i>	Wall
<i>wb</i>	Wet bulb
<i>x</i>	Characteristic length

### ***Greek symbols***

$\sigma$	Area ratio, Surface tension, Stefan Boltzmann constant	[N/m], [W/m <sup>2</sup> K <sup>4</sup> ]
$\delta_z$	Film thickness	
$\psi$	Arrangement factor, Mixing pool coefficient, Dimensionless pitch factor	
$\phi$	Arrangement factor, Relative humidity, Inclination angle	[°]
$\rho$	Density	[kg/m <sup>3</sup> ]
$\Delta$	Difference	
$\eta$	Dimensionless film parameter, efficiency	[%]
$\mu$	Dynamic viscosity	[Ns/m <sup>2</sup> ]
$\chi$	Correction factor	
$\omega$	Humidity ratio at the dry bulb temperature	
$\omega_s$	Humidity ratio at the wet bulb temperature	
$\nu$	Kinematic viscosity, Specific volume	[m <sup>2</sup> /s], [m <sup>3</sup> /kg]

### ***Acronyms and Abbreviations***

Alt	Altitude above sea level	[m]
ANOVA	Analysis of variance	
Baro	Barometric pressure	[Pa]
COP	Coefficient of Performance	
ESDU	Engineering Sciences Data Unit	

HPHE	Heat Pipe Heat Exchanger
in	Inch = 25.4 mm
TEG	Triethylene glycol
s/s	Stainless Steel

# 1 INTRODUCTION

Owing to ever increasing demands for global energy savings, South African Companies are seeking to improve their international competitive edge by developing new systems whereby wasted energy can be efficiently recovered. For this reason, heat recovery systems are becoming increasingly important. Yucon, a large refrigeration heat exchanger manufacturer deemed it strategically important to meet this challenge by investigating the possibility of increasing their existing product range by adding to it the option of heat pipe (thermosyphon) heat recovery systems. The express objective of this thesis is therefore to meet this company's product development requirements.

Successful implementation in the design of a heat pipe heat exchanger (HPHE) requires detailed knowledge of the heat transfer characteristics. The development of theoretical inside heat transfer coefficients and the maximum heat transfer rates for different thermosyphon working fluids based on experimental data and on the physical behaviour of the working fluid are important to determine heat transfer characteristics. Furthermore, it is also important to investigate the performance parameters of the thermosyphons, such as the diameter and the evaporator to condenser length ratios so that an appropriate heat exchanger can be specified. Based on these performance parameters, a theoretical model is developed for a thermosyphon heat recovery system whereby, by altering the parameters, the size and predicted heat recoveries for a range of HPHE's can be developed.

HPHE's are used in many countries world-wide in a variety of applications. However, they have as yet not been accepted by the South African market. Continental Fan Works (CFW), a design and manufacture company specialising in drying systems and other air handling products were willing provide an opportunity to demonstrate the performance of such a HPHE. The objective is therefore to verify the economic viability of using such a heat recovery system in a practical industrial application. The economic evaluation of the demonstration unit is therefore considered and includes factors such as the initial costs, running costs and the energy savings of the HPHE.

A literature survey is conducted to give insight into heat pipes (thermosyphons) and HPHEs. The performance parameters and the characteristics that influence the



performance of thermosyphons were specifically studied. This survey is located in Section 2. The theory from which the theoretical model is developed is located in Section 3. Section 4 describes the design specifications for the demonstration HPHE and presents the results from the computer simulation program. Section 5 discusses the experimental design and set-ups and experimental procedures followed whilst Section 6 presents the results from the experimental work. The discussions and conclusions pertaining to the results in Section 6 are presented in Section 7 with recommendations given in Section 8.

## 2 LITERATURE STUDY

The modern day development of heat pipes and thermosyphons began with a journal entry by George Grover on July 24, 1963, in which a device capable of heat transfer via capillary movement of fluids was suggested. This device has since found uses in a variety of applications and popularity is ever-increasing worldwide. The historical development and essential characteristics of thermosyphons and heat pipes will be considered in this literature study.

### 2.1 Historical Development of Heat Pipes

The heat pipe concept was first introduced in the 1800's by patents formulated by A. M. Perkins and his son, J. Perkins. These men developed what is known as the Perkins tube, a device that works on the principle of using either single or two-phase processes to transfer heat from a furnace to a boiler. This device consists of a tube with an airtight space partially filled with water as the working fluid. In the space, boiling with the formation of vapour and liquid, condensation, and free convection heat and mass transfer between the boiling and condensation regions occurs. The earliest applications of these tubes were in locomotive boilers and in locomotive fire box super heaters. Figure 2.1 illustrates the Perkins boiler. In the Perkins boiler, one end of each tube projects downwards into the fire and the other part extends up into the water of the boiler. Any additional heat applied thereto will quickly rise to the upper parts of the tubes and be given off to the surrounding water contained in the boiler (Piro, 1997).

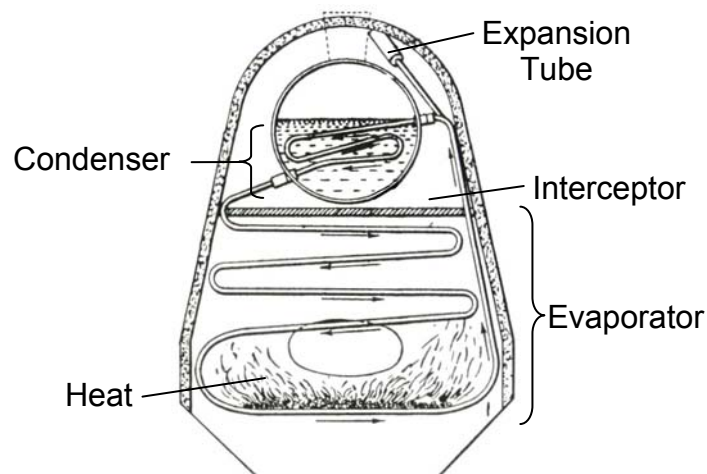


**Figure 2.1** The Perkins Boiler (Lock, 1992)

At a time when high pressure boilers were still experimental and their operation was plagued by scaling and fouling problems, the system proposed by Perkins represented excellence in design as tests verified that there was no leakage and no deposits of any kind occurring within the tube. In the patent taken out by Perkins' in 1892, mention is made of applications of the Perkins tube to waste heat recovery, where the heat is recovered from the exhaust gases from blast furnaces and other similar apparatus, and used to preheat incoming air.

Perkins' patents however neglected to include the use of external fins on the tubes to improve the tube-to-gas heat transfer. Gay introduced the fin concept and took out a patent in 1929, in which a number of finned Perkins tubes were situated vertically with the evaporator section below the condenser section (Dunn, 1994). A plate then sealed the passage between the exhaust and inlet air ducts as illustrated in Figure 2.2. It was this setup, which, with the introduction of capillary forces, laid the groundwork in the development of what is today known as a heat pipe (Peterson, 1994).

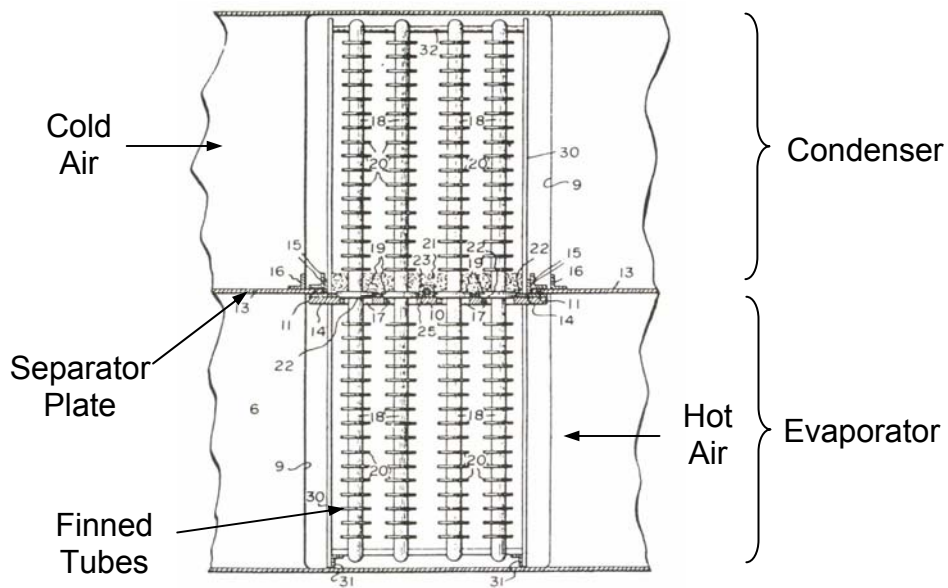


**Figure 2.2** Thermosyphon heat exchanger proposed by Gay (Lock, 1992)

Following the groundwork by Gay, Gaugler then envisioned a device which would evaporate a liquid at a point above the place where condensation would occur without requiring any additional work to move the liquid to the higher elevation and it was this idea, which led to the introduction of the heat pipe concept.

A heat pipe consists of a sealed pipe lined with a wicking structure in which a small amount of working fluid is present. A heat pipe can further be divided into two sections, namely, the evaporator or heat addition and condenser or heat rejection sections. When heat is added to the evaporator region, the working fluid present in the wicking structure is heated until it vaporizes. The pressure differences between the two regions then cause the vapour to flow to the cooler condenser section. The vapour then condenses in this section and gives up its latent heat of vaporization. The capillary forces in the wicking structure then *pump* the liquid back to the evaporator. Gaugler later introduced this principle of using a wicking structure to allow for large heat transfers with minimal temperature drops for applications in refrigeration engineering. However, the heat pipe proposed by Gaugler was not developed beyond the patent stage (Dunn, 1994).

In 1962 the heat pipe idea was resurrected by Trefethen in connection with high-temperature space power systems (Ivanovskii, 1982). Serious development then started in 1963 when the heat pipe was independently reinvented by Grover at Los Alamos National Laboratory in New Mexico. Grover demonstrated the heat pipes effectiveness as a high performance heat transmission device. Cotter's publication in 1965, in which the theoretical results and design tools were reported, is however responsible for the recognition of the heat pipe. Following this publication, research began worldwide (Faghri, 1995).

In 1968 Nozu (1969) described an air heater using a bundle of finned heat pipes. This later became known as a heat pipe heat exchanger (HPHE) and was of significant importance owing to the increasing interest in energy conservation and environmental protection world-wide. The exchanger could then be used to recover heat from hot exhaust gases and be applied in industrial and domestic air conditioning (Dunn, 1994). For the aforementioned reasons, these heat exchangers are the most widely known applications of heat pipes since the early 1990's.

## 2.2 Thermosyphons

Thermosyphons are essentially heat pipes without the wicking structure. They act as vapour-liquid heat conductors and are often regarded as a special type of heat pipe. The difference between the two is that the thermosyphon uses gravity to transfer heat from a heat source that is located below the cold sink. As a result, the evaporator section is situated below the condenser section. The working fluid evaporates, condenses in the condenser section and flows back to the evaporator section by means of gravity. Hence, the term 'gravity assisted heat pipe' is often used to describe the thermosyphon. It has been shown that in the presence of gravity, thermosyphons are preferred to heat pipes owing to the fact that the wicks in heat pipes produce an additional resistance to the flow of condensate. This extra resistance may reduce the heat fluxes in heat pipes by 1.2 to 1.5 times lower than those in thermosyphons (Pioro, 1997). In addition, the manufacture of heat pipes is more complicated and cost intensive.

In the thermosyphon, heat applied to the evaporator section is conducted through the pipe wall where it vaporises the working fluid. The pressure differences between the evaporator and condenser regions then cause the vapour to flow to the cooler condenser section. The vapour then condenses at this section and releases its latent heat of vaporization. The condensate then returns to the evaporator section by means of gravity where the process continues (Ivanovskii, 1982). This is a continuous process resulting in the transfer of heat from one zone to another. Figure 2.3 illustrates the principle difference between the heat pipe and the thermosyphon.

Thermosyphons can be categorised as either two-phase or single-phase flow devices. Single-phase refers to the pipe being filled with either a gas or liquid only. If the pipe was only filled with liquid, provision would have to be made to compensate for the expansion of the liquid when it is heated in order to maintain the inside pressure at acceptable levels. By introducing a liquid and its vapour into the pipe, the vapour compresses as the temperature increases. In addition, the heat transfer capability is considerably increased owing to the fact that the large latent heat mechanism of the working fluid can then be exploited.

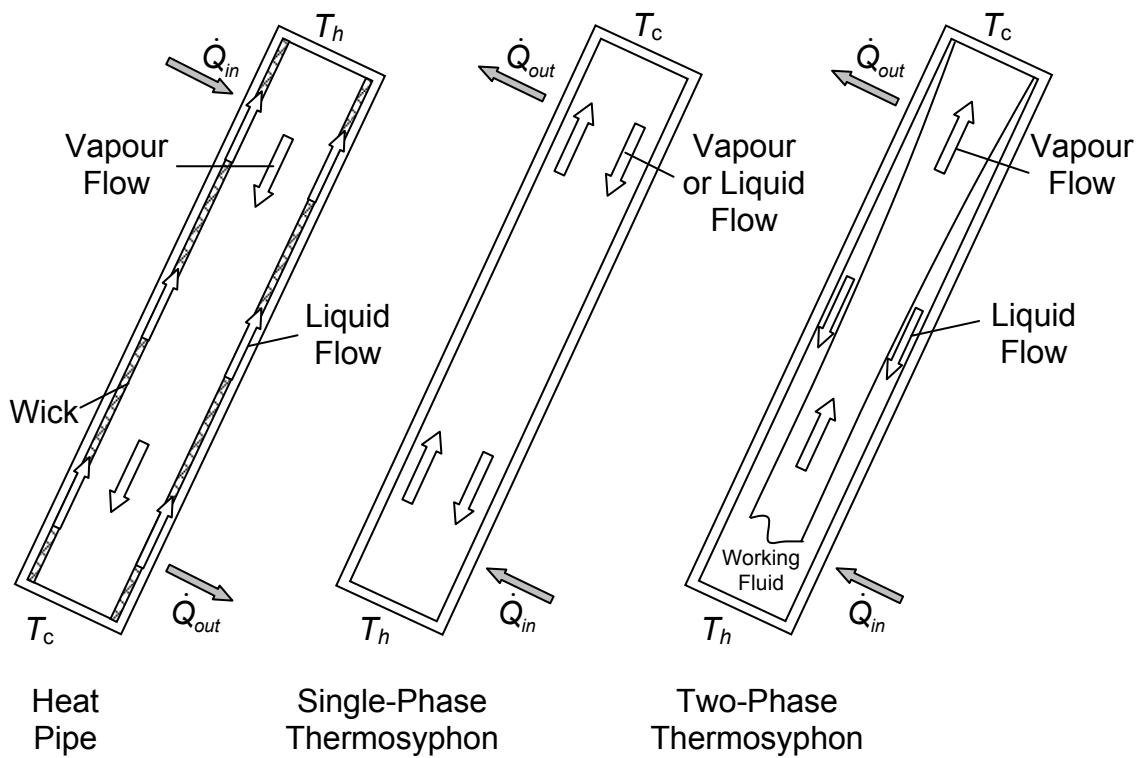


**Figure 2.3** Thermosyphon and heat pipe operation

In addition, thermosyphons can be either closed or open. The open thermosyphon does not have a condenser section and the working fluid is supplied continuously from the outside into the evaporator along the pipe as shown in Figure 2.4. These thermosyphons are primarily used for studying boiling processes inside thermosyphons. Closed thermosyphons may be evacuated or non-evacuated and can be supplied with heat from the sides and the end (Piro, 1997).

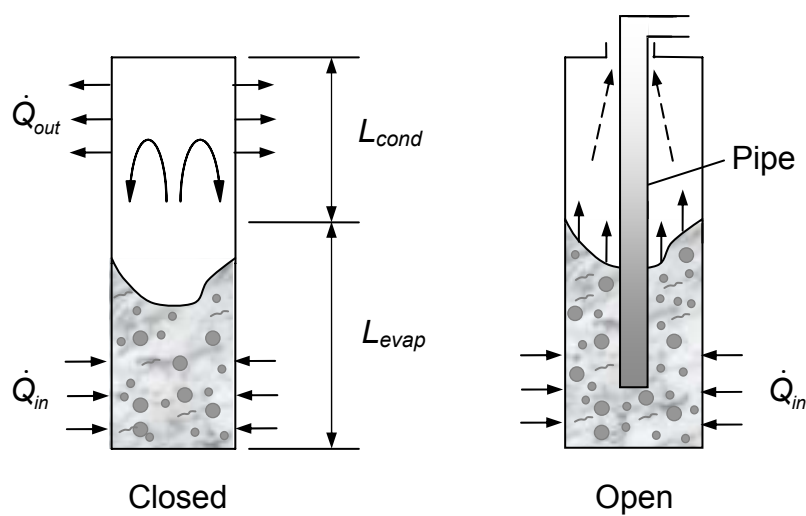


**Figure 2.4** Closed and open thermosyphons

Aerosyphons are also a variety of thermosyphons in which the heat flux is transmitted by forced convection of the liquid. This involves passing a saturated gas through the liquid, causing the liquid to bubble intensively helping stir the liquid. However, this type of thermosyphon has as yet no applications and is primarily used to investigate boiling heat transfer since the boiling process is simulated rather well (Lock, 1992).

When heat is applied to the evaporator, in a loop arrangement, the liquid evaporates and flows through the vapour transport line to the condenser zone, where heat is removed. This is then known as a loop thermosyphon illustrated in Figure 2.5. The liquid subsequently returns to the evaporator via a sub cooled liquid return line, which collapses any remaining vapour bubbles. Consequently, smooth wall tubing can be employed in the construction of the vapour and liquid transport lines as well as in the condenser zone as no wicking structure is needed. This avoids the liquid flow losses that would be apparent in a conventional heat pipe (Yun and Kroliczek, 2002).

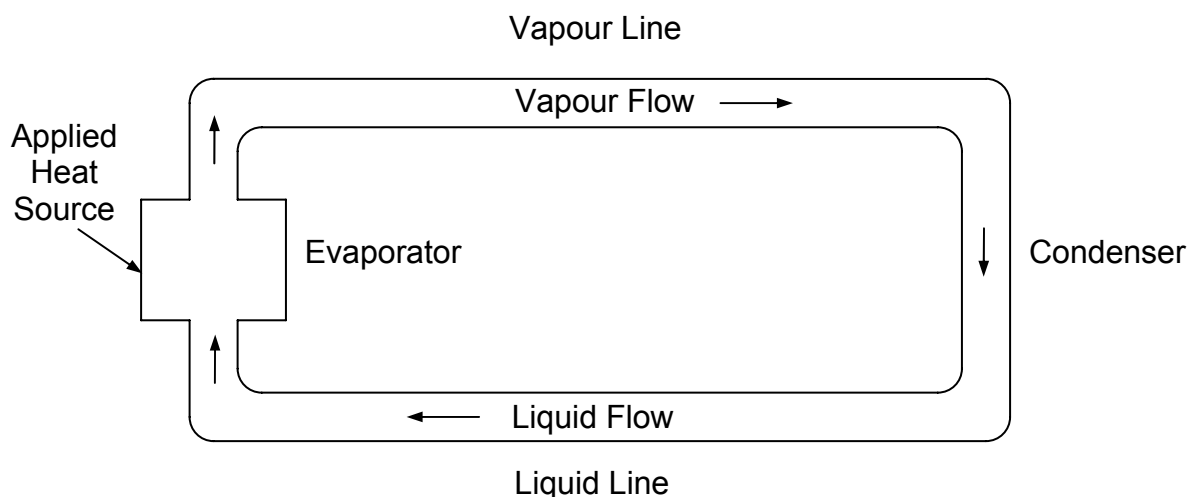


**Figure 2.5** Loop thermosyphon operation

### 2.2.1 Thermosyphon characteristics

One of the main reasons why thermosyphons are becoming ever more popular is the fact that they have a very high effective thermal conductance. As an example, these pipes are able to conduct up to 1000 times more heat, under favourable conditions, than copper in the same space and time (Russwurm, Part 1, 1980). Faghri (1995) illustrated this by comparing a copper rod of 25.4 mm OD and different thermosyphons. Figure 2.6 illustrates the heat transfer characteristics.

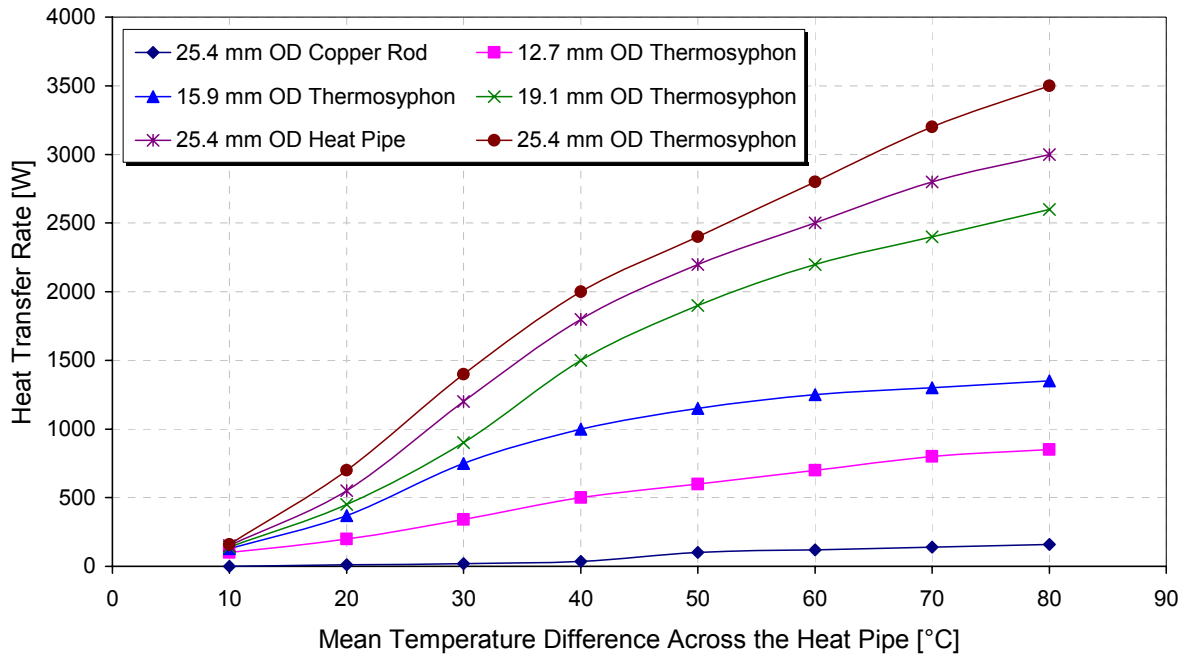


**Figure 2.6** Heat transfer characteristics for different thermosyphons (Faghri, 1995)

Thermosyphons also have the ability to act as a thermal flux transformer where energy can be added at a high heat flux rate to the pipe over a small surface area and removed over a larger surface area at a lower heat flux, or vice versa. In addition, thermal flux transformation ratios of 15 to 1 can be achieved using thermosyphons (Faghri, 1995). By determining the conditions at the condenser, the thermosyphon can be designed to keep a nearly constant temperature at the evaporator section even though the rate of heat input to the evaporator varies. Another important characteristic of the thermosyphon is the fact that as it is a closed system, the thermosyphon can operate over lengthy periods without maintenance and is self contained.

When evaluating the thermal characteristics of the thermosyphon, it is important to consider the evaporator and condenser heat transfer coefficients. These heat transfer coefficients can be determined either experimentally or modelled mathematically using computational fluid dynamics (CFD). However, the use of CFD to date is limited and the results not entirely believable as many assumptions are used in evaluating the boundary conditions of the thermosyphon. The chaotic behaviour of the working fluid inside the thermosyphon also makes this method of determining the heat transfer coefficients very difficult. Hence, most researchers use experiments to determine the heat transfer capabilities of various fluids. The evaporator and condenser heat transfer coefficients will now be discussed with detailed correlations given in Section 3.1.



### ***The inside evaporation heat transfer coefficient***

The evaporation heat transfer coefficient is an important variable in the design of any thermosyphon. The falling film of liquid that is established in the condenser section persists into the evaporator section. At the upper part of the evaporator, the liquid film is sub-cooled. As the liquid falls, it reaches its saturation temperature and finally becomes superheated. Evaporation and nucleate boiling may both occur in the falling film and in the liquid pool situated at the bottom of the evaporator (Faghri, 1995).

The three mechanisms of boiling are nucleate, convective and film boiling and it is general practice to accept nucleate boiling inside thermosyphons, where vapour bubbles start to grow from nucleation sites. As the heat transfer coefficient is high in nucleate boiling, it is therefore a very efficient mode of heat transfer. As boiling is complex and difficult to model theoretically, the heat transfer coefficients are generally given by experimentally determined correlations. Whalley (1987) provides correlations for calculating the boiling heat transfer coefficient based on the Chen correlation. Piro (1997) also provides many correlations for evaporative heat transfer coefficients for different configurations and working fluids. However, care must be exercised as they give wildly differing results.

Dobson and Pakkies (2002) developed inside evaporator heat transfer coefficients for a R134a charged thermosyphon. A liquid fill charge ratio of 50 % was used and the tests were conducted for varying orientation angles. Their results showed that the heat transfer coefficients differed significantly for a vertical and an inclined thermosyphon. However, once inclined, the heat transfer coefficients did not vary significantly for inclination angles between 20 and 70°. They also showed that the maximum heat transfer rate when inclined at 45° is approximately 40 % higher than that of the vertical position.

Dobson and Kröger (1999) developed inside heat transfer coefficients for an ammonia-charged two-phase thermosyphon. Their results showed that their predicted heat transfer correlation was within 10 % of the experimental values. They also showed that existing pool boiling heat transfer coefficient correlations for ammonia under-estimated by on average of 57 % the experimentally determined values for a vertically orientated thermosyphon.

### ***The inside condensation heat transfer coefficient***

The vapour generated in the evaporator section rises up to the condenser section, where it condenses and returns to the evaporator as a falling liquid film. This condensation can occur either as filmwise condensation where the condensate forms a continuous film or as dropwise condensation (which does not wet the surface well). The latter is difficult to obtain and hence filmwise condensation is generally modelled as condensation inside a vertical tube using the Nusselt theory (Whalley, 1987). The continuity, momentum and energy equations can be solved for a liquid film control volume.

The result of combining the continuity, momentum and energy equations yields the local heat transfer coefficient

$$h_z = \left[ \frac{\rho_l (\rho_l - \rho_v) g h_{fg} k_l^3}{4 \mu_l \Delta T_{sat} z} \right]^{0.25} \quad (2.1)$$

However, the average heat transfer coefficient is normally of more importance than the local heat transfer coefficient and is given by

$$h = \frac{\sqrt{8}}{3} \left[ \frac{\rho_l (\rho_l - \rho_v) g h_{fg} k_l^3}{\mu_l \Delta T_{sat} L} \right]^{0.25} \quad (2.2)$$

Pan (2001) investigated the condensation heat transfer model by considering the interfacial shear due to mass transfer and interfacial velocity. Pan's model predictions differed significantly from the Nusselt solutions. This emphasised the significance of the interfacial shear on the condensation inside the thermosyphon as the interfacial shear due to the counter-current liquid and vapour flow obstructs the flow of the film.

## **2.2.2 Performance limitations and critical parameters of thermosyphons**

Some of the limitations and factors affecting thermosyphon performance include flooding, entrainment and dry-out and boiling limitations. These factors are discussed in this section.

### ***The flooding and entrainment limits***

Viscous shear interfacial forces arise when the relative velocity between the liquid and vapour increases and it is these forces that prevent the return of the liquid from the

condenser to the evaporator. The thermosyphon is then said to have reached flooding when all the liquid, just some of the liquid or all of the liquid just some of the time is prevented from returning to the evaporator. When additional heat is applied, the vapour velocity will increase, resulting in the liquid-vapour interface becoming unstable and unsteady. This then results in the liquid viscous forces being greater than the surface tension forces resulting in liquid droplets being entrained in the vapour region of the condenser section. This limitation is then known as the entrainment limit.

Wallis (1969) and Kutateladze (1972) formulated correlations for predicting the flooding limit of two-phase flows. The Wallis correlation however falls short as the effect of surface tension is not taken into account (Faghri, 1995). The Wallis equation is as follows:

$$V_l^{*\frac{1}{2}} + V_v^{*\frac{1}{2}} = C \quad (2.3)$$

Where  $V_l^*$  is a dimensionless liquid superficial velocity given by

$$V_l^* = \frac{V_l \rho_l^{\frac{1}{2}}}{[gd(\rho_l - \rho_v)]^{\frac{1}{2}}} \quad (2.4)$$

And  $V_v^*$  is a dimensionless vapour superficial velocity given by

$$V_v^* = \frac{V_v \rho_v^{\frac{1}{2}}}{[gd(\rho_l - \rho_v)]^{\frac{1}{2}}} \quad (2.5)$$

And  $C$  is a constant with a value of about 0.8.

The Kutateladze number correlation, on the other hand, includes the effect of the surface tension but does not include the effect of the pipe diameter. The Kutateladze numbers for the vapour and liquid are as follows:

$$K_v = \frac{V_v \rho_v^{\frac{1}{2}}}{[g\sigma(\rho_l - \rho_v)]^{\frac{1}{4}}} \quad (2.6)$$

$$K_l = \frac{V_l \rho_l^{\frac{1}{2}}}{[g\sigma(\rho_l - \rho_v)]^{\frac{1}{4}}} \quad (2.7)$$

The most commonly quoted correlation of this type is that  $K_v = 3.2$  derived by Pushkina and Sorokin (1969). Whaley (1987) suggests that the Wallis-type correlation be used if the tube diameter is small (<50 mm) and that the Pushkina and Sorokin correlation be used if the tube diameter is large (>50 mm).

Faghri et al. (Faghri, 1995) improved the existing semi-empirical correlations by including the effects of diameter, surface tension and working fluid properties. The following correlation was formulated for the maximum heat transfer rate:

$$\dot{Q}_{\max} = Kh_{fg}A[g\sigma(\rho_l - \rho_v)]^{1/4}[\rho_v^{-1/4} + \rho_l^{-1/4}]^{-2} \quad (2.8)$$

Where  $K$  is a Kutateladze number defined by

$$K = \left(\frac{\rho_l}{\rho_v}\right)^{0.14} \tanh^2 Bo^{1/4} \quad (2.9)$$

And  $Bo$  is the Bond number defined by

$$Bo = \left(\frac{C_k}{C_w}\right)^4 \left[\frac{\sigma}{g(\rho_l - \rho_v)}\right]^{1/2}; C_k = \sqrt{3.2} \quad (2.10)$$

With  $C_k$ , a constant defined by Kutateladze and  $C_w$ , an empirically determined constant ranging between 0.7 and 1 for various fluids.

The influence of filling plays an important role in the flooding limit. It can be summarised as follows: for small charges, the heat transfer limit increases as some power of the filling ratio; for large charges, the heat transfer limit remains constant (Lock, 1992). The liquid fill charge ratio is defined by the ratio of the volume of the liquid phase of the fluid under initial conditions to the inner volume of the thermosyphon or the evaporator volume. It is important to make the distinction between the fill-charge ratio with respect to the entire volume of the thermosyphon or just the evaporator volume when designing the thermosyphon as this can result in improper operation. It is recommended that in actual use, the quantity of working fluid charge should be between 30-33 % of the total volume of the thermosyphon. If however, the length of the condenser is longer than the evaporator, the ratio of the volume of liquid to the evaporator volume should be 50 % (Pioro, 1997).

Park et al. (2002) investigated the effects of the fill charge ratio for a two-phase closed thermosyphon. For the tests, a copper container with FC-72 as working fluid was used. The experiments were performed in the range of 50-600 W heat flow rate and 10-70 % fill charge ratio. The results showed that the heat transfer coefficient of the evaporator to the fill charge ratio were nearly negligible. However, at the condenser, the heat transfer coefficients showed some enhancements with the increase of fill charge ratio. However, no optimum fill charge ratio is given.

### ***The dry-out limitation***

When the liquid charge volume and the radial evaporator heat flux are very small, the dry-out limitation is reached at the bottom of the evaporator. The falling condensate persists into the evaporator section with its thickness approaching zero at the bottom. As a result, the entire amount of working fluid is circulated either as a falling film or as a vapour. A pool of liquid at the bottom of the evaporator is therefore not present and if the heat flux is increased, dry-out of the film will start from the bottom upwards, effectively shortening the evaporation area. The evaporator wall temperature will then increase steadily but the heat transfer rate will not (Faghri, 1995).

### ***The boiling limitation***

When the fill volume of the working fluid is large and the radial heat flux in the evaporator section is high, boiling limitation is achieved. As the heat flux is increased, nucleate boiling occurs in the evaporator. At the critical heat flux, the vapour bubbles coalesce near the pipe wall, which essentially prevents the liquid from touching the wall. The wall temperature then increases rapidly to compensate for the loss in heat flux, since the gas bubbles allow for an increase in thermal resistance for heat flow into the liquid (Faghri, 1995).

### ***Other Literature regarding performance limitations and critical parameters of thermosyphons***

The effect of the thermosyphon geometry also plays a critical role on the value of the limiting heat flux. Some researchers report that only the diameter affects the maximum heat transfer ( $\dot{Q}_{\max}$ ) whereas others report that only the evaporator length is the

determining factor. Recent studies show however, that both affect the value of  $\dot{Q}_{\max}$ . Experimental data has shown that with decreasing  $d_i/L_{\text{evap}}$ , the value of  $\dot{Q}_{\max}$  is increasingly affected by the interaction between the counter directed vapour and liquid flows. Whereas the dimensions of the evaporator exert a significant effect on  $\dot{Q}_{\max}$  the dimensions of the adiabatic length (section of the thermosyphon between the evaporator and condenser) and condenser do not have a significant effect. The geometric dimensions of the condenser may however affect the limiting heat transmitting capability of the thermosyphon indirectly owing to the fact that the pressure in the thermosyphon depends on the condenser dimensions and on the conditions of its cooling (Pioro, 1997).

Abou-Ziyan et al. (2001) investigated the performance of a thermosyphon with water and R134a as working fluids. For their tests, a copper pipe of OD 25 (ID 23) mm and 900 mm total length was used. The effect of the adiabatic length (a separator section between the evaporator and condenser section) was investigated. Their results showed that for their thermosyphon, the capability of the thermosyphon to transfer large amounts of heat is enhanced as the adiabatic length increases. They also investigated the effect of the liquid fill charge ratio. They concluded that the largest heat transport is obtained for a fill charge ratio of 50 %.

When selecting the working fluid, the first consideration is temperature (and hence the pressure of the vapour). The temperature is important as to ensure that the working fluid is stable and will not break down into its separate chemical components. The pressure is important to ensure that the thermosyphon does not leak. It is also important for the working fluid to have a high latent heat of vaporisation in order to transfer large amounts of heat with low vapour flow rates. The critical parameters of the working fluid should also be higher than the operating temperature of the thermosyphon. It has been shown that water is a good working fluid. It permits the transformation of more heat than all the other known working fluids, is inexpensive, readily available and is fire and explosion safe. However, it also has the ability to react with some substances, e.g. stainless steel (Pioro, 1997).

Payakaruk et al. (2000) investigated the heat transfer characteristics of an inclined thermosyphon. In their experiments, copper thermosyphons with ID's of 7.5, 11.1 and 25.3 mm were employed with R22, R123, R134a, ethanol, and water as the working fluids. The inclination angle was varied from the horizontal axis and the vapour temperature

ranged from 0 to 30 °C. Their results showed that the working fluid increased the heat transfer rate at inclination angles of 20 to 70° and that the lower the latent heat of vaporization of the fluid, the higher the heat transfer rate.

Dobson and Kroger (2000) investigated the thermal characteristics of an ammonia charged two-phase closed thermosyphon. For their setup, the thermosyphon consisted of a 6.2 m long by 31.9 mm inside diameter stainless steel pipe. The heating water from the hot water supply was increased from room temperature to a maximum of 80 °C and the cooling water varied between 10 and 20 °C. Their results showed that the inside heat transfer coefficients are complicated functions of the heat flux, temperature, liquid fill charge ratio, orientation and the evaporator and condenser lengths.

Nuntaphan et al. (2002) investigated the heat transport in a thermosyphon air preheater at high temperatures with a binary working fluid. For the test case, an ID 9.5 mm copper pipe with a wall thickness of 1 mm was used as the thermosyphon. The lengths of the evaporator, condenser and adiabatic sections were 400, 400 and 200 mm. The working fluid was water and the binary fluid that was added to the water was triethylene glycol (TEG). The filling ratio was 50 % of the evaporator volume. Their results showed that using TEG-water mixture, the critical limit due to flooding inside the thermosyphon could be extended and that the limit is directly proportional to the amount of TEG in the mixture. The tests also showed that with a suitable mixture of TEG-water, the performance of the preheater can be increased by 30-80 % for a parallel flow and 60-115 % for a counter flow air preheater compared to pure TEG.

### **2.2.3 Applications**

As heat pipes can be used over a very wide temperature range, from cryogenic temperatures (starting from -272 °C) to the high temperatures (2200-2700 °C), their applications cover a wide spectrum. They can be used in underground cool rooms, for aircraft temperature control and in spacecraft, to name but a few. The primary applications can however, be divided into two main categories: heat transfer from a heat source to a sink and temperature equalization control. Some uses of heat pipes (specifically thermosyphons) will now be discussed.

### ***Dehumidification and air conditioning:***

In an air conditioning system, the heat removed in cooling the incoming air to the thermosyphon can be recovered and used to reheat air. This increases the moisture removal capacity of the air conditioning system. The thermosyphon then recovers the energy in the hot humid air and uses it to re-heat the cold, dehumidified air. This saves in energy expenditure and also in a smaller cooling coil resulting in a more cost-effective system (Dobson, 1999). Wu et al. (1997) showed that for a specific test condition, the cooling capability of a system can be enhanced by 20 to 32.7 % using a HPHE.

### ***Electric power generation:***

Electric power is generally produced by means of the Rankine cycle. In this cycle, fossil fuel is converted into high pressure vapour in a boiler. The vapour moves through the turbine where its energy is converted into rotational power. This causes rotation of the turbine's shaft which in turn drives an electrical generator. Akbarzadeh et al. (2001) investigated the concept of a heat pipe turbine or thermosyphon Rankine engine for power generation using solar, geothermal or other available low grade heat sources. The basis of the engine is the thermosyphon cycle, which is modified to incorporate a turbine in the adiabatic region. The basic configuration is a closed vertical cylinder functioning as an evaporator, an insulated section and a condenser. The turbine is placed in the upper end between the insulated section and the condenser section, and a plate is installed to separate the high pressure region from the low pressure region in the condenser. The mechanical energy developed by the turbine can be converted to electrical energy by direct coupling to an electrical generator. Results showed that an electrical power output of 100 W could be achieved with a heat input of 10 kW and 6000 rpm.

### ***Heat recovery systems:***

As heat pipes are characterised by their high heat transfer capabilities and no external power requirements, they are being used in various heat exchangers for various applications. Advantages of these exchangers compared to the standard heat exchangers is the fact that they are nearly isothermal and can be built with better seals to reduce leakage. Cost savings are also evident with these exchangers as they are smaller and no power requirements are needed. HPHE's will be discussed in Section 2.3.



### **Other Applications:**

In a summary of the proceedings of the UK Institute of Refrigeration in 1998/1999 by Maidment and Eames (2001), thermosyphon developments for air conditioning are presented. A thermosyphon chiller consisting of a compressor, chiller, condenser and a four port valve is used to describe the free cooling capability of a thermosyphon. In this set-up, when the compressor is turned off the system operates by circulating refrigerant to the condenser without the use of the compressor but by means of the pressure difference produced by the temperature difference between the cooled water and the ambient air. It is shown that average coefficients of performance (COP) of between 10 and 13 can be obtained. In the report, mention is made of the first ammonia charged thermosyphon chiller installation in the UK. The 20 year life cycle cost of ownership for this system was estimated to be 55 % of that for an alternative system and COP's of between 8.5 and 14 were obtained. Figure 2.7 illustrates a typical thermosyphon chiller unit.

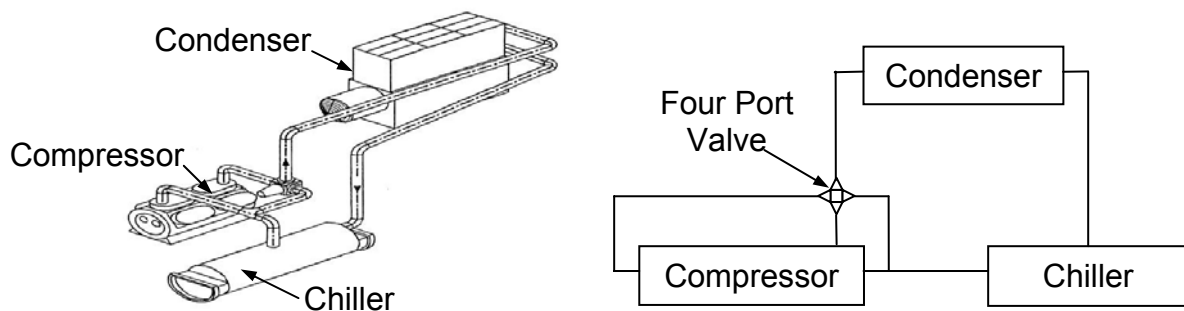


**Figure 2.7** Typical thermosyphon chiller arrangement (Maidment and Eames, 2001)

Pan et al. (2002) investigated the applications on freezing expansions of soil restrained two-phase closed thermosyphons. In cold regions, foundations of buildings are often deformed and damaged due to the freezing expansion of the soil in winter. One of the ways to prevent this damage is to make use of thermosyphons in which the evaporator section is buried in the soil and the condenser section is exposed to the air. When the air temperature is below the soil temperature, the evaporation-condensation cycle inside the thermosyphon starts and the thermal energy in the soil is then transferred into the environment and the soil temperature decreases. The soil remains frozen and the number of thaw cycles are reduced.

## 2.3 Heat Pipe Heat Exchangers (HPHEs)

Waste heat is heat which is generated in a process but then rejected to the environment even though it could still be reused for some useful or economic purpose. Sources of waste heat can be divided according to three temperature ranges. High temperature range ( $>650\text{ }^{\circ}\text{C}$ ), medium temperature range ( $230\text{-}650\text{ }^{\circ}\text{C}$ ) and low temperature range ( $<230\text{ }^{\circ}\text{C}$ ). Heat exchangers are devices generally used to recover the waste heat and depending on the configuration of the exchanger, can be used in all three temperature ranges (Goldstick, 1983).

The flow configuration for heat exchangers can be classified as single stream, parallel-flow two-stream, counterflow two-stream or cross flow two-stream. A single stream exchanger is one in which the temperature of only one fluid changes and the direction in which the fluid flows is immaterial. Condensers and boilers are examples. In the parallel-flow two-stream exchanger, the two fluids flow parallel to each other in the same direction. Examples are the shell and tube exchanger which is generally used for liquids and for high pressures. Fluids flow parallel to each other in opposite directions in a counterflow two-stream exchanger. The effectiveness is higher than that of a parallel flow exchanger and examples are feed water preheaters for boilers and oil coolers for aircrafts. In the cross flow two-stream exchanger, the two streams flow at right angles to each other. The hot stream may flow inside tubes arranged in a bank in a direction generally at right angles to the tubes. Either one or both of the streams may be unmixed (Mills, 1995).

Heat exchangers can also be classified as either regenerators or recuperators. In regenerators, heat is alternatively removed from the high temperature fluid and transferred to the low temperature fluid via a heat source. The energy transfer is dependant on the physical properties of the fluids and heat transfer surface as well as the flow situation of the two fluids. In recuperative heat exchangers, the high and low temperature fluids do not come into direct contact with each other but are separated by a barrier. The heat is transferred from the high temperature source through the wall into the lower temperature fluid by conduction through the supporting wall.

HPHEs are liquid-coupled indirect transfer type heat exchangers except that the HPHE employs heat pipes or thermosyphons as the major heat transfer mechanism from the high-temperature to the low-temperature fluid and do not require an external pump to

circulate the coupling fluid. They can be used for gas-to-gas, gas-to-liquid and liquid-to-liquid heat exchange. For the HPHE, the evaporator section of the thermosyphon is situated in the hot stream and the condenser section is situated in the cold stream. Heat transfer is aided by the addition of fins to increase the surface area available for convective heat transfer (Faghri, 1995). Figure 2.8 illustrates a commercial HPHE.



**Figure 2.8** A commercial HPHE (Colmac Coil, 2000)

The use of heat pipes or thermosyphons in the exchanger configuration is ever-increasing in popularity and is attributed to the following advantages:

- Thermosyphons have no moving parts and auxiliary working fluid power requirements are not needed.
- The hot and cold streams of the HPHE can be completely isolated preventing cross-contamination of the fluids.
- The rate of heat transferred can be increased by adjusting the tilt angle.
- HPHE are redundant in design. If one thermosyphon fails the heat exchanger is still operational.
- HPHE have the ability to operate as thermal transformers. By altering the relative lengths of the evaporator and condenser sections the temperature at which the heat is transferred can be selected or adjusted.

Commercial production of HPHEs began in the mid-1970s and have since found many applications in industry. These applications can be divided into three main categories (Noie-Baghban and Majideian, 2000):

- Heat recovery in air conditioning devices.

The HPHE is installed in the ventilation system and recovers heat from the stale outgoing air and transfers it to the fresh incoming air. For these HPHE's, high heat

transfer coefficients and heat transfer surface areas are needed to offset the relatively low temperature difference between the two fluid streams.

- Heat recovery from the process exhaust streams to preheat air for space heating.  
The temperatures encountered here are generally higher than those in the HVAC applications. The temperature difference is also much higher. The thermosyphons are generally constructed of copper for lower temperature exhaust streams and carbon-steel for higher temperature applications.
- Heat recovery from the process exhaust streams to re-use in the process.  
The most severe applications are in the exhaust waste heat recovery for re-use in the process industries. Examples of such application include air driers and ovens. Temperatures up to 400 °C are common to exhaust streams of industrial processes.

Zhang and Zhuang (2003) investigated the use of heat pipe gas-gas heat exchangers and heat pipe air preheaters. They investigated 20 different structure types of 26-32 mm in diameter and 1.2-2 m in length under 300 different operating conditions. The following table illustrates a typical air preheater that was investigated. The heat recovery of 11970 kW illustrates the economic efficiency and the important role that such a heat exchanger can play in the energy-saving transformation in large plants.

**Table 2.1** HPHE configuration (Zhang and Zhuang, 2003)

Pipe size [mm]	OD 51 t=4.5, L = 6000, 1914 pieces	
Heat Exchanger size [m]	Height 6.4, Length 2.4, Inlet width 13.7, Outlet width 10.37	
	<b>Flue gas</b>	<b>Air</b>
Flow rate [Nm <sup>3</sup> /h]	238000	195860
Inlet temp [°C]	297.7	54.8
Outlet Temp [°C]	171.2	228.7
Pressure Drop [Pa]	580	280
Heat Recovery [kW]	11970	

Lukitobudi et al. (1995) investigated the design, construction and testing of a thermosyphon heat exchanger for medium temperature heat recovery. For the tests, water was used as the working fluid. Copper pipes of OD 15.88 mm were used and evaporator, condenser and adiabatic lengths were 300, 300 and 150 mm respectively. From the study,

effectiveness for the thermosyphon heat exchanger was evaluated and a maximum effectiveness formulated. The results of the study showed that by using a finned copper thermosyphon heat exchanger as apposed to a finned steel thermosyphon heat pipe exchanger, effectiveness values ranging between 17.8 - 63 % could be obtained instead of 6.2 - 48.5 %.

Yang et al. (2003) demonstrated the use of a gravity assisted heat pipe heat exchanger for heat recovery of the exhaust gas of an automobile. In cold areas, the heat of the automotive exhaust gas is conveyed into the vehicles carriage utilizing the heat pipes. Air from the carriage is introduced into the recovery unit by a fan and warmed by the heat from the exhaust gas. The air then flows into the carriage to keep a comfortable temperature.

## **2.4 Air Drying**

It was decided to include drying in the literature study as the utilisation of an air drier to demonstrate the feasibility of a HPHE was defined early in the thesis outline. Drying may involve various modes of heat transfer such as convection, conduction or radiation. In convection drying, the heating medium comes into direct contact with the solid material and initiates diffusion of water vapour from and within the material. In conduction drying, the heating medium is separated from the solid by a hot conducting surface such as in drum, cone and trough driers. In radiation drying, heat is transmitted solely as radiant energy (Sharma et al. 2000). Figure 2.9 illustrates a typical air drier unit. Unless otherwise stated, the information is supplied by Dobson (2001).

The rate of drying depends on properties of the material being dried such as the bulk density, initial moisture content and its relation to the equilibrium moisture content under drying conditions and can be divided into constant rate drying and falling rate drying. The equilibrium moisture content depends on the temperature and the relative humidity of the air. This equilibrium content is the state when the material has been exposed to the hot air for a long time and drying ceases.

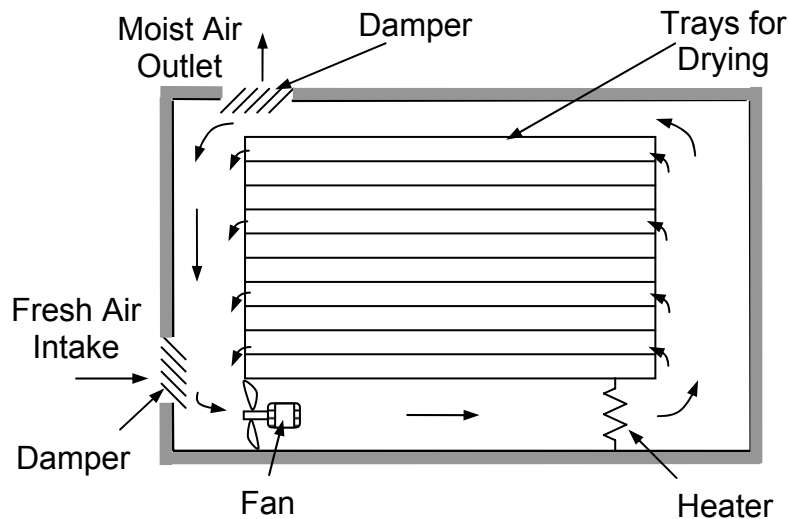


**Figure 2.9** A typical air drier unit

Constant rate drying is characterized by the evaporation of moisture from a saturated surface. This involves the diffusion of water vapour from a saturated surface of the material through an air film into the bulk of the air. The rate of drying is controlled by the rate of heat transfer to the surface (Sharma et al. 2000). In the constant rate drying period the surface of the material is supplied by an excessive amount of liquid by capillary action. The rate of drying tends to be controlled by the rate at which the layer of liquid on the surface is able to evaporate (Dobson, 2001).

At end of the constant rate period, the critical moisture content is reached. At this point, the surface of the solid is no longer saturated and dry spots occur. The outside wet area may be reduced and the rate of drying falls off progressively. This period is usually the longest period of drying operation and is known as falling rate drying. The drying rate depends on the air temperature and food bed thickness and is unaffected by the relative humidity and the velocity of the air (Sharma et al. 2000). In this rate, the drying tends to be controlled by the ability of the water to diffuse to the surface of the material.

Drying of a material occurs by transfer of water vapour from a saturated liquid-vapour interface through an air film to the bulk gas phase or environment. The rate of water removal is controlled by the heat transfer to the evaporating surface, which allows for the liquid to evaporate. The rate of mass transfer at steady state balances the rate of heat transfer into the material being dried. For temperature controlled drying, the rate of convective heat transfer from the air to the surface of the material being dried is given by:

$$\dot{Q} = hA(T_{air} - T_s) \quad (2.11)$$

The heat required to vaporize the water, at the rate of  $\dot{m}_{evap}$ , from the surface is

$$\dot{Q} = \dot{m}_{evap}(h_g - h_f) = \dot{m}_{evap} h_{fg} \quad (2.12)$$

And from equations 2.11 and 2.12, the following relation holds

$$\dot{m}_{evap} = \frac{hA(T_{air} - T_w)}{h_{fg}} \quad (2.13)$$

Alternatively, the mass flux of vapour leaving the surface of the material can be considered using Fick's law:

$$\frac{\dot{m}_{evap}}{A} = k(P_{sat@T_w} - P_v) \quad (2.14)$$

Where

$P_{sat@T_w}$  = saturation temperature corresponding to the temperature of the surface

$P_v$  = partial pressure of the water vapour in the air

$k$  = mass transfer coefficient

The rate of evaporation can therefore be evaluated by either equation 2.13 or 2.14. In order to predict the mass transfer rate in the constant rate period, the heat transfer coefficient needs to be known. The following correlations are given for drying rate purposes (Dobson, 2001):

For air flows parallel to the surface and velocities between 0.5 and 7.6 m/s

$$h = 14.3\rho V^{0.8} \quad (2.15)$$

For air flows perpendicular to the surface and velocities between 0.9 and 4.6 m/s

$$h = 24.2\rho V^{0.37} \quad (2.16)$$

### 3 THERMAL MODELING

This section discusses the theory and presents equations in the thermal modelling of a single thermosyphon. From this theory a thermal model for a HPHE using many thermosyphons can be developed. Also presented in this section is the modelling of an air drier used to simulate a variety of drying applications.

#### 3.1 Single Thermosyphon

For a single thermosyphon, heat is transferred across the evaporator wall, through the evaporator internal section, the condenser internal section and the condenser walls. The heat that is transferred by the thermosyphon depends on the temperature difference and the thermal resistance to heat flow between the hot and cold ends. Figure 3.1 illustrates the thermal resistance model of a thermosyphon.

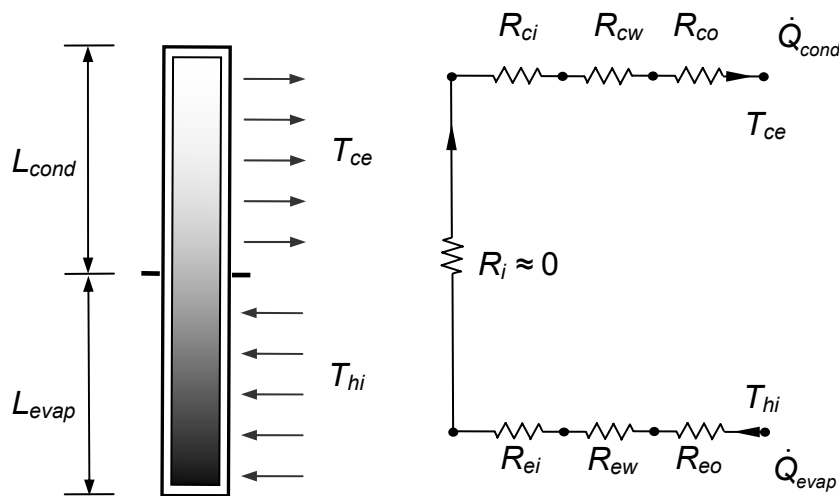


**Figure 3.1** Thermal resistance model of a thermosyphon

The evaporator heat transfer rate can be expressed in terms of the temperature difference between the hot and internal temperatures as

$$\dot{Q}_{evap} = \frac{\bar{T}_h - T_i}{\Sigma R_{evap}} \quad (3.1)$$

And the heat transfer rate out of the condensing section as

$$\dot{Q}_{cond} = \frac{T_i - \bar{T}_c}{\Sigma R_{cond}} \quad (3.2)$$



Where

$$\bar{T}_h = (T_{hi} + T_{he})/2$$

$$\bar{T}_c = (T_{ci} + T_{ce})/2$$

For steady operation, the heat transfer input equals the heat transfer output

$$\dot{Q}_{cond} = \dot{Q}_{evap} = \dot{Q} \quad (3.3)$$

The internal temperature,  $T_i$  can be eliminated and rearranged to give

$$\dot{Q} = \frac{\bar{T}_h - \bar{T}_c}{\Sigma R_{evap} + \Sigma R_{cond}} = \frac{\bar{T}_h - \bar{T}_c}{\Sigma R} \quad (3.4)$$

Where

$$\Sigma R = \Sigma R_{evap} + \Sigma R_{cond} \quad (3.5)$$

$\Sigma R_{evap}$  and  $\Sigma R_{cond}$  represent the total thermal resistance over the evaporator and condenser sections, respectively, and are given by

$$\Sigma R_{evap} = R_{eo} + R_{ew} + R_{ei} \quad (3.6)$$

$$\Sigma R_{cond} = R_{ci} + R_{cw} + R_{co} \quad (3.7)$$

The following sections describe the individual resistances across the evaporator and condenser sections in terms of the thermal resistance model.

### 3.1.1 Heat transfer resistance across the evaporator and condenser walls

The wall thermal resistances for the evaporator and condenser sections are calculated from Fourier's law of conduction across a cylindrical shell. With an inside diameter  $d_i$ , outside diameter  $d_o$ , length  $L_{evap}$ ,  $L_{cond}$  and wall thermal conductivity  $k$ , the thermal resistance is given by (Mills, 1995)

$$R_{ew,cw} = \frac{\ln(d_o/d_i)}{2\pi k L_{evap,cond}} \quad (3.8)$$

### 3.1.2 Evaporator internal heat transfer resistance

The falling film of liquid that is established in the condenser section persists into the evaporator section. Evaporation and nucleate boiling may both occur in the falling film and in the liquid pool situated at the bottom of the evaporator (Faghri, 1995). The three mechanisms of boiling are nucleate, convective and film boiling and it is general practice to accept nucleate boiling inside thermosyphons, where vapour bubbles start to grow from nucleation sites.

El-Genk and Saber (1997) investigated the liquid film and pool regions in the evaporator of a thermosyphon. Water, ethanol, methanol, Dowtherm-A, R-11 and R-113 were used as working fluids and all the data was correlated to within 15 % by the heat transfer correlations. The liquid pool was divided into three heat transfer regimes: natural convection, nucleate boiling and combined convection where both the natural convection and nucleate boiling contribute to the heat transfer.

For the liquid pool, the natural convection correlation is given by

$$h_{NC} = 0.475Ra^{0.35} \left( \frac{\sqrt{\sigma/g(\rho_l - \rho_v)}}{d_i} \right)^{0.58} \frac{k_l}{d_i} \quad (3.9)$$

Where the Rayleigh number is given by

$$Ra = \frac{\beta g d_i^4 \dot{q}_e}{k_l \alpha_l \nu_l} \quad (3.10)$$

The nucleate boiling correlation for the pool is given by

$$h_{NB} = (1 + 4.95\psi)h_{KU} \quad (3.11)$$

Where the Kutateladze heat transfer coefficient,  $h_{KU}$  is given as

$$h_{KU} = 6.95 \times 10^{-4} Pr_l^{0.35} \left( \frac{\dot{q}_e \sqrt{\sigma/g(\rho_l - \rho_v)}}{\rho_v h_{fg} \nu_l} \right)^{0.7} \left( \frac{P \sqrt{\sigma/g(\rho_l - \rho_v)}}{\sigma} \right)^{0.7} \left( \frac{k_l}{d_i} \right) \quad (3.12)$$

The mixing pool coefficient is given by

$$\psi = \left( \frac{\rho_v}{\rho_l} \right)^{0.4} \left[ \left( \frac{P \nu_l}{\sigma} \right) \left( \frac{\rho_l^2}{\sigma g (\rho_l - \rho_v)} \right)^{0.25} \right]^{0.25} \quad (3.13)$$

This mixing pool coefficient reflects the contribution of mixing by sliding and rising bubbles to the nucleate boiling heat transfer in the pool. The combined convection can then be given in terms of the natural convection and nucleate boiling correlations

$$h_{CC} = (h_{NC}^4 + h_{NB}^4)^{0.25} \quad (3.14)$$

El-Genk and Saber (1997) also introduced a dimensionless pool parameter,  $X$  whereby the different heat transfer regimes could be classified:

For Natural Convection  $X < 10^6$

For Nucleate Boiling  $X > 2.1 \times 10^7$

And for combined convection  $10^6 \leq X \leq 2.1 \times 10^7$

With

$$X = \psi Ra^{0.35} Pr_l^{0.35} \left( \frac{P \sqrt{\sigma/g(\rho_l - \rho_v)}}{\sigma} \right)^{0.7} Re_v^{0.7} \quad (3.15)$$

Where

$$Re_v = \frac{\dot{q}_{evap} L_m}{\rho_v h_{fg} v_l} \quad (3.16)$$

And the bubble length scale,  $L_m$  is defined by

$$L_m = \sqrt{\frac{\sigma}{g(\rho_l - \rho_v)}} \quad (3.17)$$

The liquid film region was also divided into three heat transfer regimes: laminar convection, nucleate boiling and combined convection. These regimes were classified in terms of a wall heat flux exponent,  $n$ .

The laminar convection correlation for the liquid film with  $n = -\frac{1}{3}$  is given by

$$h_x = \left( \frac{4}{3} \right)^{\frac{1}{3}} Re_x^{-\frac{1}{3}} k_l / \left[ \frac{v_l^2}{g} \left( \frac{\rho_l}{\rho_l - \rho_v} \right) \right]^{\frac{1}{3}} \quad (3.18)$$

The nucleate boiling correlation for the liquid film with  $0.67 < n < 0.7$  is given by

$$h_{NB} = 1.155 \times 10^{-3} N_{\mu f}^{0.33} Pr_l^{0.35} \left( \frac{P \sqrt{\sigma/g(\rho_l - \rho_v)}}{\sigma} \right)^{0.7} Re_{ev}^{0.7} \frac{k_l}{\left[ \frac{v_l^2}{g} \left( \frac{\rho_l}{\rho_l - \rho_v} \right) \right]^{1/3}} \quad (3.19)$$

Where the viscosity number is given by

$$N_{\mu f} = \frac{\mu_l}{(\sigma g \sqrt{\sigma/g(\rho_l - \rho_v)})^{0.5}} \quad (3.20)$$

The combined convection correlation for the liquid film can then be given in terms of the laminar convection and nucleate boiling correlations, with  $-\frac{1}{3} < n < 0.67$  as

$$h_{CC} = (h_x^3 + h_{NB}^3)^{1/3} \quad (3.21)$$

A dimensionless film parameter,  $\eta$  is introduced to distinguish between the various heat transfer regimes in the liquid film:

For laminar convection  $\eta \leq 10^9$

For nucleate boiling  $\eta \geq 2.7 \times 10^{10}$

And for combined convection  $10^9 < \eta < 2.7 \times 10^{10}$

With

$$\eta = Re_{ev}^2 \left( \frac{P \sqrt{\sigma/g(\rho_l - \rho_v)}}{\sigma} \right)^2 Re_{ex} / Pr_l \quad (3.22)$$

Imura et al. (1979) proposed the following inside heat transfer coefficient in which they found that the ratio of the filled volume to the total volume and that the ratio of the heated to cooled length had little effect on the mean heat transfer coefficient (Faghri, 1995).

$$h_{ei} = 0.32 \left( \frac{\rho_l^{0.65} k_l^{0.3} cp_l^{0.7} g^{0.2} q_e^{0.4}}{\rho_v^{0.25} h_{fg}^{0.4} \mu_l^{0.1}} \right) \left( \frac{P_{sat}}{P_a} \right)^{0.3} \quad (3.23)$$

Shiraishi et al. (1981) however correlated their data after changing the exponent of 0.3 in equation 3.23 to 0.23, (Pioro and Pioro, 1997).

$$h_{ei} = 0.32 \left( \frac{\rho_l^{0.65} k_l^{0.3} cp_l^{0.7} g^{0.2} q_e^{0.4}}{\rho_v^{0.25} h_{fg}^{0.4} \mu_l^{0.1}} \right) \left( \frac{P_{sat}}{P_a} \right)^{0.23} \quad (3.24)$$

With  $q_e = 1000 - 35000 \text{ W/m}^2$ ,  $V^* = 50 - 100 \%$  and  $T_{sat} = 32 - 60 \text{ }^\circ\text{C}$

The inside heat transfer coefficient can also be expressed in terms of the Nusselt theory given by (Whalley, 1987). However, this is not a good approximation as Nusselt theory is generally used for filmwise condensation.

$$h = \frac{\sqrt{8}}{3} \left[ \frac{\rho_l (\rho_l - \rho_v) g h_{fg} k_l^3}{\mu_l (T_{wall} - T_{sat}) L_{evap}} \right]^{0.25} \quad (3.25)$$

Semena et al. (1988) proposed the following correlation for their data set comprising of  $\dot{q}_e = 6000-1100000 \text{ W/m}^2$ ,  $L_{evap} = 0.25-0.7 \text{ m}$ ,  $\phi = 5 - 90^\circ$ ,  $d_i = 6-24 \text{ mm}$  and  $V^* = 20-50 \%$  (Piro and Piro, 1997)

$$h_{ei} = 0.0123 \left( \frac{k_l}{L_m} \right) \left( \frac{\dot{q}_e L_m}{h_{fg} (\rho_l - \rho_v) \mu_l} \right)^{0.5} \left( \frac{\mu_l c p_l}{k_l} \right)^{0.35} \left( \frac{P_i}{\sqrt{\sigma g (\rho_l - \rho_v)}} \right)^{0.54} \left( \frac{d_i}{L_m} \right)^{0.17} \quad (3.26)$$

In order to take into account, the effect that the inclination angle has on the heat transfer coefficient, Piro and Piro (1997) recommend the following

$$h_{inclined} = h_{vertical} 0.61e^{0.5 \sin^4 \phi} \quad (3.27)$$

Where for equation 3.27,  $\phi = 0^\circ$  represents the vertical situation. Once the heat transfer coefficient is calculated, the thermal resistance is calculated as follows

$$R_{ei} = 1/(h_{ei} A_{ei}) \quad (3.28)$$

With the area being

$$A_{ei} = \pi d_i L_{evap} \quad (3.29)$$

### 3.1.3 Condenser internal heat transfer resistance

The condensate that falls from the condenser section to the evaporator section occurs either as filmwise condensation were the condensate forms a continuous film or as dropwise condensation. The latter is difficult to obtain and hence filmwise condensation is generally modelled as condensation inside a vertical tube using the Nusselt theory. The assumption is however that there are negligible shear stresses at the liquid-vapour

interface and that a constant temperature difference occurs between the wall and the saturated vapour. The local heat transfer coefficient is given by (Faghri, 1995):

$$h_z = \frac{k_l}{\delta_z} \left[ \frac{\rho_l (\rho_l - \rho_v) g h_{fg} k_l^3 [h_{fg} + 0.68 c_{p_l} \Delta T_{sat}]}{4 \mu_l \Delta T_{sat} z} \right]^{0.25} \quad (3.30)$$

A local modified Nusselt number is then introduced

$$Nu_z^* = \frac{h_z}{k_l} \left[ \frac{g}{v_l^2} \left( \frac{\rho_l - \rho_v}{\rho_l} \right) \right]^{-1/3} = 0.693 Re_l^{-1/3} \quad (3.31)$$

Where

$$Re_l = \frac{\dot{Q}_{cond}}{\pi d_i \mu_l h_{fg}} \quad (3.32)$$

The average heat transfer coefficient is then given by

$$\bar{h} = \frac{1}{L_{cond}} \int_0^{L_c} h_z dz = \frac{\sqrt{8}}{3} \left[ \frac{\rho_l (\rho_l - \rho_v) g k_l^3 [h_{fg} + 0.68 c_{p_l} (T_{sat} - T_w)]}{\mu_l (T_{sat} - T_w) L_{cond}} \right]^{0.25} \quad (3.33)$$

In relating the modified Nusselt number and Reynolds numbers, the heat transfer coefficient can be expressed in dimensionless form as follows

$$\bar{Nu}^* = \frac{\bar{h}}{k_l} \left[ \frac{v_l^2}{g} \left( \frac{\rho_l}{\rho_l - \rho_v} \right) \right]^{1/3} = 0.925 Re_{l,max}^{-1/3} \quad (3.34)$$

Where

$$Re_{l,max} = \frac{\dot{Q}_{cond}}{\pi d_i \mu_l h_{fg}} \quad (3.35)$$

For inclination angles, the following adjustment is made

$$Re_{\phi} = Re_{l,max} f_{\phi} \quad (3.36)$$

With  $f_{\phi} = 1$  for vertical tubes and  $f_{\phi} = 2.87 \left[ \frac{d_i}{L_{cond} \sin \phi} \right]$  for tubes with  $\phi > 10^\circ$  where  $\phi = 0^\circ$

represents vertical operation. The heat transfer coefficients according to the ESDU (1981) over the flow regions are given by (Faghri, 1995)

For  $Re_{l,max} < 325$

$$h_{ci} = 0.925 Re_{l,max}^{-1/3} \frac{k_l}{\left[ \frac{v_l^2}{g} \left( \frac{\rho_l}{\rho_l - \rho_v} \right) \right]^{1/3}} \quad (3.37)$$

For  $Re_{l,max} \geq 325$

$$h_{ci} = 0.0134 Re_{l,max}^{0.4} \frac{k_l}{\left[ \frac{v_l^2}{g} \left( \frac{\rho_l}{\rho_l - \rho_v} \right) \right]^{1/3}} \quad (3.38)$$

Uehara et al. (1983) however propose the following correlations (Faghri, 1995)

For  $0.5 < Re_{l,max} f_\phi < 325 Pr_l^{-0.96}$

$$h_{ci} = 0.884 (Re_{l,max} f_\phi)^{-1/4} \frac{k_l}{\left[ \frac{v_l^2}{g} \left( \frac{\rho_l}{\rho_l - \rho_v} \right) \right]^{1/3}} \quad (3.39)$$

For  $Re_{l,max} f_\phi \geq 325 Pr_l^{-0.96}$

$$h_{ci} = 0.044 (Re_{l,max} f_\phi)^{1/6} Pr_l^{2/5} \frac{k_l}{\left[ \frac{v_l^2}{g} \left( \frac{\rho_l}{\rho_l - \rho_v} \right) \right]^{1/3}} \quad (3.40)$$

The following equation is attributable to Wang and Ma (1991) and is presented as (Faghri, 1995)

$$h_{ci} = h_N \left[ P_{sat}^{0.37} \left( \frac{2L_{cond}}{d_i} \right)^{[\cos(\pi/2-\phi)]/4} \left[ \begin{array}{l} 0.41 - 0.72V^+ \\ + (-62.7V^{+2} + 14.5V^+ + 7.1)(\pi/2 - \phi)/1000 \end{array} \right] \right] \quad (3.41)$$

Where  $V^+ = V_l/V_{tot} \geq 0.1$  for their experiments,  $h_N$  is the Nusselt heat transfer coefficient and  $\phi$  is measured from the vertical. Once the heat transfer coefficient is calculated, the thermal resistance is calculated as follows

$$R_{ci} = 1/(h_{ci} A_{ci}) \quad (3.42)$$

With the area being

$$A_{ci} = \pi d_i L_{cond} \quad (3.43)$$

### 3.1.4 Outside heat transfer resistance

Forced or natural convection analysis is used to calculate the outside heat transfer resistance of a single unfinned thermosyphon tube. Section 3.2 details the analysis for forced convection. However, for natural convection, Churchill and Chu (1975) proposed the following correlations (Mills, 1995)

For laminar flow,  $R_{aL} \leq 10^9$

$$\bar{N}_{uL} = 0.68 + 0.67 (R_{aL} \psi)^{1/4} \quad (3.44)$$

For turbulent flow  $10^9 \leq R_{aL} < 10^{12}$

$$\bar{N}_{uL} = 0.68 + 0.67 (R_{aL} \psi)^{1/4} (1 + 1.6 \times 10^{-8} R_{aL} \psi)^{1/12} \quad (3.45)$$

With

$$\psi = \left[ 1 + \left( \frac{0.492}{Pr} \right)^{9/16} \right]^{-16/9} \quad (3.46)$$

From which the outside convection heat transfer coefficient is calculated from

$$h_c = \left( \frac{k}{L_{evap,cond}} \right) \bar{N}_{uL} \quad (3.47)$$

The determination of the thermal resistance is analogous to that of equation 3.28, with the inside area being substituted by the outside area.



## 3.2 Thermosyphon Heat Exchanger Model

The thermosyphon heat exchanger (HPHE) consists of an array of staggered or aligned thermosyphon tubes that may be either finned or unfinned. The three common configurations are given as being either individual bare tubes, individual finned tubes or the HPHE consisting of a plate finned tube bundle configuration.

For the modelling, the heat transfer resistances across the walls and the internal heat transfer resistances are calculated as in Section 3.1. The modelling of the resistance between the fins and the outside air is now discussed depending on the flow configuration and the respective pressure drop correlations for these configurations are given.

### 3.2.1 Unfinned individual tube configuration

This configuration consists of an array or bundle of unfinned tubes, which are either aligned or staggered, that are surrounded by side walls. Figure 3.2 illustrates this. By adjusting the velocity such that the Reynolds number is based on an average velocity in the space between two adjacent tubes, the Churchill and Bernstein (1977) formulae for calculating the average Nusselt number,  $\bar{N}_{ud}$  can be used (Mills, 1995)

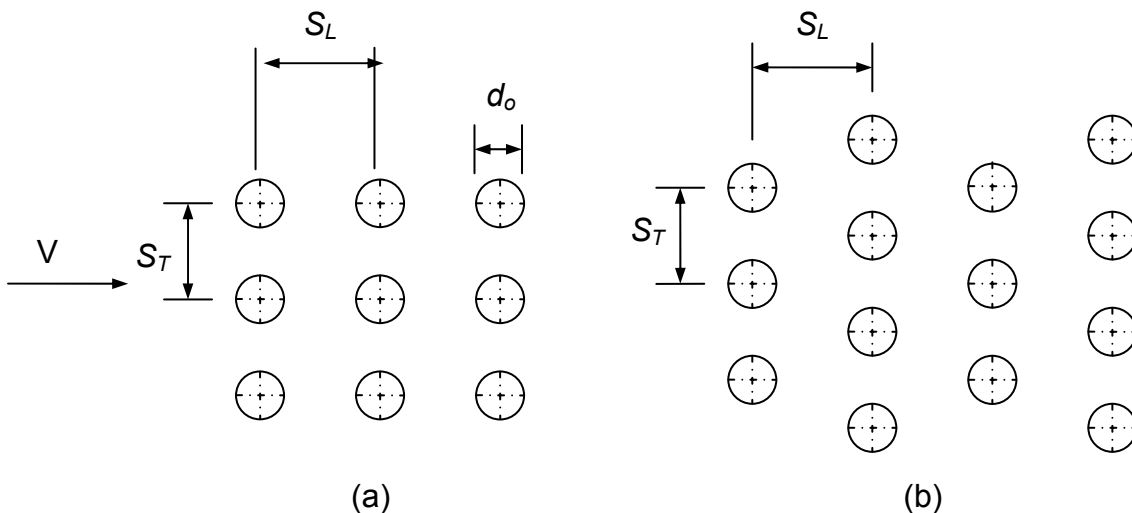


**Figure 3.2** The tube bundle configurations, (a) Aligned, (b) Staggered

For  $Re_d < 10^4$ :

$$\bar{N}_{ud} = 0.3 + \frac{0.62 Re_d^{1/2} Pr^{1/3}}{\left[1 + (0.4/Pr)^{2/3}\right]^{1/4}} \quad (3.48)$$

For  $2 \times 10^4 < Re_d < 4 \times 10^5$ :

$$\bar{N}_{ud}^{-1} = 0.3 + \frac{0.62 Re_d^{1/2} Pr^{1/3}}{\left[1 + (0.4/Pr)^{2/3}\right]^{1/4}} \left[1 + \left(\frac{Re_d}{282000}\right)^{1/2}\right] \quad (3.49)$$

For  $4 \times 10^5 < Re_d < 5 \times 10^6$ :

$$\bar{N}_{ud}^{-1} = 0.3 + \frac{0.62 Re_d^{1/2} Pr^{1/3}}{\left[1 + (0.4/Pr)^{2/3}\right]^{1/4}} \left[1 + \left(\frac{Re_d}{282000}\right)^{5/8}\right]^{4/5} \quad (3.50)$$

Where the velocity is adjusted as follows

$$\bar{V} = V_o \left( \frac{S_T}{S_T - (\pi/4)d_o} \right) \quad (3.51)$$

For tube banks of fewer than 10 rows, the following interpolation formula applies

$$\bar{N}_{ud}^{<10} = \frac{1 + (N_r - 1)\phi}{N_r} \bar{N}_{ud}^{-1} \quad (3.52)$$

The average  $N_{ud}^{\geq 10}$  for a tube bank with 10 or more rows is calculated from

$$\bar{N}_{ud}^{\geq 10} = \phi \bar{N}_{ud}^{-1} \quad (3.53)$$

Where the arrangement factors are

$$\phi_{aligned} = 1 + \frac{0.7}{\psi^{1.5}} \frac{S_L/S_T - 0.3}{(S_L/S_T + 0.7)^2} \quad (3.54)$$

$$\phi_{staggered} = 1 + 2/3 P_L \quad (3.55)$$

Dimensionless transverse and longitudinal pitches are used in the factor  $\psi$

$$\psi = 1 - \frac{\pi}{4 P_T} \quad \text{if } P_L \geq 1 \quad (3.56)$$

$$\psi = 1 - \frac{\pi}{4 P_T P_L} \quad \text{if } P_L < 1 \quad (3.57)$$

With the pitches being

$$P_T = S_T/d_o \quad \text{and} \quad P_L = S_L/d_o \quad (3.58)$$

From the Nusselt number, the outside heat transfer coefficient,  $h_{eo,co}$  can be calculated. The thermal resistance can then be calculated using the following formula where  $N_p$  is the number of thermosyphon tubes

$$R_{e_o,co} = \frac{1}{h_{e_o,co} A_{e\text{face},c\text{face}} N_p} \quad (3.59)$$

With

$$A_{e\text{face},c\text{face}} = \pi d_o L_{\text{evap,cond}} N_p \quad (3.60)$$

For the pressure drop across the unfinned individual tube configuration, Zukauskus (1985) recommends the following correlation (Mills, 1995)

$$\Delta P = N_r \chi \left( \frac{\rho V_{\text{max}}^2}{2} \right) f \quad (3.61)$$

Where Zukauskus correlates the friction factor,  $f$  and correction factor,  $\chi$  using empirically determined data based on the Reynolds number and geometric parameters. The maximum velocity is given as

$$V_{\text{max,aligned}} = V_o \left( \frac{S_T}{S_T - d_o} \right) \quad (3.62)$$

$$V_{\text{max,staggered}} = V_o \times \max \left[ \left( \frac{S_T}{S_T - d_o} \right), \frac{S_T/2}{(S_L^2 + (S_T/2))^{\frac{1}{2}} - d_o} \right] \quad (3.63)$$

### 3.2.2 Plate finned tube bundle configuration

The plate finned tube bundle configuration consists of an array of finned tubes where the fins are plate fins that are separated by spacers from each other. The spacers are in the form of the protrusions punched out of the finned surface. The array of tubes can be either aligned or staggered, however it is general practice to use the staggered configuration as it allows for higher heat transfer rates. Figure 3.3 illustrates the plate finned tube bundle configuration. Kröger (1998) presents the method for analysing the control volume. This method is described in full as it was used in a computer code for the design of HPHE's as described in Appendix C.

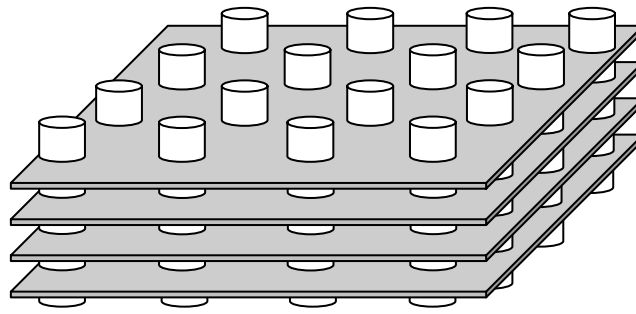


**Figure 3.3** Plate finned tube bundle Configuration

For the analysis of the thermal resistance, an elemental control volume through which the flow passes is considered and is illustrated in Figure 3.4.

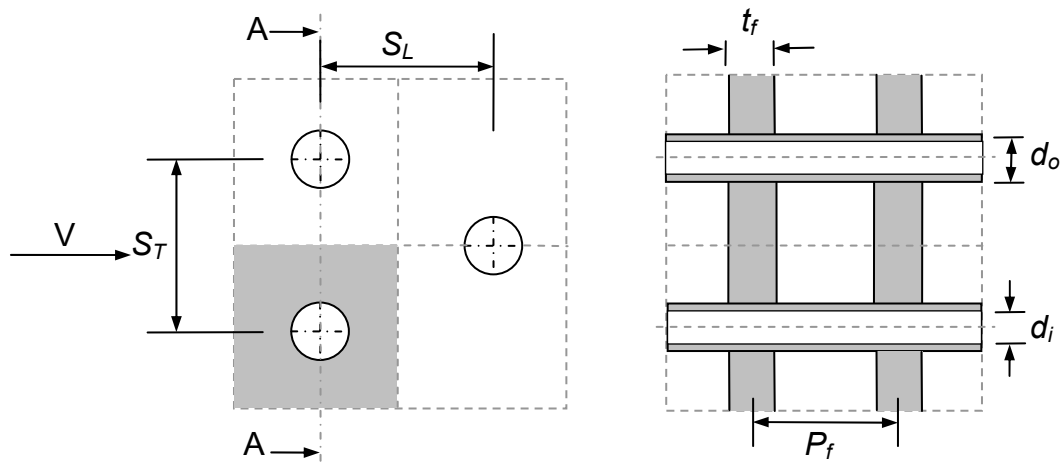


**Figure 3.4** The Plate-and-tube Control Volume, (a) Plan View, (b) Cut-away View

The minimum free flow area of the control volume,  $A_{cvc}$  is

$$A_{cvc} = (S_T - d_o)(P_f - t_f) \quad (3.64)$$

And the corresponding frontal area,  $A_{cvfr}$  is given as

$$A_{cvfr} = S_T P_f \quad (3.65)$$

The area ratio,  $\sigma$  is then given by

$$\sigma = A_{cvc} / A_{cvfr} \quad (3.66)$$

The fin surface area exposed to the air stream is given by

$$A_{cvf} = 2[S_T S_L - \pi d_o^2 / 4] \quad (3.67)$$

And the surface area exposed to the air stream flowing through the elementary control volume is given as

$$A_{cva} = A_{cvf} + (P_f - t_f)(\pi d_o) \quad (3.68)$$

The hydraulic diameter of the control volume is

$$d_h = 4A_{cvc} S_L / A_{cva} \quad (3.69)$$

The mass velocity,  $G_{cv}$  through the minimum free flow area of the control volume is given as

$$G_{cv} = \dot{m} / A_{cvfr} \sigma \quad (3.70)$$

From which the corresponding Reynolds number can be calculated

$$R_{ed} = G_{cv} d_h / \mu_{in} \quad (3.71)$$

Colburn (Kröger, 1998) proposed a method by which the heat transfer coefficient can be calculated from the Colburn j-factor, where

$$j = St Pr^{0.67} = \frac{N_{ud} Pr^{0.67}}{R_{ed} Pr} = \frac{h Pr^{0.67}}{G_{cv} c_p} \quad (3.72)$$

For tube banks of 4 or more tube rows, Nuntaphan (2000) proposed the following adjustment

$$j_{\geq 4} = 0.14 R_{ed}^{-0.328} \left( \frac{S_T}{S_L} \right)^{-0.502} \left( \frac{P_f - t_f}{d_o} \right)^{0.031} \quad (3.73)$$

Webb (1992) proposes the correction for rows less than four and is given by

$$j_N = j_{\geq 4} 0.991 \left[ 2.24 R_{ed}^{-0.092} \left( \frac{N_r}{4} \right)^{-0.031} \right]^{0.607(4-N_r)} \quad (3.74)$$

The thermal resistance across the finned surfaces is then given by

$$R_{e_o,co} = \frac{1}{(h_{e_o,co} A_{cvc} N_r L_{evap,cond} N_p / P_f)} \quad (3.75)$$

Kröger (1998) gives the following correlation for the pressure drop across the plate finned tube bundle as follows

$$\Delta P = \frac{G^2}{2} \left[ \frac{N_r f}{\rho_{am}} \left( \frac{A_{cva}}{A_{cvc}} \right) + (1 + \sigma^2) \left( \frac{1}{\rho_{ao}} - \frac{1}{\rho_{ai}} \right) \right] \quad (3.76)$$

Where the air mass velocity through the minimum free flow area of the core is

$$G = \dot{m} / (A_{fr} \sigma) \quad (3.77)$$

And  $A_{fr}$  represents the frontal area of the plate finned tube bundle. The mean density through the core given as

$$\rho_{a\_ave} = 2 / \left( \frac{1}{\rho_{ai}} + \frac{1}{\rho_{ao}} \right) \quad (3.78)$$

The friction factor is empirically based on the Reynolds number and geometric parameters and can be found in various literatures such as Kays and London (1984).

### 3.2.3 Plain individually finned tube configuration

Plain individually finned tubes consist of an array of annular finned tubes in which the fins are extruded or spirally wound onto the circular tubes. This configuration, illustrated in Figure 3.5, is generally used in the process industry and in combustion heat recovery. The method for determining the thermal resistance is analogous to the method proposed in Section 3.2.2 with the exception that different Colburn j-factors are introduced by Webb (1992). Figure 3.5 illustrates visually the individually finned tubes and Figure 3.6, the control volume for the tube configuration.

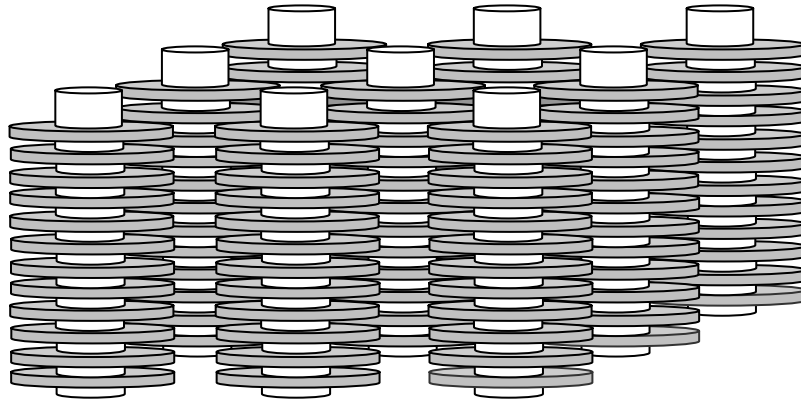


**Figure 3.5** Plain individually finned tube configuration

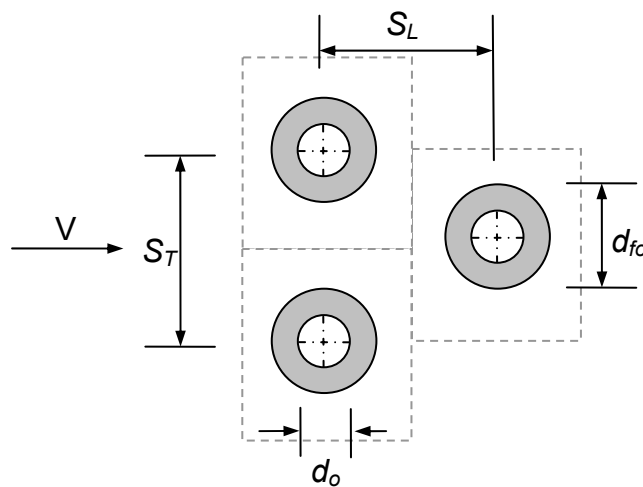


**Figure 3.6** Plain Individually finned tube control volume

For four or more tube rows,

$$j_4 = 0.134 R_{ed}^{-0.319} (s/e)^{0.2} (s/t_f)^{0.11} \quad (3.79)$$

And for  $N_r < 6$

$$j = j_4 \left( 1 + \frac{G_c}{\rho N_r^2} \right)^{-0.14} \quad (3.80)$$

The spacing between two fins,  $s$  is given by

$$s = (P_f - t_f) \quad (3.81)$$

And  $e$ , the fin height given by

$$e = (d_{fo} - d_o)/2 \quad (3.82)$$

The heat transfer coefficient is calculated from the Colburn j-factor with the thermal resistance given by equation 3.75. Shah and Giovanelli (1987) recommend the following correlation be used for the pressure drop calculation across the plain individually finned tube configuration (Faghri, 1995)

$$\Delta P = 2N_r f \frac{G^2}{\rho_{ai}} + G^2 \left( \frac{1}{\rho_{ao}} - \frac{1}{\rho_{ai}} \right) \quad (3.83)$$

Where for their correlation

$$G = \dot{m} / A_{fr} \quad (3.84)$$

Again, the friction factor correlations are empirically based on the Reynolds number and geometric parameters. Robinson and Briggs (1996) recommend the following correlation be used for the friction factor (Faghri, 1995)

$$f = 9.465 R_{eD}^{-0.316} \left( \frac{S_T}{d_o} \right)^{-0.937} \quad (3.85)$$

### 3.3 Air Drier Model

As it was decided to test a demonstration HPHE on an air drier unit in a field application, a standard air drier is modelled such that many typical drying applications can be simulated. For the model it is necessary to utilise standard psychrometric theory to obtain the humidity ratios and moisture contents at the various stages in the drier. From this model, a computer program is generated in which the various temperatures, fan and heating capabilities are entered in as variables and the resulting moisture contents of the air at various stages in the drier are obtained. The following equations are used in determining the air properties at the various stages in the drier (Johannsen, 1981). The computer program is described in Appendix C.

It is first necessary to calculate the saturated water vapour pressure,  $P_{ws}$

$$P_{ws} = 22.087837 \times 10^6 \times \exp^P \quad (3.86)$$

Where

$$P = \frac{0.01}{(T_{db} + 273.15)} \times (374.136 - T_{db}) \times \sum_{i=1}^8 \left[ F(i) \times (0.65 - 0.01T_{db})^{i-1} \right] \quad (3.87)$$



And

$$\begin{aligned}
 F_1 &= -741.9242 & F_5 &= 0.1094098 \\
 F_2 &= -29.721 & F_6 &= 0.439993 \\
 F_3 &= -11.55286 & F_7 &= 0.2520658 \\
 F_4 &= -0.8685635 & F_8 &= 0.05218684
 \end{aligned}$$

It is then necessary to calculate the humidity ratio,  $\omega_s$  at the wet bulb temperature

$$\omega_s = \frac{0.62198 \times f \times P_{ws@T_{wb}}}{Baro - f \times P_{ws@T_{wb}}} \quad (3.88)$$

Where

$$Baro = 101325 \times \left(1 - 22.55691 \times 10^{-6} \times Alt\right)^{5.2561} \quad (3.89)$$

And where  $f$  is a correction factor given by  $f = 1.005$ . It is then possible to calculate the humidity ratio,  $\omega$  of the air at the dry bulb temperature

$$\omega = \frac{(2501.6 - 2.3263 \times T_{wb}) \times \omega_s - 1.00416 \times (T_{db} - T_{wb})}{2501.6 + 1.8577T_{db} - 4.184T_{wb}} \quad (3.90)$$

The vapour pressure is then calculated from

$$P_v = \frac{Baro \times \omega}{f \times (0.62198 + \omega)} \quad (3.91)$$

The relative humidity,  $\phi$  is then calculated from

$$\phi = \frac{P_v}{P_{ws}} \quad (3.92)$$

The enthalpy,  $h$  can also be calculated and is given by

$$h = 1.00416T_{db} + \omega(2501.6 + 1.8577T_{db}) \quad (3.93)$$

And the specific volume is given by

$$v = \frac{287.052 \times (T_{db} + 273.15)}{Baro} \times (1 + 1.6078\omega) \quad (3.94)$$

From which the density can be calculated. Figure 3.7 illustrates the air drier that is being modelled with its corresponding psychrometric chart.

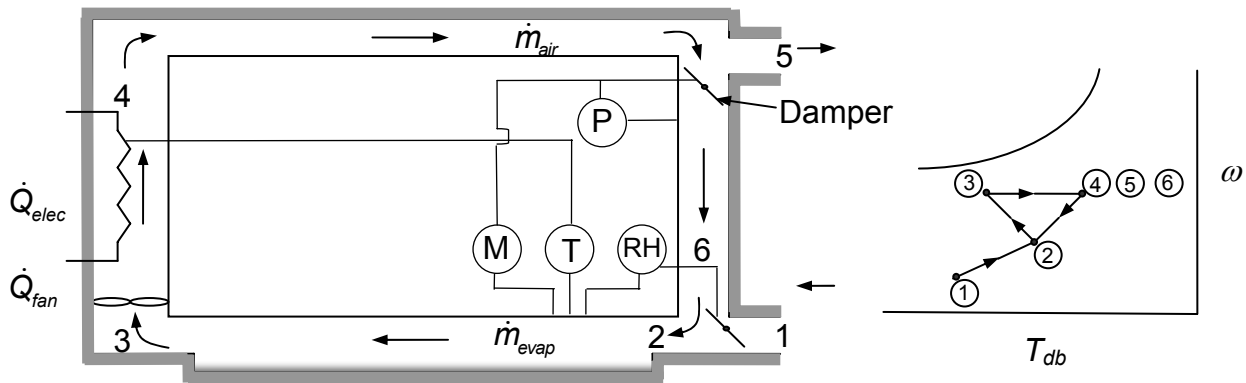


**Figure 3.7** The drier unit model and corresponding psychrometric chart

From Figure 3.7, the air enters the drier at position 1, where it is mixed with recirculated air from position 6 at a specified percentage based on the damper position at 5. From here, the air then passes over section 2-3 where the product to be dried is situated. It is in this process that the moisture is evaporated from the product. From section 3, the air is then blown and heated by some form of heating device till it reaches section 4 and passes to section 5 where the process repeats itself. From Figure 3.7, it can be seen that

$$\omega_3 = \omega_4 = \omega_5 = \omega_6$$

With

$$r = \frac{\dot{m}_6}{\dot{m}_5} \quad (3.95)$$

$$\omega_2 = r\omega_6 + (1-r)\omega_1 \quad (3.96)$$

$$\therefore \omega_2 = r\omega_5 + (1-r)\omega_1$$

And that

$$h_2 = rh_5 + (1-r)h_1 \quad (3.97)$$

The properties at position 1 and 5 of the drier are then calculated using equations 3.86-3.94. From equation 3.92

$$h_2 = 1.00416T_{db2} + \omega_2(2501.6 + 1.8577T_{db2}) \quad (3.98)$$

From which  $T_{db2}$  can be calculated

$$T_{db2} = \frac{h_2 - \omega_2 \times 2501.6}{1.00416 + 1.8577\omega_2} \quad (3.99)$$

The humidity ratio at position 3 is then calculated from

$$\omega_3 = \frac{\dot{m}_{evap}}{\dot{m}_{air}} + \omega_2 \quad (3.100)$$

Where  $\dot{m}_{evap}$  is calculated using either equation 2.13 or 2.14. Alternatively, experimentally determined values for  $\dot{m}_{evap}$  can be used as was the case for the computer simulation code described in Appendix C (Dobson, 2001).

The enthalpy at position 3 is then calculated from

$$h_3 = h_2 + \dot{m}_{evap} h_{fg@T_{wb2}} \quad (3.101)$$

Where

$$h_{fg} = -3.027 \times 10^{-7} T_{wb}^4 + 1.682 \times 10^{-4} T_{wb}^3 - 3.54 \times 10^{-2} T_{wb}^2 + 0.1681 T_{wb} + 2457 \quad (3.102)$$

The  $T_{db3}$  temperature can then be calculated using equation 3.99 by replacing the subscript, 2 with the subscript 3. The enthalpy at position 4 can then be calculated from

$$h_4 = h_3 + \frac{Q_{elec} + Q_{fan} - Q_{loss}}{\dot{m}_{air}} \quad (3.103)$$

Again, from which the  $T_{db4}$  temperature can be calculated using equation 3.99 and hence all the properties are known at the various positions in the drier.

## 4 DESIGN OF A DEMONSTRATION HPHE

This section discusses the procedures followed in the design of a demonstration HPHE including the design criteria and specifications. The demonstration unit is to be installed on an existing air drier unit in a factory.

### 4.1 Design Criteria and Specifications

Various factors need to be considered in the design of a HPHE, specifically in the operation of the thermosyphons from which the HPHE is constructed. These factors all play an important role in the operation of the HPHE. However, it is difficult to link all these factors together to obtain the 'perfect' exchanger. As a result, the factors that are most prominent in the operation of the exchanger are considered in the design philosophy and include:

- The operating temperatures and pressures and the respective relative humidity's for the design application.
- The environmental conditions surrounding the HPHE. For instance, whether or not the HPHE will be exposed to fouling or corrosive contaminants in the flow field or not. The dew points need to be determined to evaluate the corrosive nature of the flow field.
- The diameters of the individual thermosyphons which will affect the flooding and entrainment limits.
- The tube, header and fin materials.
- The tube and header wall thicknesses to allow for pressure and the possibility of corrosion.
- The lengths of the evaporator and condenser sections which also affect the flooding and entrainments limits.
- The working fluid which is dependant on the required vapour temperature and pressure.
- The face velocity of the air on the HPHE as this influences the heat transfer rate.
- The configuration of the fins on the HPHE.

Continental Fan Works (CFW), under management of Mr. R. Raad (Jr.), was willing to provide assistance in the testing of the demonstration HPHE to determine the economic viability of such a device for practical application. Yucon manufactured the HPHE according to the desired specifications given in Table 4.1.

**Table 4.1** Design specifications for the CFW/Yucon HPHE

Design pressure	Atmospheric pressure at sea level
Inlet hot temperature	40 – 60 °C
Inlet cold temperature	Ambient air
Mass flow of the air into the condenser section	0.72 kg/s
Mass flow of the air into the evaporator section	0.72 kg/s

CFW (Mr. Raad as a private communicator) felt that it was not necessary for the demonstration model to have a defined outlet temperature, but that an economic evaluation of the HPHE would substantiate its use, should acceptable outlet temperatures be obtained.

Other requirements that were believed to be necessary in the design included

**Safety:**

- The working fluid inside the thermosyphon tubes of the HPHE must not be able to escape into the atmosphere, preventing harm to the environment and nearby workers.
- Any electrical components must be secured and well protected against possible high temperatures.

**Mobility:**

- The HPHE must be fixed to the necessary ducting and should be allowed to be easily detached should any maintenance be required.
- The HPHE should also be easy to install into the current application setup.

**Durability:**

- The HPHE must be corrosion resistant. Hence, the working fluid chosen should not react with the tube material.
- Should contaminants be present in the air flow, a protective coating on the entire HPHE should be used to prevent corrosion of the thermosyphon tubes and fins.

**Size:**

- The HPHE must be able to be incorporated into an existing setup in which the spatial constraints might be limited.

A computer program based on the thermal modelling in Section 3 was developed to aid in the design of the HPHE. In the program, the various design variables such as the physical and geometrical inputs are entered in as variables. The program then undergoes various iteration processes using these inputs and gives new desired outputs. Should the outputs not comply with what is desired, the geometrical inputs can be altered, the iteration process continued and new outputs obtained. The user of the computer program soon develops a feel for the program and the process of altering the inputs becomes easier. A detailed user-manual for the computer program is given in Appendix C. Figure 4.2 illustrates the flow diagram for the operation of the computer program and Table 4.2 illustrates the design inputs for the CFW/Yucon HPHE. Appendix D gives the detail drawing of the CFW/Yucon HPHE.

**Table 4.2** Design inputs for the CFW/Yucon HPHE.

Working Fluid	R134a	
Inlet hot temperature	50	°C
Inlet cold temperature	22	°C
Desired outlet cold temperature	30	°C
Evaporator air mass flow rate	0.72	kg/s
Condenser air mass flow rate	0.72	kg/s
Tube bank configuration	Plate-and-tube	
Evaporator length	0.35	m
Condenser length	0.35	m
Number of tube rows	6	
Number of tubes per row	11	

Longitudinal pitch	0.0381	m
Transverse pitch	0.0381	m
Fin pitch	10	Fins/in
Fin thickness	0.0002	m
Outside diameter of tubes	0.01588	m
Inside diameter of tubes	0.01490	m

The CFW/Yucon HPHE was then designed using the computer simulation program based on the CFW design specifications given in Table 4.1. The results are given in Table 4.3, with the temperatures between each row being calculated and the total heat transfer rate given. The row by row configuration is given in Figure 4.1.

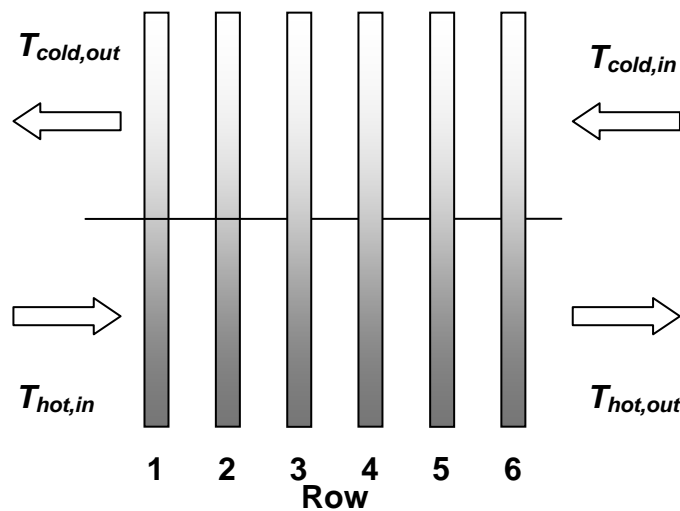


**Figure 4.1** Row configuration for the CFW/Yucon HPHE

**Table 4.3** CFW/Yucon HPHE results from the computer simulation program

	Inlet, Outlet	Row 1-2	Row 2-3	Row 3-4	Row 4-5	Row 5-6	Outlet, Inlet
Hot Temperature [°C]	50	47.87	45.73	43.6	41.46	39.32	37.19
Cold Temperature [°C]	34.82	32.69	30.55	28.41	26.28	24.14	22
Total Pressure Drop [Pa] (Using Equation 3.76)	281.53						
Total heat load [W] ( $\dot{Q}_{evap} = \dot{Q}_{cond}$ )	9297.95						

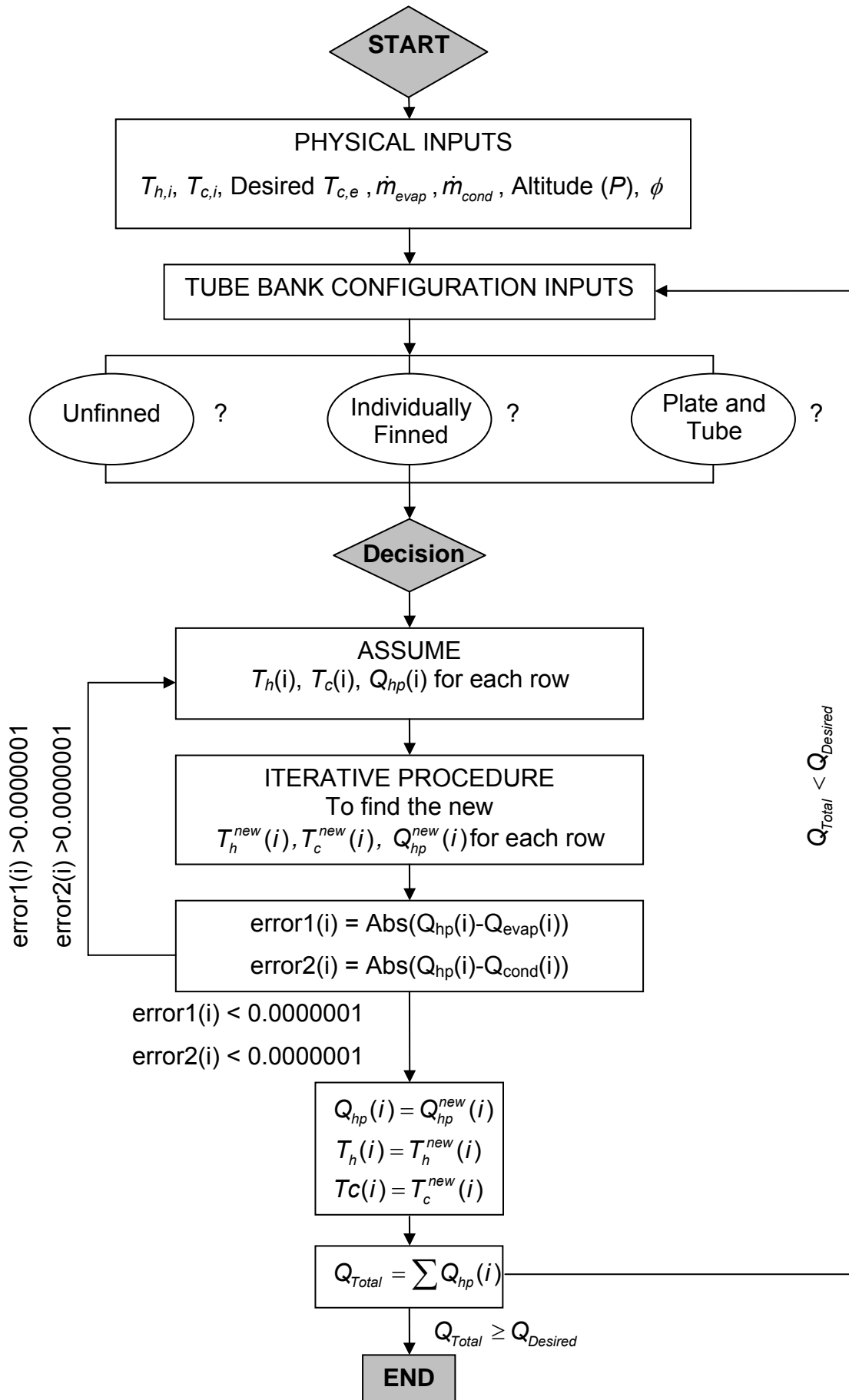


**Figure 4.2** Flow diagram for the HPHE computer simulation program



## 5 EXPERIMENTAL WORK

This section discusses the experimental work. The necessary procedures, equipment and calibration techniques will also be discussed. The experimental work is grouped into four sub-sections:

- Experimental determination of the thermosyphon thermal characteristics,
- Investigation into the inside temperature distribution of a HPHE,
- The economic analysis of a demonstration HPHE in a practical application, and
- The equipment and calibrations used for the experiments

### 5.1 Experimental Determination of the Thermosyphon Thermal Characteristics

#### 5.1.1 Thermosyphon description

Three copper thermosyphons and a stainless steel thermosyphon, all of different diameters were used in the experiments. The objective of these experiments was to determine the inside evaporator and condenser heat transfer coefficients for different thermosyphon geometries. The diameters of the copper pipes used for the thermosyphons had ID's of 14.99, 17.272 and 22.23 mm. The copper thermosyphons all had the same evaporator to condenser length ratio of 1. The stainless steel thermosyphon had an ID of 31.9 mm with an evaporator to condenser length ratio of 0.24. Table 5.1 gives detailed characteristics of the thermosyphons used.

The effects of four independent variables on the heat transfer coefficient were experimentally evaluated. These variables included the evaporator to condenser length ratio, the total (evaporator and condenser) length, diameter and the orientation of the thermosyphon to the horizontal.

For the purpose of this thesis, liquid fill charge ratios of 50 % based on the evaporator length of the thermosyphons were used. Research suggests that liquid fill charge ratios in the region of 50 % are acceptable and that good heat transfer rates are achieved (see Section 2.2.2). The liquid fill charge ratio was kept at 50 % to limit the number of

experiments. As the heat source facilities were limited, low temperature working fluids: refrigerant R134a and Butane, were chosen as the working fluids. The thermosyphon experiments were all undertaken at an orientation angle of 90° and 45° to the horizontal.

**Table 5.1** Detailed characteristics of the experimental thermosyphons

	<b>Material</b>	<b>ID [mm]</b>	<b>OD [mm]</b>	<b><math>L_{evap}</math> [m]</b>	<b><math>L_{cond}</math> [m]</b>	<b>ID Cooling Jacket [mm]</b>
5/8"-Thermosyphon	Copper	14.9	15.88	1	1	20.193
3/4"-Thermosyphon	Copper	17.272	19.05	1.03	1.03	26.543
7/8"-Thermosyphon	Copper	20.193	22.225	1.03	1.03	26.543
5/4"-Thermosyphon	Stainless Steel	31.9	34.9	1.2	5	42.1

### 5.1.2 Thermosyphon experimental set-up

To increase the amount of data acquisition, two or three thermosyphons were tested simultaneously. This was achieved by mounting the thermosyphons on a support structure which consisted of a wooden rotateable fixture on which the thermosyphons could be mounted. This rotateable fixture was then bolted on a mounting fixture which consisted of a circular disk with 15° spaced locating holes. Figure 5.1 illustrates the set-up. The rotateable fixture could then be mounted at the desired orientation angle. For the water supplies, the outlet water of the one thermosyphon would in effect be the inlet water for the next thermosyphon.

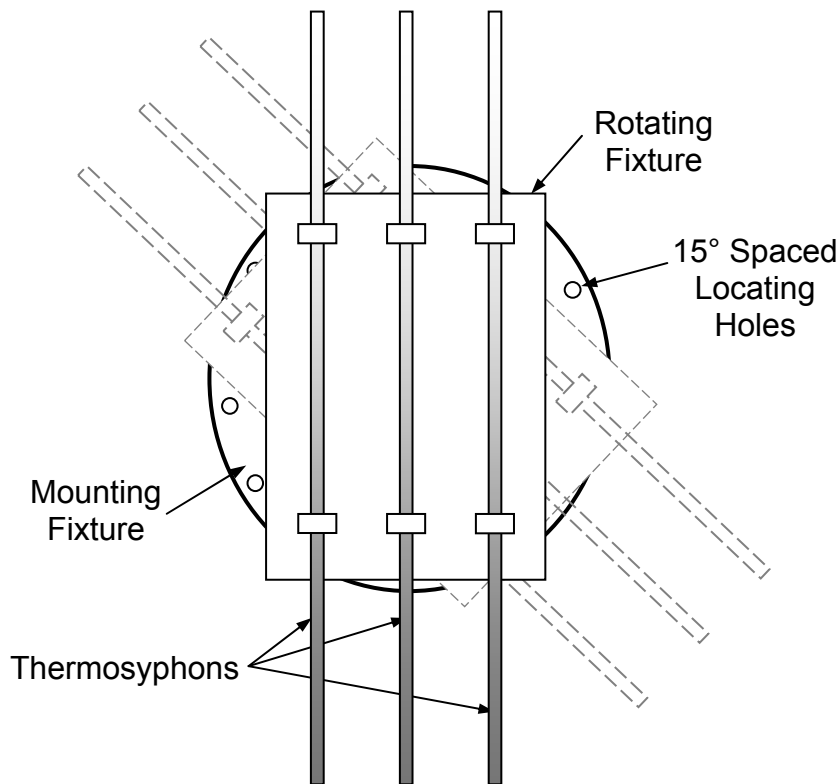


**Figure 5.1** The thermosyphon support structure

To supply the evaporator sections of the thermosyphons with a suitable heat source, a 1800 L hot water supply tank system in the laboratory was used. This water could be heated up to 80 °C by elements situated in the tank. This limitation on the maximum that the water can be heated up to, might result in the inside temperatures not being able to reach high enough temperatures for flooding to occur (which is necessary in determining the maximum heat transfer rate of the working fluid). Hence, this aided in the decision to use medium temperature range fluids such as R134a and Butane which would reach high enough temperatures with the hot water supply system.

A 2400 L cold water supply tank was used to supply the condenser sections of the thermosyphons with cold water. This cold water provides for the temperature difference between the top and bottom of the thermosyphon such that the thermosyphon will start to operate. This water could be passed through a chiller and cooled down to 5 °C. Figure 5.2 illustrates the water tank systems with their supply lines to an individual thermosyphon.

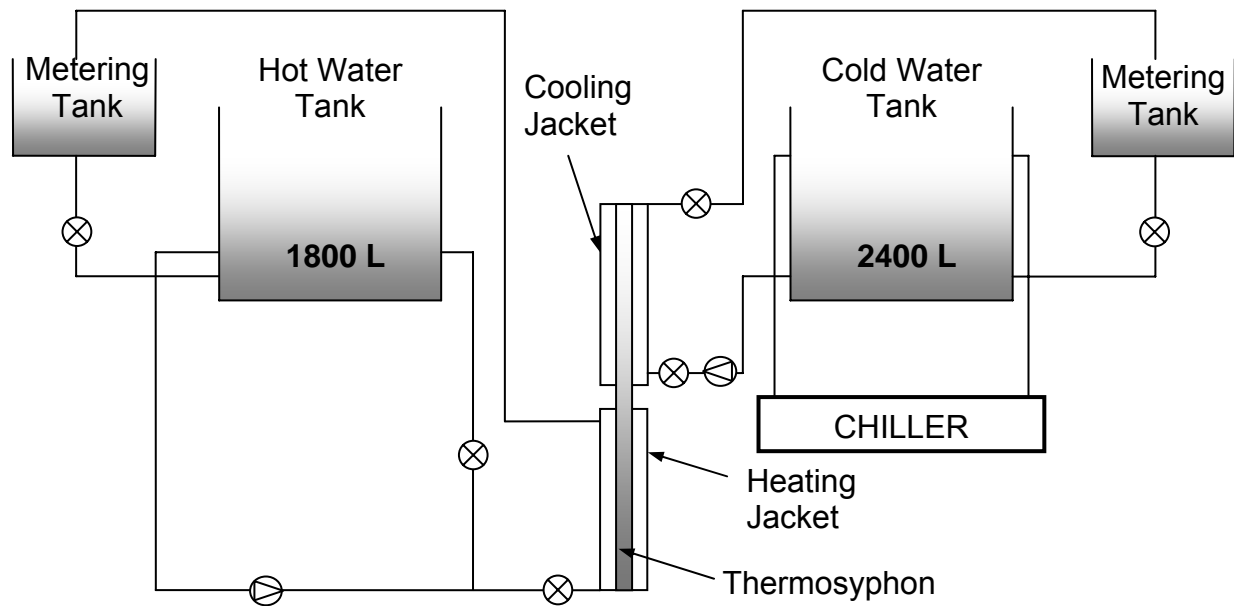


**Figure 5.2** Thermosyphon heating and cooling water tank systems

To determine the heat transfer rate that is supplied to the thermosyphon and that is recovered from the thermosyphon to the cold water supply, various measurements are needed. These include measuring the mass flow rates of both the cold and hot water supplies and also measuring temperatures at various positions on the thermosyphon. In measuring the water temperatures, it is important that the thermocouples do not touch the supply line pipe walls as this might result in erroneous readings in temperature. The temperatures were measured using type-T thermocouples and the data was logged with a Schlumberger data logger. The thermosyphons were tested prior to the experiments to ascertain the accuracy of the measurements. However, this could not be done for each experiment as removing the thermocouples would result in leakage of the working fluid from the thermosyphon and leakage of water from the supply lines. The temperature measurements are illustrated in Figure 5.3 for a single thermosyphon and include:

$T_{top}$	Inside vapour temperature at the top of the thermosyphon
$T_{bottom}$	Inside working fluid temperature at the bottom of the thermosyphon
$T_{hw,i}$	Inlet hot water temperature to the heating jacket
$T_{hw,e}$	Exit hot water temperature from the heating jacket
$T_{cw,i}$	Inlet cold water temperature to the cooling jacket
$T_{cw,e}$	Exit cold water temperature from the cooling jacket

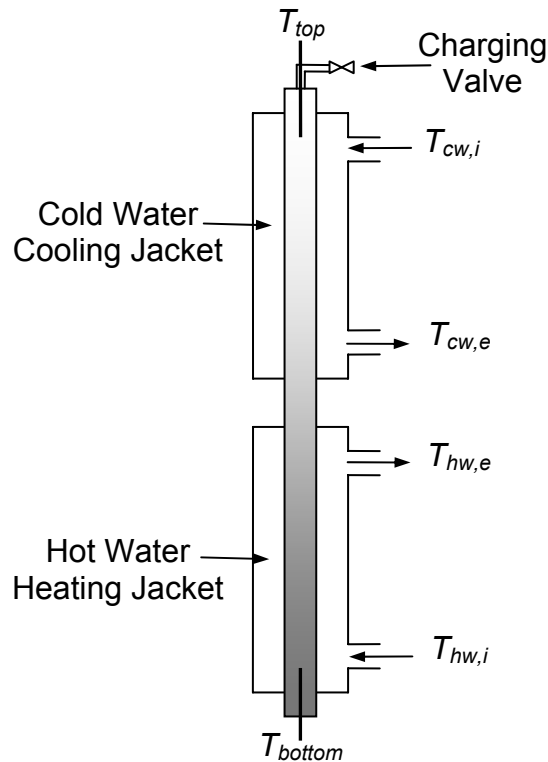


**Figure 5.3** Thermosyphon temperature measurement positions

As it is important that no air is present in the thermosyphon, it is essential that a complete vacuum is drawn before charging the thermosyphon with the working fluid. Two charging procedures were investigated during the course of the experiments. For the first procedure a standard single stage vacuum pump and scale were used as shown in Figure 5.4. The procedure is as follows:

- The bottle, in which the fluid is held, is heated to obtain a higher pressure such that the charge flows from the bottle to the thermosyphon. For safety reasons, it is important that not too high a pressure is obtained and hence this must be carefully monitored.
- The bottle is placed on the scale and the scale zeroed.
- Valves 1, 2 and 3 are opened and a vacuum is drawn from the thermosyphon and the connecting supply line.
- Valve 2 is then closed and valve 4 of the bottle opened such that the weighted amount can be read off from the scale. Valve 4 is then closed.
- Valves 2 and 3 are then closed, the thermosyphon charged and disconnected from the bottle and vacuum pump.

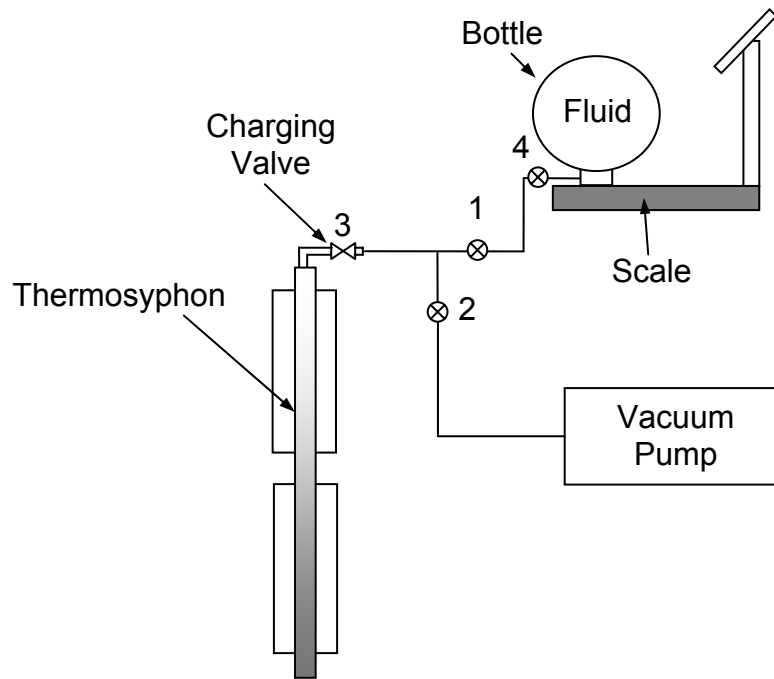


**Figure 5.4** Connectivity of the charging device to the thermosyphon

It was found that this procedure was not accurate enough for small charges as the sensitivity of the scale ( $\pm 0.005\text{kg}$ ) affected the charge significantly. However, when large amounts of charge were used, it was deemed accurate enough. For the second charging procedure, a charging device was constructed which aimed at obtaining accurate measurements for small charges. This measuring device was taken from a standard refrigeration rotameter and adapted to allow for the necessary fittings. The charging device was calibrated and is illustrated in Figure 5.5.

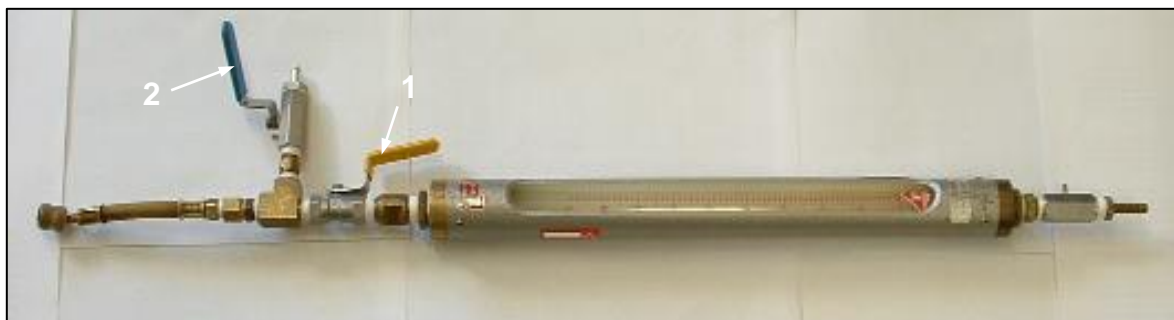


**Figure 5.5** The charging device

Figure 5.6 illustrates the connectivity of the charging device to the thermosyphon and the charging procedure is as follows:

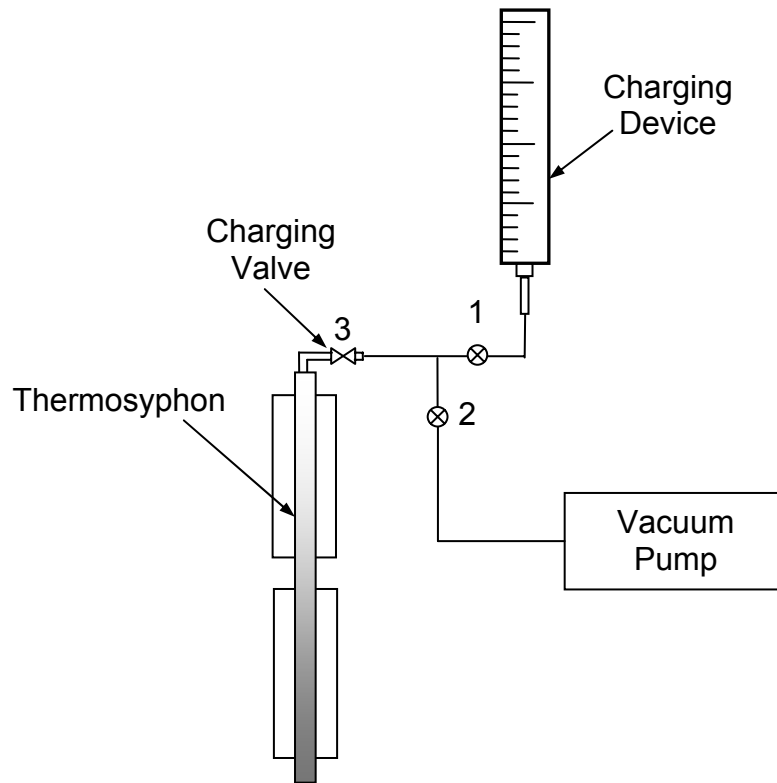


**Figure 5.6** Connectivity of the charging device to the thermosyphon

- The charging device is cooled in ice-water such that the bottle temperature, in which the charge fluid is kept, is higher than the measuring devices.
- The device is then connected to the bottle and vacuum pump.
- Valves 1 and 2 are opened and a vacuum is drawn from the charging device and supply line.
- Valve 2 is closed and the valve on the bottle is opened. The working fluid is then filled to the desired level in the charging device.
- The bottle's valve and valve 1 are then closed and the charging device disconnected.
- The charging device is then immersed in a hot water bucket such that the fluid inside the charging device starts to boil.
- The measuring device is then connected along with the vacuum pump to the thermosyphon.
- Valves 2 and 3 are then opened and vacuum is drawn from the thermosyphon and supply line, keeping valve 1 closed.

- Valve 2 is then closed and valves 1 and 3 opened such that the working fluid flows into the thermosyphon.
- Valve 3 is closed, the thermosyphon charged and the charging device disconnected.

Should more working fluid be required than what the charging device can hold, the above procedure is continued until the thermosyphon is charged with the necessary amount of working fluid.

To further ensure that no air was present in the thermosyphon, it was necessary to heat the working fluid up to a temperature such that a positive pressure relative to the surroundings was obtained inside the thermosyphon. The reason for this is that any air will then be dragged up to the top (during operation) of the thermosyphon where it can be briefly purged into the atmosphere. However, as the hot water supply only reaches 80 °C, it was decided to heat the water to 100 °C using a jug of boiling water. The water would then be poured into the heating jacket were it would heat the fluid. The inside temperatures were carefully monitored such that excess pressures inside the thermosyphon were prevented. When satisfactory positive pressures were obtained, valve 3 (see Figures 5.4 and 5.6) was briefly opened and the air purged. Figure 5.7 gives a visual image of the thermosyphon experimental set-up.

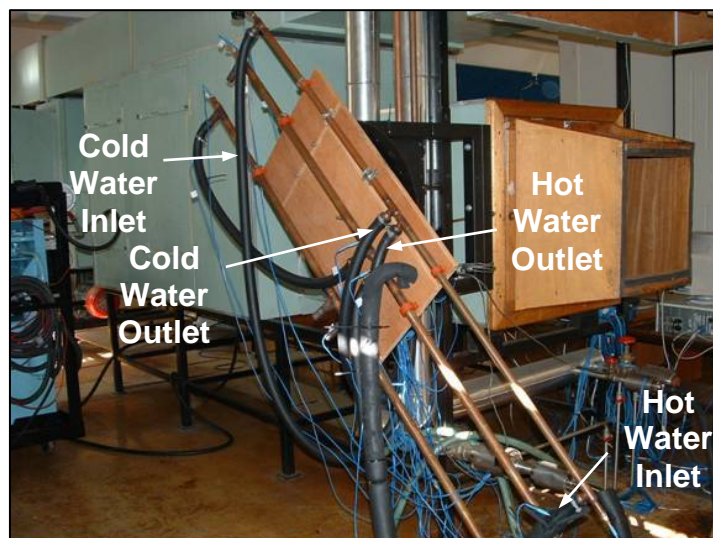


**Figure 5.7** The thermosyphon experimental set-up



### 5.1.3 Thermosyphon experiments undertaken

*Measuring water mass flows:* Cold water mass flow rates were measured using a bucket, scale and a stopwatch. The cold water supply was turned on and the mass of water returning to the metering tank (see Figure 5.2) measured over a 10 second time period. This was done three to four times and the values averaged. A typical experimental run would give results of 0.513, 0.52 and 0.53 kg/s from which the mass flow rate of 0.52 kg/s is calculated.

To measure the hot water mass flow, a similar technique was used were the valve to the metering tank of the hot water supply line was closed. Markings exist on the metering tank that indicates a specified volume (0.0518 m<sup>3</sup> at 17 °C) of water between two marked points on the tank. The volume of water is then divided by the time that it takes the water to fill the metering tank between the markings and this volume is then adjusted for the specific water temperature. The mass of water is then calculated over the measured time period. To obtain accurate mass flows, the flow rate was adjusted such that the measuring time was longer than one minute but with the temperature difference between the hot water inlet and outlet to the thermosyphon, being not more than 3° C.

*Heat losses to the environment:* The heat losses to the environment generally only occur in the evaporator section of the thermosyphon as the temperatures are high here. During the experiments, the presence of condensate on the outside walls of the condenser sections of the thermosyphons was non-existent and losses due to condensation were therefore ignored. In order to calculate the heat losses from the thermosyphons, a vacuum was drawn from each of the thermosyphons. The water supplies were then connected and the mass flows measured. An experiment was then undertaken in which the hot water temperature was raised in 5 °C increments and allowed to stabilize at these incremental temperatures. The heat transfer rate was then calculated from the temperature differences between the inlet and outlet of the water supplies at these incremental temperatures using

$$\dot{Q} = \dot{m}c_p\Delta T \quad (5.1)$$

Where  $c_p$  is the specific heat of the water and  $\dot{m}$  the mass flow rate. Figure 5.8a and 5.8b illustrates the heat loss results obtained for the 5/8" and the 3/4" copper thermosyphons.

The erratic behaviour in the data indicates unsatisfactory results and the fact that such high heat loss values are obtained indicate errors. Another factor that aided in realizing that the data was incorrect, was the fact that most of the calculated heat losses from Figure 5.8a and 5.9b were higher the heat that was actually transferred to the thermosyphons when compared to actual thermosyphon experiments operating with a working fluid. These experiments for the heat losses were repeated and the same pattern of results observed. It was then decided not to do the experiment on the 7/8" thermosyphon and that standard heat loss theory would rather be used to calculate the losses from all the thermosyphons.

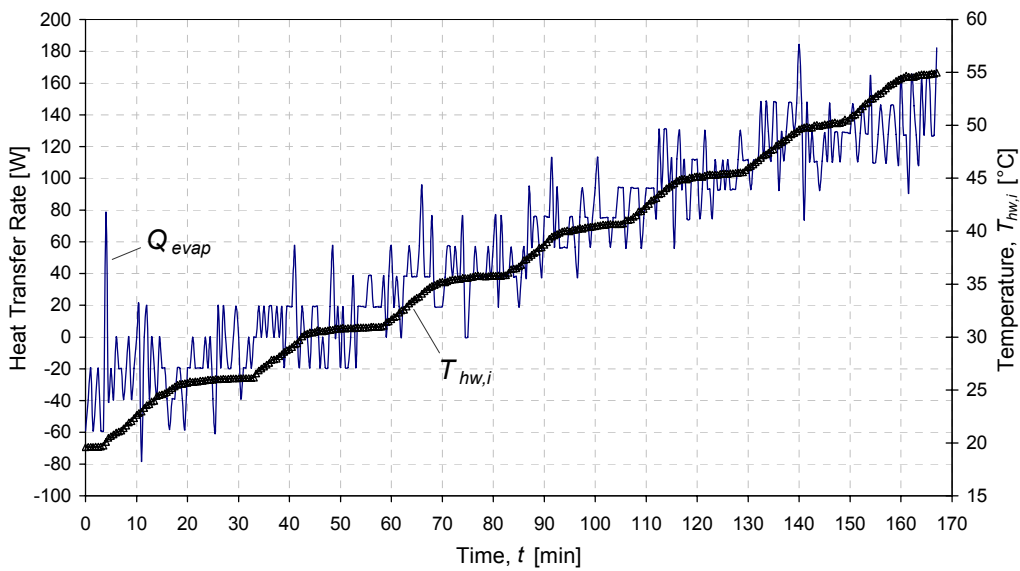


**Figure 5.8a** Experimental heat loss for the 5/8"-Thermosyphon

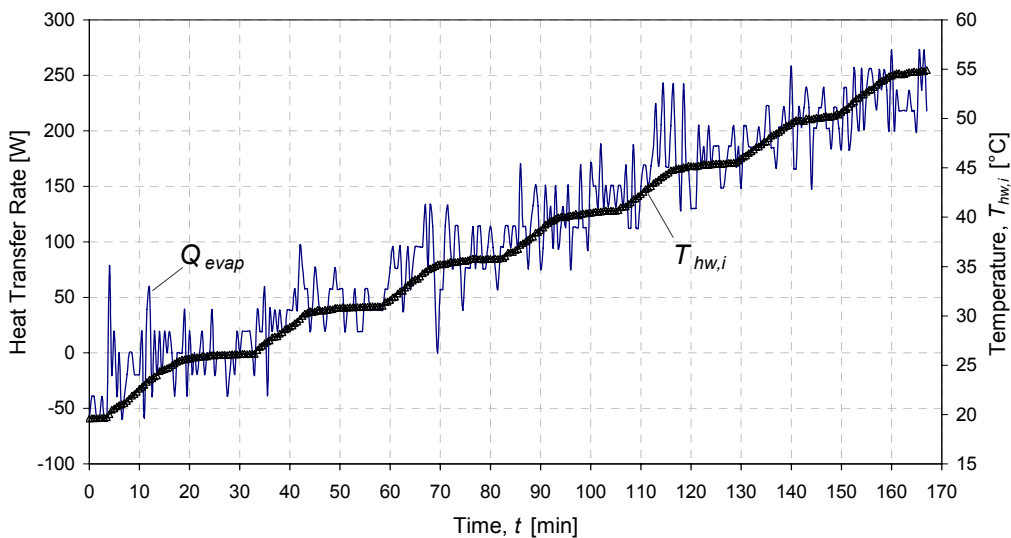


**Figure 5.8b** Experimental heat loss for the 3/4"-Thermosyphon

For laminar and turbulent-natural convection, equations 3.44 and 3.45 are used to calculate the convective heat transfer coefficients. For the radiative heat transfer coefficients, the following equation was used (Mills, 1995)

$$h_r = 4\varepsilon\sigma\left(\frac{T_{wall} + T_{amb}}{2}\right)^3 \quad (5.2)$$

Where the wall temperature is taken as the average between the inlet and outlet temperature of the hot water. From the convective and radiative heat transfer coefficients, the heat losses to the environment were calculated and trend-lines plotted to obtain these losses as functions of temperature. The following equations represent these losses as functions of the temperature difference between the wall and the ambient temperature of 20 °C. Figure 5.9 illustrates the heat losses. These losses are then adjusted for when calculating the actual heat transfer rates from the evaporator sections of the thermosyphons. Appendix B gives the sample calculations.

$$Q_{loss\_5/8''} = 1.442 \times 10^{-3} (T_{wall} - T_{amb})^2 + 0.2721 (T_{wall} - T_{amb}) - 0.4734 \quad (5.3)$$

$$Q_{loss\_3/4''}, Q_{loss\_7/8''} = 1.852 \times 10^{-3} (T_{wall} - T_{amb})^2 + 0.3493 (T_{wall} - T_{amb}) - 0.6079 \quad (5.4)$$

$$Q_{loss\_5/4''} = -3.101 \times 10^{-5} (T_{wall} - T_{amb})^3 + 7.279 \times 10^{-3} (T_{wall} - T_{amb})^2 + 0.4701 (T_{wall} - T_{amb}) - 0.466 \quad (5.5)$$

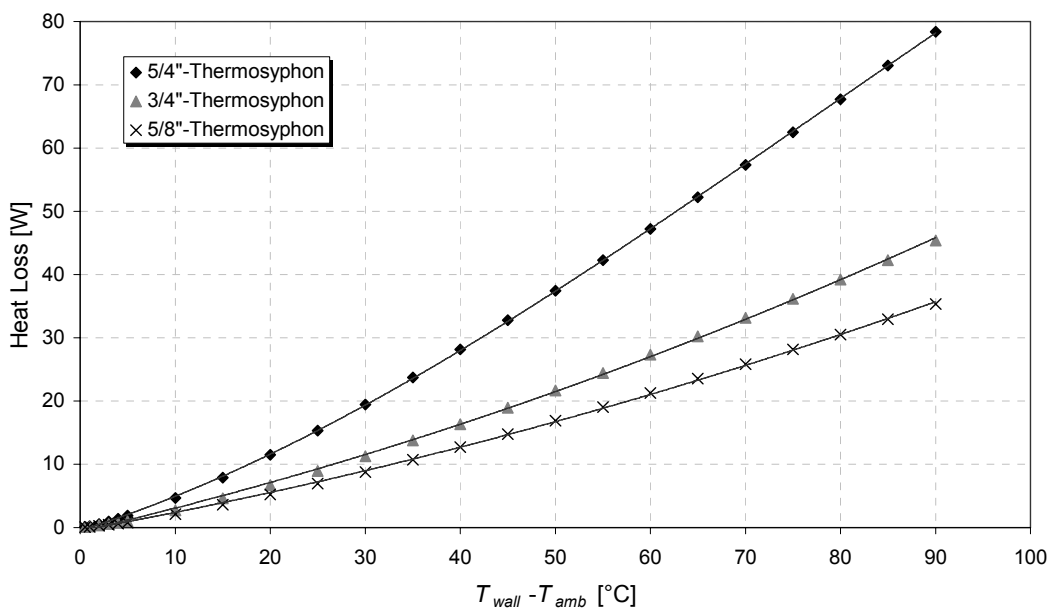


**Figure 5.9** Theoretical heat losses for the thermosyphons with  $T_{amb} = 20$  °C

## 5.2 Investigation into the Temperature Distribution of a HPHE

### 5.2.1 HPHE description

A relatively small HPHE is used in the investigation into the temperature distribution inside the rows of a HPHE in which in each row is connected to a pipe header. The HPHE was locally manufactured (Yucon, 2003) and consists of three separate rows of 5/8" copper tubes (representing thermosyphons) with pipe headers as illustrated in Figure 5.10. Aluminium fins are used to increase the heat transfer rate and the casing is manufactured from galvanized steel. A separator plate is used to separate the evaporator and condenser sections of the HPHE and also aids as a mounting bracket when the HPHE is mounted to the necessary ducting. The HPHE is charged with R134a with a liquid fill charge ratio of 50 % based on the evaporator length. Table 5.2 lists the HPHE design characteristics:

**Table 5.2** Design characteristics of the HPHE

Working Fluid	R134a	
Tube bank configuration	Plate-and-tube	
Evaporator length	0.204	m
Condenser length	0.204	m
Width	0.306	m
Depth	0.1	m
Number of tube rows	3	
Number of tubes per row	8	
Longitudinal pitch	0.0381	m
Transverse pitch	0.0381	m
Fin pitch	12	Fins/in
Fin thickness	0.0002	m
Outside diameter of tubes	0.01588	m
Inside diameter of tubes	0.01490	m

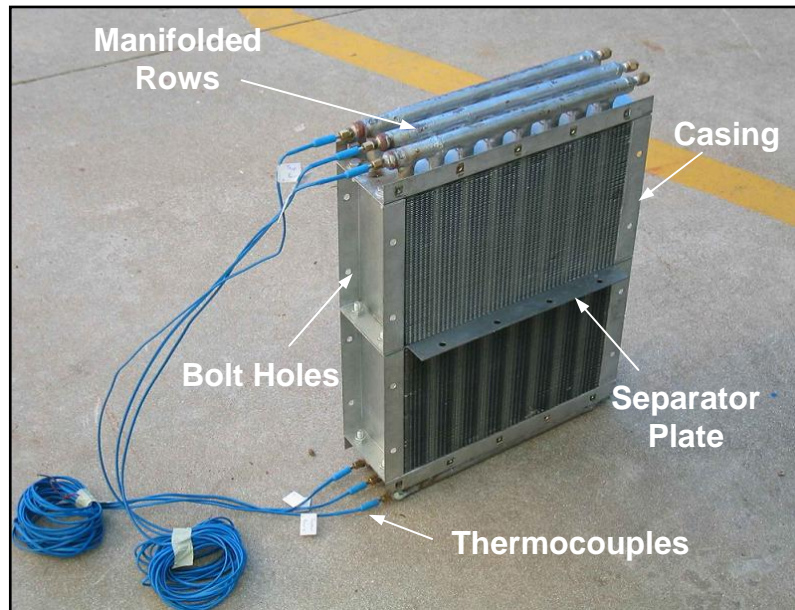


**Figure 5.10** The HPHE used in the inside temperature distribution experiments

### 5.2.2 HPHE experimental set-up

The HPHE was installed into a wind tunnel set-up as shown in Figure 5.12b. Figure 5.12a gives a visual image of the experimental set-up. As can be seen, a tunnel section was constructed whereby two air streams could flow. The upper tunnel section is used for the cold air stream and the lower for the hot air stream. This hot air stream represents the heat source supplied to the evaporator section of the HPHE. In order to obtain this hot air, two water heated heat exchangers are placed in front of the wind tunnel. Hot water from the supply tank system (see Figure 5.2) is passed through the lower heat exchanger which heats up the air that passes through this section of the tunnel. The upper heat exchanger is used to supply the same pressure drop as the lower heat exchanger; however, no water is passed through this exchanger.

In order to measure the flow rates through each tunnel section, an anemometer is used. A range of readings are taken for each tunnel section and the values averaged. Once the temperatures and velocities of the respective sections are known, the mass flow rate can then be calculated from

$$\dot{m} = \rho VA \quad (5.6)$$

$V$  is the measured velocity and  $A$  is the tunnel section area. The density is adjusted for the respective tunnel section temperatures. As can be seen from Figure 5.11, nine different temperature readings are taken for the inlet and outlet temperature readings of each tunnel section which are then averaged. The cold and hot air stream tunnel sections are symmetrical and have dimensions of 0.306 x 0.204 m.

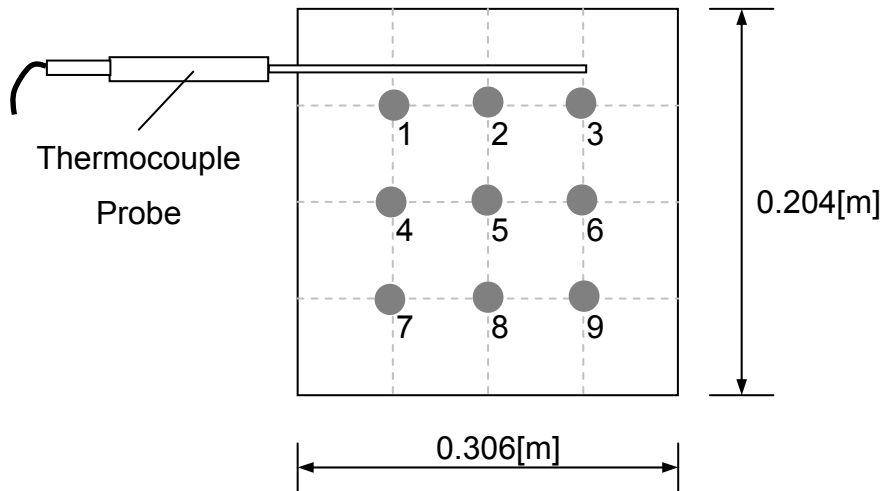


**Figure 5.11** Temperature and velocity measurement matrix (front view)

To measure the inside temperatures of the individual rows of the HPHE, thermocouples were inserted at the top and bottom manifolds of the HPHE (see Figure 5.10). It is important that these thermocouples do not touch the copper walls as incorrect fluid inside temperatures might be measured. The pressure drop across the HPHE is measured using a differential pressure transducer.

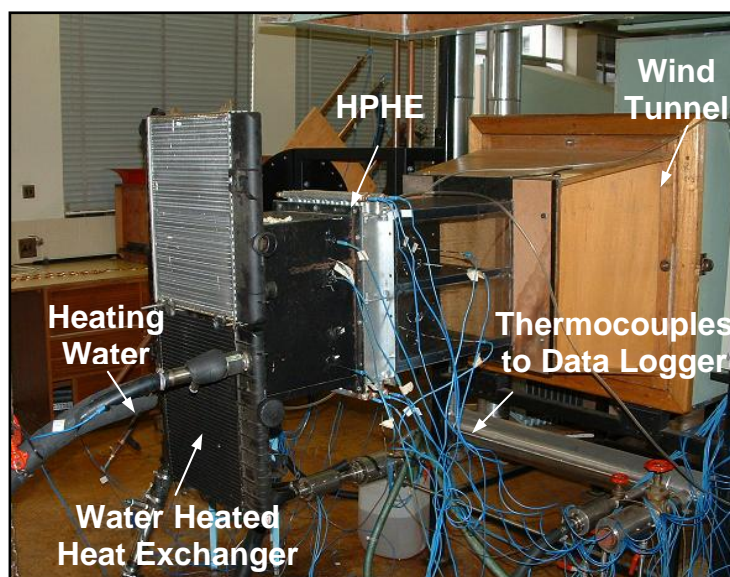


**Figure 5.12a** The HPHE wind tunnel set-up

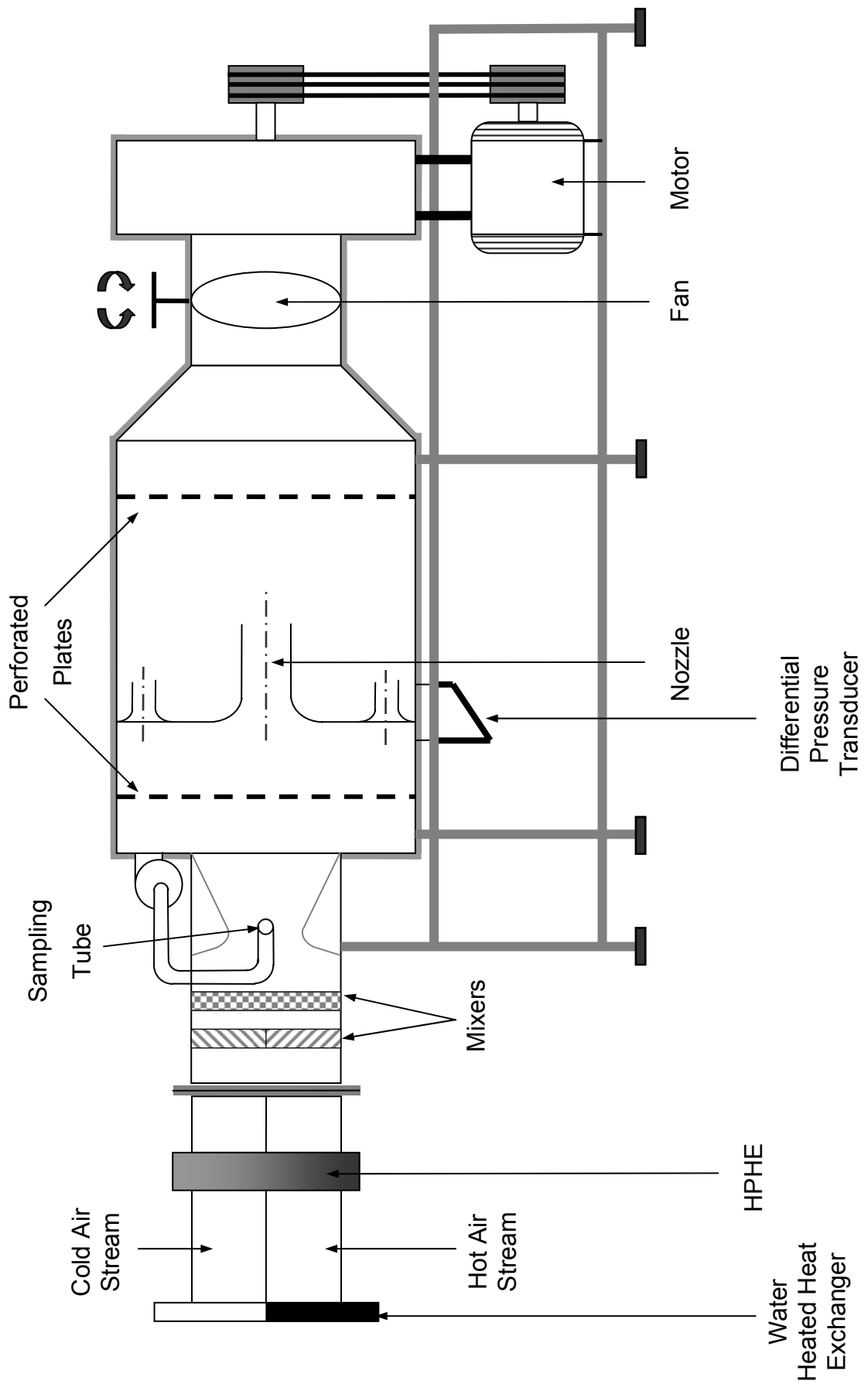


**Figure 5.12b** The HPHE wind tunnel set-up (side view)

### 5.2.3 HPHE experiments undertaken

For the HPHE experiments, four different fan speeds were used to obtain different mass flow rates through the tunnel. These include 35, 25, 15 and 10 Hz, as adjusted by the variable speed drive. Once the pressure drop across the nozzle is measured, the mass flow rate of the air through the tunnel can be calculated from

$$V_2^2 = \frac{2\Delta P}{\rho} + V_1^2 \times \frac{A_2}{A_1} \quad (5.7)$$

Where  $V_2$  is the velocity of the air flowing through the wind tunnel nozzle which has a diameter of 0.25 m and  $A_1$  is the area of the tunnel before the nozzle, with dimensions of 1.43 x 1.28 m. Equation 5.7 can be used as an accuracy check for the mass flow rates, where the sum of the respective tunnel section mass flows should equal the mass flow that is obtained through the nozzle section of the wind tunnel. The water flowing through the water heated heat exchanger is heated up in 10 °C increments such that the air before the evaporator section is heated at approximately the same ratio. An experimental run would typically consist of the following procedures:

1. Setting the hot water flow through the water heated heat exchanger and allowing it to stabilize at a given temperature
2. Setting the variable speed drive of the fan at 35 Hz
3. Measuring the temperatures at the inlet-and-outlet sections of the cold and hot air streams
4. Measuring the pressure drop across the HPHE
5. Measuring the pressure drop across the nozzle of the tunnel and the respective temperature at the nozzle
6. Adjusting the variable speed drive to a lower frequency and repeating steps three through five.

A test run is then complete and the temperature of the hot water increased and allowed to stabilize at the new incremental temperature. The above procedures are then repeated for different inlet hot temperatures.



In the testing of the HPHE, heat losses to the environment were taken into consideration. These losses are divided into four sections, namely

- Losses from the upper and lower copper headers
- Losses from the upper and lower galvanized steel casing

These losses were calculated using standard convection theory at an ambient temperature of 20 °C and are represented in Figure 5.13. Appendix B gives the sample calculations

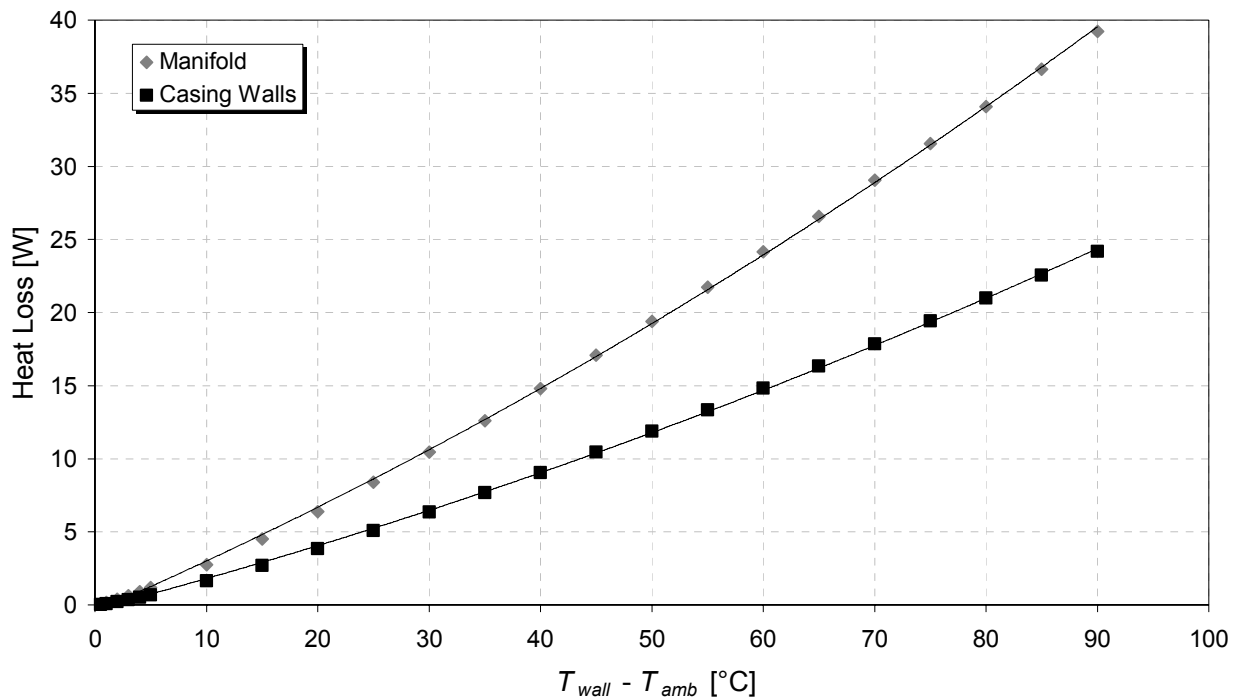


**Figure 5.13** Theoretical heat losses for the HPHE

As the dimensions for the upper and lower copper headers are the same, equation 5.9 applies to both and it should be noted that the header equation includes all 3 headers of the HPHE. The evaporator and condenser casing wall dimensions are also the same and therefore equation 5.9 represents both situations.

$$Q_{loss\_header} = 1.267 \times 10^{-3} (T_{wall} - T_{amb})^2 + 0.33(T_{wall} - T_{amb}) - 0.4226 \quad (5.8)$$

$$Q_{loss\_casing} = 8.16 \times 10^{-4} (T_{wall} - T_{amb})^2 + 0.2(T_{wall} - T_{amb}) - 0.2793 \quad (5.9)$$

## **5.3 Economic Analysis Experiments on a Demonstration HPHE**

### **5.3.1 CFW/Yucon HPHE description**

The demonstration HPHE specified in Section 4 is used in the economic analysis experiments. CFW decided that the HPHE could be tested on one of their 'mini' drier units with the following specifications:

- Unit wet capacity: between 50kg and 250kg depending on the product density
- Dimensions: 2.8 x 1.4 x 1.9 m
- Power requirements: 32A/ 3 phase/ 380 V supply

The drier unit is ideal for small scale drying of fruits, vegetables, herbs, meat and other products and is ideal for the purposes of this investigation. The HPHE was locally manufactured (Yucon, 2003) and consists of an array of 5/8" copper pipes manifolded to represent the thermosyphons. Aluminium fins were used and the casing manufactured from galvanized steel.

The aim of the experiments was primarily to determine the running costs of the mini drier when the HPHE was installed into the unit and therefore the energy savings. Correlation with the mathematical model can also be undertaken to ascertain whether or not the HPHE was in fact functioning as predicted. The HPHE was charged with R134a at a liquid fill charge ratio of 50 % based on the evaporator length.

### **5.3.2 CFW/Yucon HPHE experimental set-up**

For the drier unit, the only adjustment made by CFW was that a variable speed extractor fan was installed on the drier unit such that the mass flow rate could be adjusted. Aluminium foil ducting was used to connect the various air streams to the drier unit. Ducting was therefore needed from the extractor fan to the evaporator section of the HPHE and from the condenser section of the HPHE back into the inlet vent of the drier. For the connectivity, reducers were needed from the HPHE to the respective 0.25 m aluminium ducts. These reducers were manufactured by CFW and fitted to the HPHE. Figure 5.14a and 5.14b are photos of the HPHE set-up.

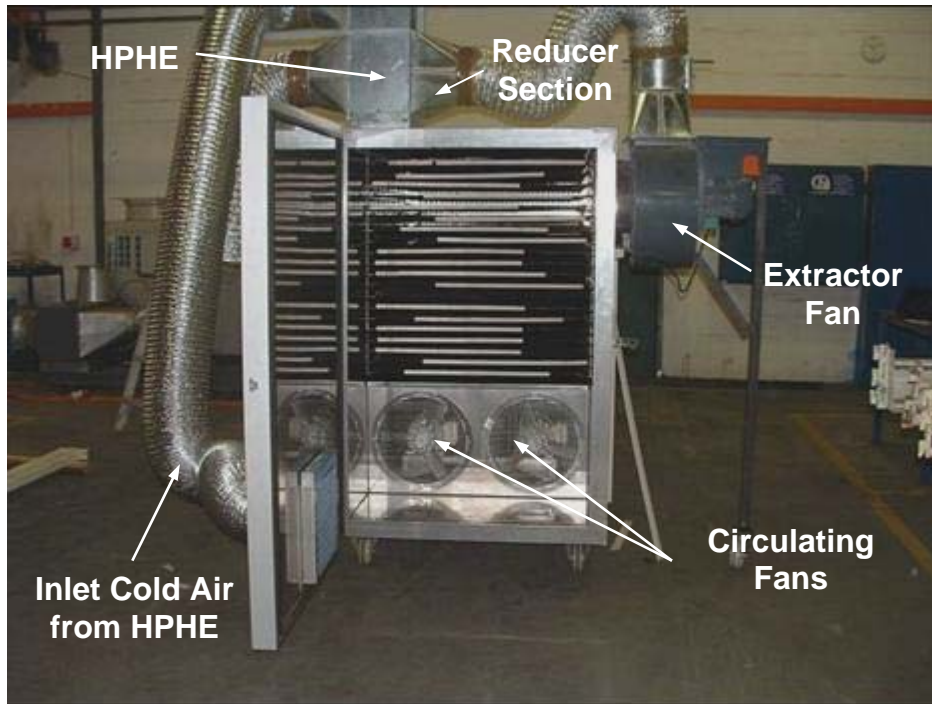


**Figure 5.14a** The HPHE installed onto the drier unit

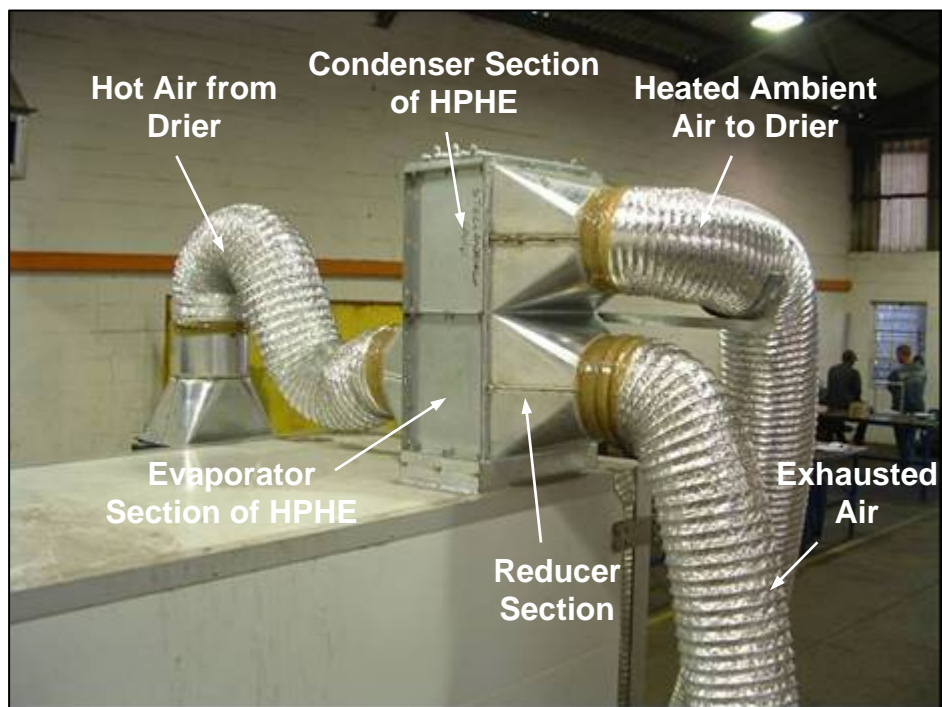


**Figure 5.14b** The reducer sections from the HPHE to the ducting

### 5.3.3 CFW/Yucon HPHE experiments undertaken

*Measuring air mass flow rates:* An anemometer was used to determine the velocities of the cold and hot air streams flowing through the ducting. The temperatures of the air streams were measured and hence the mass flow rates could be calculated from equation 5.6. To measure these velocities, a range of velocity readings were measured in the ducts which were then linearly averaged.

*HPHE testing:* A kWh meter was connected to the control system of the drier and reads the kWh's that the drier uses including the kWh's of the extractor fan. Two experiments were undertaken on the drier unit. The first was undertaken with the HPHE installed onto the drier unit. For this test, the extractor fan operated continuously. The drier control system was set such that the inside drier temperature be maintained at 50 °C. The relative humidity at start-up was 84 % and the temperature was 15 °C. The humidity ratio was obtained by wetting towels and placing them inside the drier unit. The test was run for 4 hours and the kWh reading calculated over this time period.

The next experiment was undertaken without the HPHE installed onto the unit. For this test, the extractor fan is set to only operate when the temperature of the drier reaches the specified drier temperature. The temperature of the drier was again set to 50 °C and the relative humidity at start-up was also 84 %. The start-up temperature was again 15 °C. The kWh meter readings were calculated and compared to the values with the HPHE installed.

The CFW/Yucon HPHE was then tested over a 5 hour period. Again, the drier unit was tested with and without the HPHE installed. The difference this time being that the kWh readings were calculated every hour. The reason for this was to investigate any start-up complications in the kWh readings obtained. Also, for these tests, the control system was set such that the extractor fan would operate continuously for both cases (not ideal operating conditions). The reason for this is that the HPHE's feasibility could be compared directly to the drier operating without the HPHE. The temperature of the drier was set to 50 °C in both cases. For the test with the HPHE, the relative humidity was measured as 81 % and without the HPHE as 76 %. The start-up temperatures were 20 °C and 18 °C, respectively.

The losses to the surroundings for the demonstration HPHE were calculated using standard convection theory analogous to that in Section 5.2.3 at an ambient temperature of 20 °C and are represented in Figure 5.15.

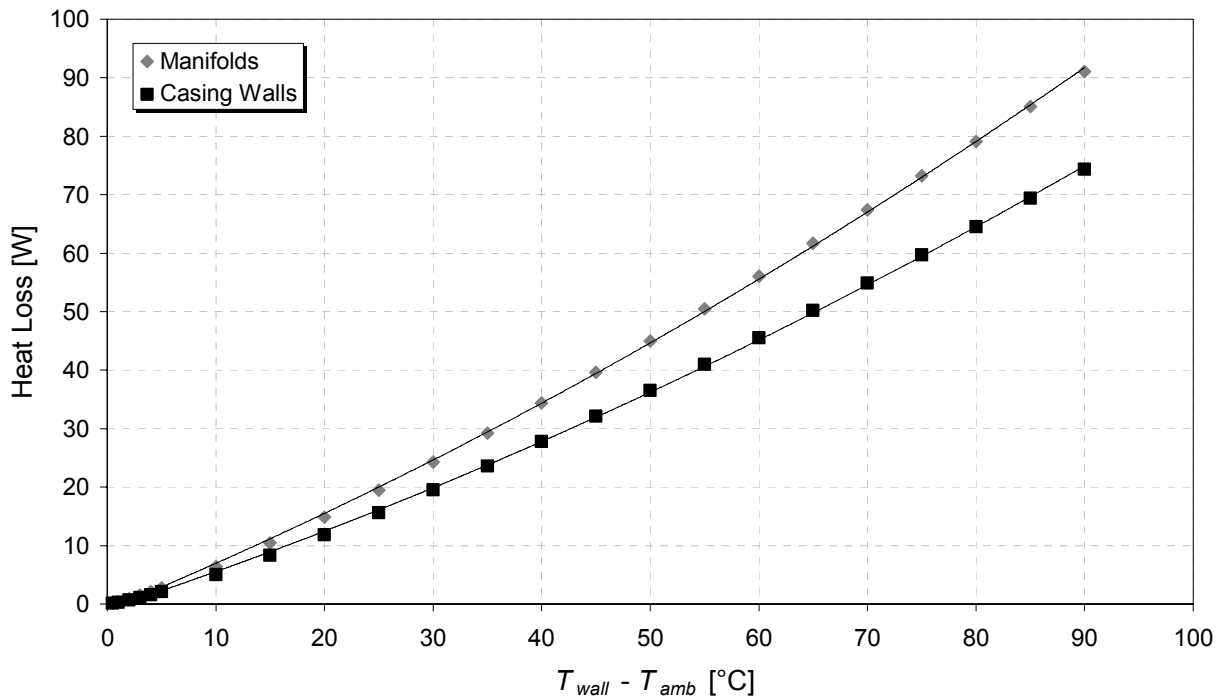


**Figure 5.15** Theoretical heat losses for the demonstration HPHE

Only the upper headers are exposed to the surrounding ambient air (the lower headers are sealed off). Equation 5.10 represents the heat losses from the six upper copper manifolds. The evaporator and condenser casing wall dimensions are the same and therefore equation 5.11 represents both situations.

$$\dot{Q}_{loss\_header} = 2.94 \times 10^{-3} (T_{wall} - T_{amb})^2 + 0.7658 (T_{wall} - T_{amb}) - 0.981 \quad (5.10)$$

$$\dot{Q}_{loss\_casing} = 2.515 \times 10^{-3} (T_{wall} - T_{amb})^2 + 0.6159 (T_{wall} - T_{amb}) - 0.862 \quad (5.11)$$

## 5.4 Equipment, Instrumentation and Calibrations

### 5.4.1 Equipment and instrumentation used

#### a) Thermocouples

All the thermocouples used in the experimental work are type-T thermocouples

#### b) Pressure Transducers

Two pressure transducers were used to measure the pressure drop across the HPHE in the wind tunnel test and also the pressure drop across the nozzle of the wind tunnel. Their serial numbers are 6FQ0141 and 6FQ0142

#### c) Measuring Scale

The scale used was a *UWE* NBS-Series 30 Bench scale capable of measuring up to 30 kg with a sensitivity of 0.005 kg

#### d) Vacuum Pump

The single stage vacuum pump used was a *Fast Vac* pump manufactured by J/B Industries, Inc. The serial number is 260227

#### e) Charging Fluid

Two fluids were used in the experimental work on the thermosyphons and the HPHE's which include

- *DuPont* SUVA 134a Refrigerant, Cas. no 811-97-2
- *Clipper* Lighter Fluid, 300 ml bottle manufactured by *Flamagas*.

#### f) Charge Measuring Device

The charge measuring device was constructed from standard charging refrigeration equipment as explained in section 5.1.2

#### g) Wind Tunnel Fan

A *Donkin Manufacturing Co. (Pty.) Ltd.* fan was used to draw the air through the wind tunnel. The serial number is C1194

h) Variable Speed Drive

A *Yaskawa Varispeed E7* variable speed drive was used to vary the wind tunnel fan. The model number is E7C4022

i) Hot Water Supply Tank

A *Hall Thermotank* boiler was used to heat the water in the 1800 L hot water supply tank. The serial number is 1000022

j) Anemometer

An *Airflow TA5* anemometer was used to measure the velocity of the cold and hot air streams in the laboratory and demonstration HPHE experiments. The serial number is 072148

k) Data Logging Units

Two different data logging systems were used. These data logging units are used to convert the mV readings from the thermocouples into temperatures. For the thermosyphon testing and laboratory HPHE testing, Schlumberger data loggers were used to log the temperatures. For the demonstration HPHE, a Hewlett Packard data logger was used along with a Laptop computer.

- *Schlumberger* SI 35951A IMP, 3 Pole Solid State Voltage, Current, Thermocouple
- HP Data Acquisition/Switch Unit. The serial number is US37008090

## 5.4.2 Calibrations

The charge measuring device described in Section 5.1.2 was calibrated such that the volume of fluid the device could hold could be determined and also what volumes the markings on the meter represented. Figure 5.16 illustrates the calibration curve.

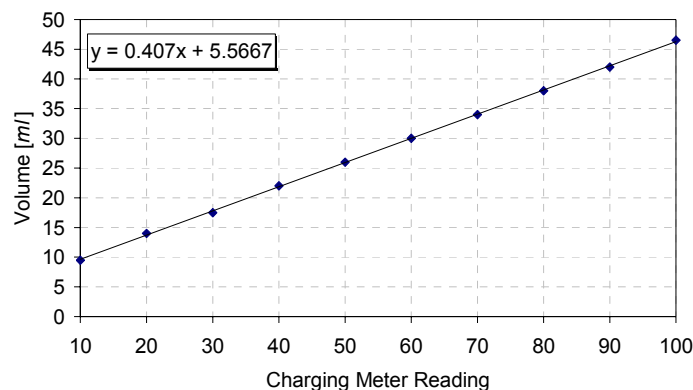


**Figure 5.16** Calibration curve for the charge measuring device

## 6 RESULTS

This section discusses the experimental results of the laboratory and industrial application experiments. Where necessary, these experimental results are compared with theoretical results such that their feasibility and accuracy are evaluated. The results are categorised into five sub-sections:

- General experimental results
- Multi-linear regression for the determination of the thermal characteristics of the charging fluids
- Performance correlating equations for thermosyphons
- The temperature distribution inside a HPHE
- Experimental verification of the CFW/Yucon HPHE

### 6.1 General Experimental Results

This section discusses the data readings obtained from the experimental work and is grouped as laboratory and demonstration experiments. The laboratory experiments consist of the thermosyphon experiments and the temperature distribution experiments inside the manifolded rows of a HPHE. The demonstration experiments consist of the economic analysis experiments undertaken on the CFW/Yucon HPHE in an industrial application.

#### 6.1.1 Thermosyphon laboratory experiments

For these experiments, the objective was to determine the inside heat transfer coefficients for the evaporator and condenser sections of various thermosyphons with different working fluids. These heat transfer coefficients can then be used in modelling HPHEs and in determining the heat transfer rate that the thermosyphons might deliver with a specified working fluid. Figure 6.1 illustrates the data for a vertically orientated thermosyphon charged with R134a from which the heat transfer rates can be calculated. The experimental readings for the thermosyphon experiments for vertical and the inclination angle of 45° are similar.



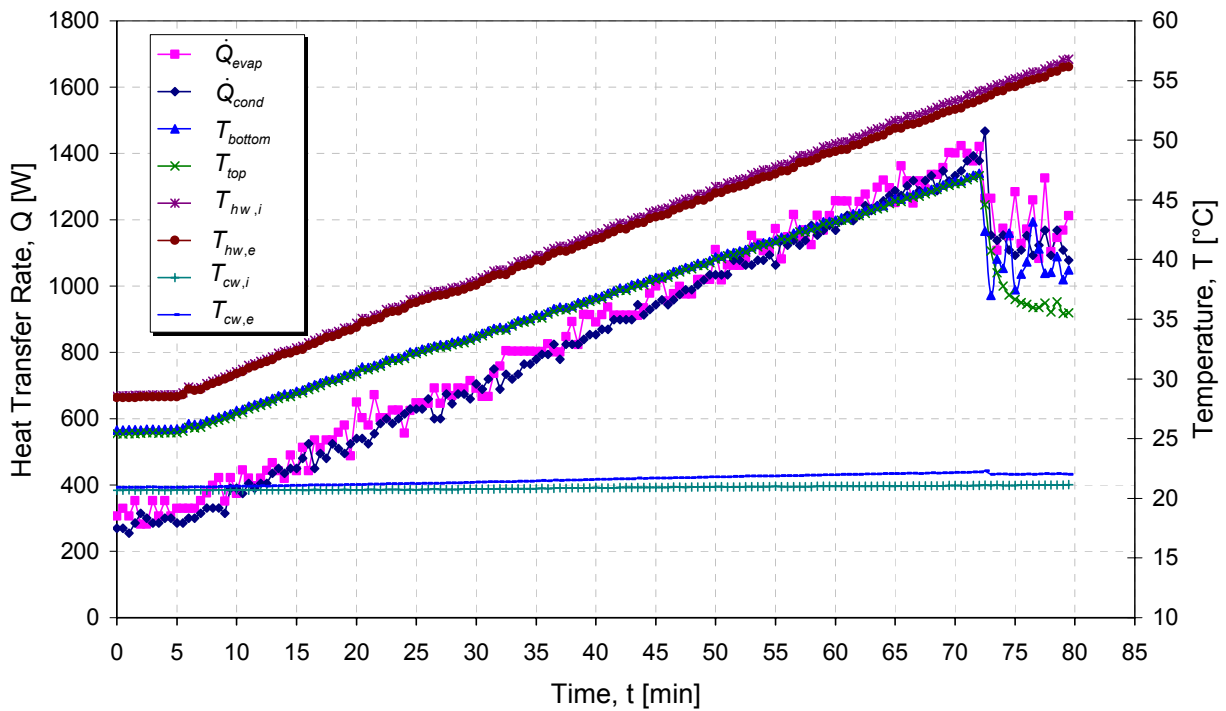


**Figure 6.1** Typical measured temperatures and heat transfer rates for the 3/4"-Thermosyphon

The important measurements used in determining the heat transfer rates for the thermosyphon are also illustrated in Figure 6.1. The inlet and outlet temperatures of the hot and cold water streams are plotted along with the inside top and bottom temperatures of the thermosyphon. From the temperature differences that arise and the known mass flows of the hot and cold water streams, the heat transfer rates of the evaporator and condenser sections are calculated using equation 5.1.

An indication that the thermosyphon is operating properly is that the top and bottom inside temperatures are the same or when the temperature difference between them is minimal. However, should this not be the case, the thermosyphon might still be functioning, but not at its optimum heat transfer rate for the corresponding inside temperatures. Also, of importance is the trend of the top and bottom temperatures at around 72 minutes in Figure 6.1. The maximum heat transfer rate of the thermosyphon is reached for both the evaporator and condenser sections and transfer of heat remains constant even if the heating temperature difference increases or the cold temperature difference decreases.

By the conservation of energy, the evaporator and condenser heat transfer rates should be the same. Figure 6.1 illustrates that  $\dot{Q}_{evap} \approx \dot{Q}_{cond}$ . Losses to the environment are present

and hence the condenser heat transfer rate is slightly lower. These losses are adjusted for when determining the inside heat transfer coefficients.

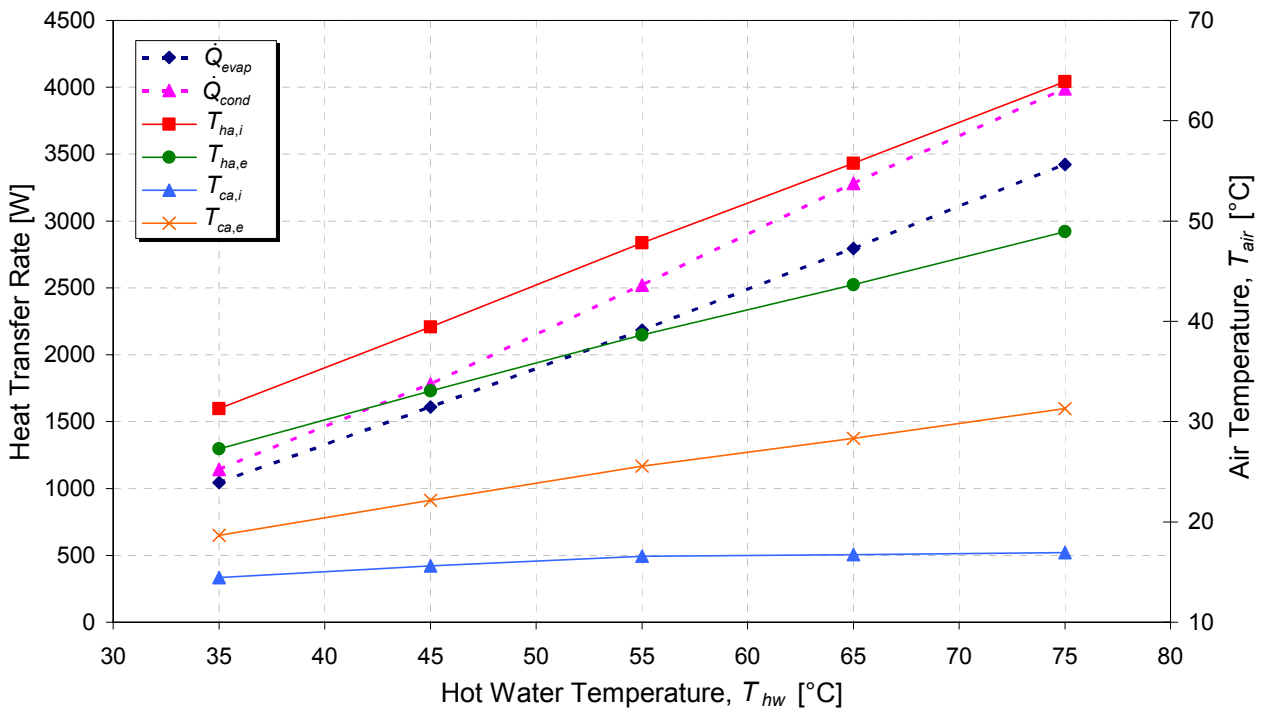


**Figure 6.2** Measured temperatures and heat transfer rates for the laboratory tested HPHE

Figure 6.2 illustrates the heat transfer rates as a function of hot water temperature for the HPHE described in Section 5.2. The objective of these experiments was to investigate the differences in the inside top and bottom temperatures of the manifolded rows of the HPHE. These inside temperatures are important as they indicate that the liquid has evaporated and thus the vapour is able to release its latent heat of vaporisation. The inlet and outlet air temperatures of the hot and cold air streams are also plotted against the respective hot water temperatures that entered the water heated heat exchanger (Section 5.2.2 describes the set-up).

### 6.1.2 Demonstration experiments on the CFW/Yucon HPHE

The demonstration experiments were undertaken on the CFW/Yucon HPHE specified in Section 4. The HPHE was installed at the CFW factory on an air drier unit. The objective of these experiments was to ascertain the feasibility of such a HPHE in industry and hence demonstrate the energy and economic savings that arise when using such a device. Figure 6.3 illustrates typical readings for the drier circulation air mass flow rate of roughly 0.5 kg/s.

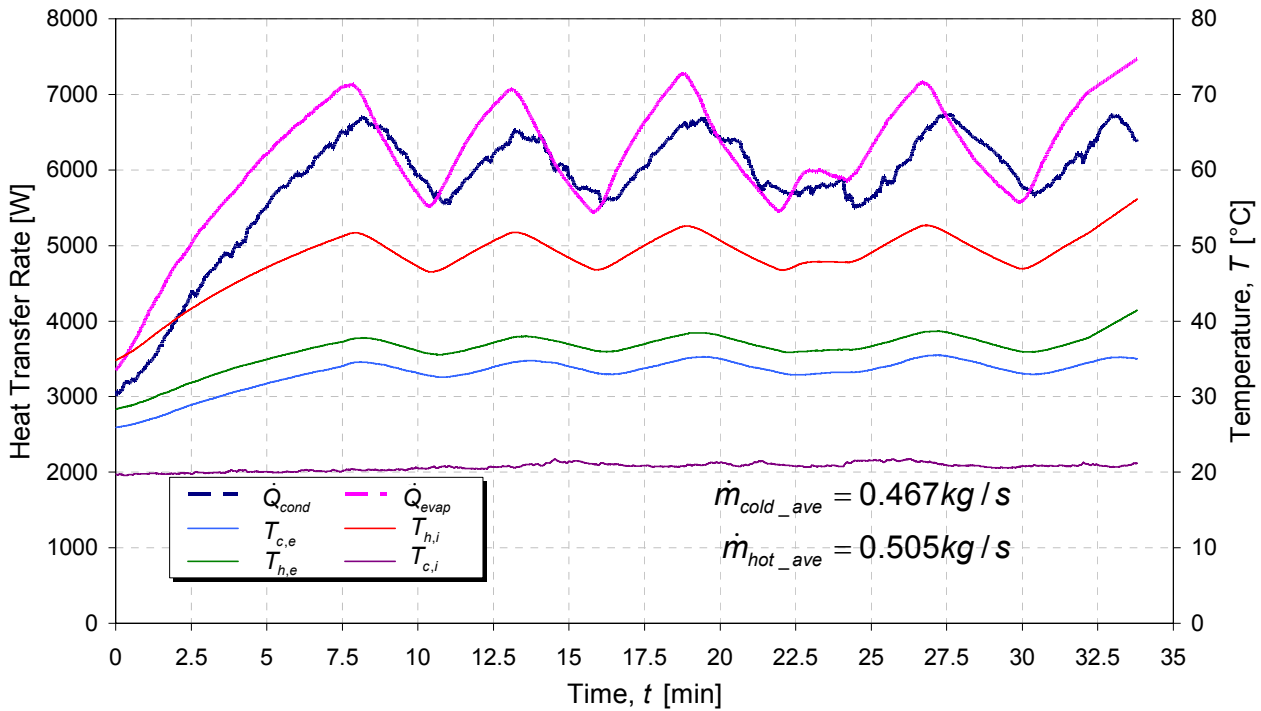


**Figure 6.3** Readings for the industrial testing of the CFW/Yucon HPHE

It is important to note the increase in the outlet cold air stream temperature,  $T_{c,e}$  and the decrease in the outlet hot air stream temperature,  $T_{h,e}$ . During these experiments, the ‘peaks’ and ‘valleys’ occurring every 2.5 minutes are as a result of the thermostat inside the drier unit. These ‘peaks’ and ‘valleys’ occurred in all the experiments undertaken on the drier unit and can be assumed to be negligible as the HPHE adjusts its heat transfer rate for changes in temperature.

The heat transfer rates are calculated from the temperature difference between the inlets and outlets of the hot and cold air streams and the measured mass flow rates using equation 5.1. For a given data point, a heat input (the heat transfer rate in the evaporator section of the HPHE) of  $\dot{Q}_{evap} = \dot{Q}_{in} = 0.503 \times 1007.77 \times (52.25 - 38.44) = 7005.5 \text{ W}$  is obtained. The fresh air is pre-heated by the recovered heat of the CFW/Yucon HPHE. This exiting air from the condenser section will then be passed back into the drier unit. a heat recovery of  $\dot{Q}_{cond} = \dot{Q}_{recovered} = 0.462 \times 1006.9 \times (35.22 - 21) = 6614.97 \text{ W}$  is obtained for the same data point.

## 6.2 Multi-Variable linear Regression Techniques for the Heat Transfer Coefficients

A large number of data points were generated for each thermosyphon experiment. These were then reduced as data sets for each thermosyphon at vertical and inclined operation and for the different working fluids such that a data set consisted of 45 data points. It is important that the energy balances between the evaporator and condenser sections of the thermosyphons lie within a small percentage of each other as this is an indication that the thermocouples are in fact measuring the correct temperatures and that the conservation of energy law is being satisfied.

This section describes the predicted results that are obtained when multi-linear regression techniques are used on the generated data sets and is further divided into the predicted results that are obtained for the operation with R134a and Butane as the working fluids. The heat fluxes and inside top-and-bottom temperatures of the thermosyphon are expected to influence the heat transfer coefficients most significantly. These variables are therefore included in the equations that are obtained from the regression techniques. Sample calculations from which the experimental inside heat transfer coefficients are calculated are given in Appendix B.

### 6.2.1 5/8"-Thermosyphon Results: R134a

Figure 6.4a and 6.4b illustrate the energy balances obtained for the thermosyphon charged with a 50 % liquid fill charge ratio based on the evaporator length. For the vertical operation, it was clear that the condenser section yielded values 40 % lower than for the evaporator and that the inclined operation yielded condenser heat transfer rates of 60 % lower than those for the evaporator heat transfer rates. The conservation of energy was clearly not satisfied and hence these experiments were deemed unsatisfactory. A possible reason for these unsatisfactory energy balances might be erroneous thermocouple measurements. Different thermocouples were used and the experiments repeated numerous times. The results however, appeared to be similar. The mass flow measurements were also repeated numerous times and proved to yield the same results.

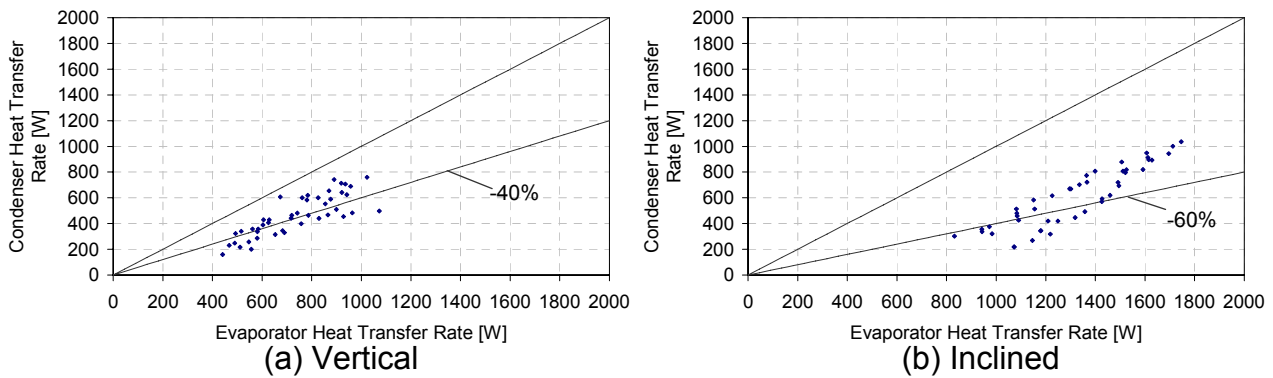


**Figure 6.4** Energy balances for the 5/8"-Thermosyphon operating with R134a charged at 50 % liquid fill charge ratio

After attempting to rectify the conservation of energy problem with little success, it was felt that the liquid fill charge ratio might influence the energy balances. With a charge of 50 %, too large an amount of fluid might be in the thermosyphon and hence the fluid does not boil over the whole region as would be desired. The fluid could also be blasted up to the condenser section were it just 'sits' and the vapour-liquid cycle is prevented from continuing. However, this could not be proven as the inside top and bottom temperature fell within reasonable bands of each. There were also no indications of flooding from the readings.

The liquid fill charge ratio was then decreased to 25 %. Figure 6.5a and 6.5b represent the energy balances for the condenser and evaporator sections for vertical and inclined operation, respectively. The results may be more reliable as the energy balances are decreased from 40 to 30 % and from 60 to 10 % for the vertical and inclined experiments, respectively. For these experiments, the heat fluxes ranged from 7000 - 25000 W/m<sup>2</sup>. The maximum heat transfer rate for the vertical operation yielded a value of 1160.46 W at a temperature difference ( $\Delta T = \bar{T}_h - \bar{T}_c$ ) of 23 °C whilst the inclined operation yielded a heat transfer rate of 936.67 W at the same  $\Delta T$ . The maximum heat transfer rate for the inclined operation was 1274.16 W at a  $\Delta T = 29.17$  °C.

Figure 6.5c and 6.5d illustrate the comparison between the experimentally and predicted inside evaporator heat transfer coefficients for vertical and inclined operation, respectively. Figure 6.5c shows that 97.7 % of the predicted values fell well within 10 % of the experimentally determined values, whilst Figure 6.5d shows that all the predicted values fell within 7.5 % of the experimental values.

Figure 6.5e and 6.5f illustrate the comparison between the experimentally and predicted inside condenser heat transfer coefficients for vertical and inclined operation, respectively. At minimum, 95.5 % of the predicted values fell within 5 % of the experimental values for both the vertical and inclined operation. It is also noticed that the condenser heat transfer coefficients remain relatively constant throughout the thermosyphon operation.

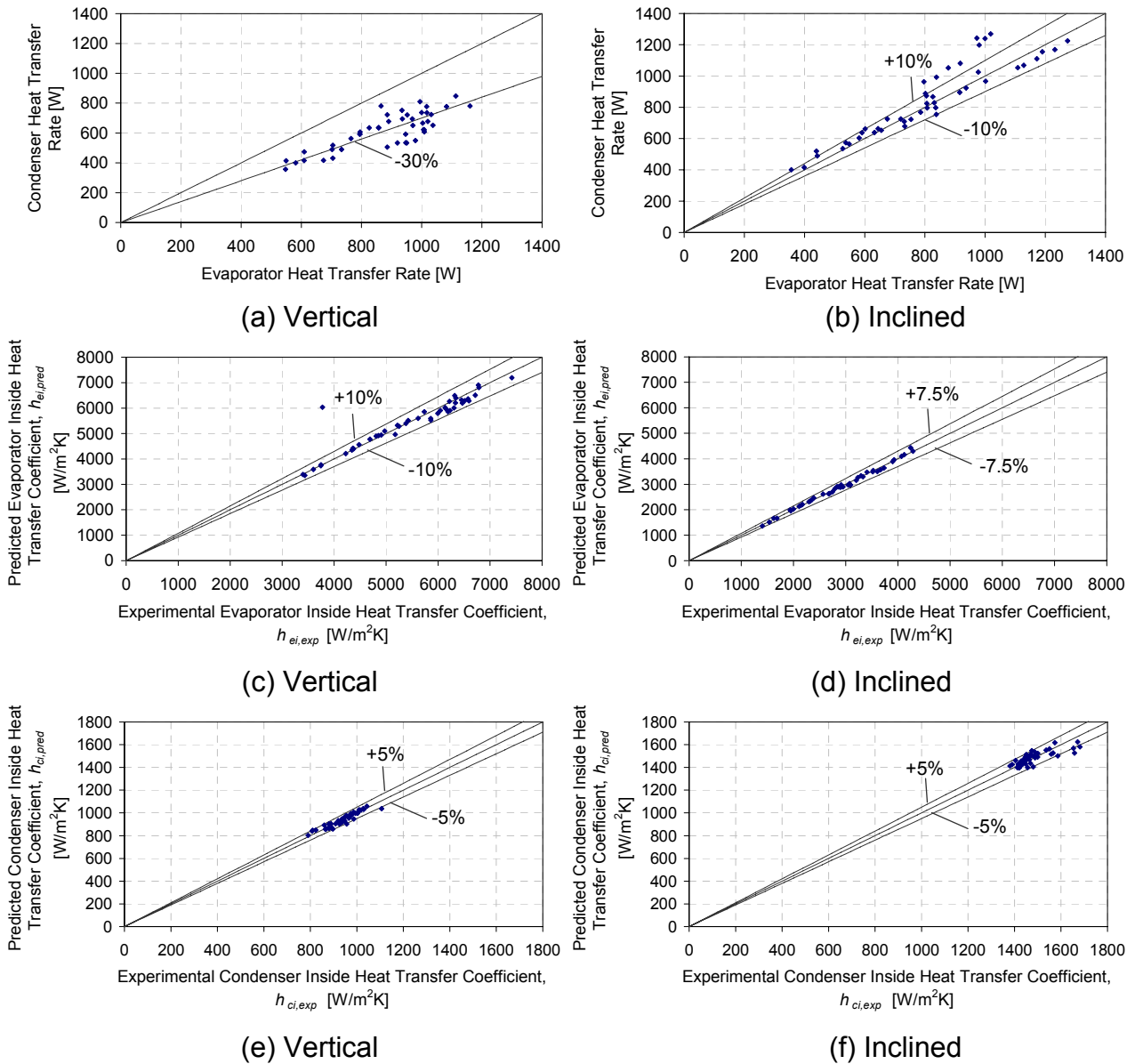


**Figure 6.5** Energy balances and inside evaporator and condenser heat transfer coefficients for the 5/8"-Thermosyphon operating with R134a charged at 25 % and operating vertically and at 45°

The following correlations for the evaporator and condenser inside heat transfer coefficients were obtained for the vertical and inclined operations

$$\phi = 90^\circ \quad h_{ei} = 0.083\dot{q}^{1.25}T_i^{-0.36} \quad [R^2=0.869] \quad (6.1)$$

$$\phi = 45^\circ \quad h_{ei} = 0.479\dot{q}^{0.875}T_i^{0.073} \quad [R^2=0.995] \quad (6.2)$$

$$\phi = 90^\circ h_{ci} = 12.264\dot{q}^{0.706}T_i^{-0.725} \quad [R^2=0.890] \quad (6.3)$$

$$\phi = 45^\circ h_{ci} = 5788.83\dot{q}^{-0.147}T_i^{0.02} \quad [R^2=0.639] \quad (6.4)$$

## 6.2.2 3/4"-Thermosyphon Results: R134a

Figure 6.6a and 6.6b illustrate energy balances of 5 % and 10 % between the evaporator and condenser heat transfer rates for both the vertical and inclined operations, respectively. For these experiments, the heat fluxes ranged from 6000-41500 W/m<sup>2</sup> and the liquid fill charge ratio was 50 %. The maximum heat transfer rate for the vertical operation yielded a value of 1384.54 W at a  $\Delta T = 31$  °C whilst the inclined operation yielded 1765.94 W at the same  $\Delta T$ . The maximum heat transfer rate for the inclined operation was 2563.59 W at a  $\Delta T = 38.98$  °C.

Figure 6.6c and 6.6d illustrate the comparison between the experimentally and predicted inside evaporator heat transfer coefficients for the vertical and inclined operation, respectively. Figure 6.6c shows that 88.8 % of the predicted values fell within 7.5 % of the experimentally determined values, whilst Figure 6.6d shows that 91.1 % of the predicted values fell well within 5 % of the experimental values.

Figure 6.6e and 6.6f illustrate the comparison between the experimentally and predicted inside condenser heat transfer coefficients for vertical and inclined operation, respectively. For the vertical operation, 95.5 % of the predicted values fell within 5 % of the experimental values and for the inclined operation, 95.5 % fell within 7.5 %. It is also noticed that the condenser heat transfer coefficients remain relatively constant throughout the thermosyphon operation.

The following correlations for the evaporator and condenser inside heat transfer coefficients were obtained for the vertical and inclined operation

$$\phi = 90^\circ h_{ei} = 38.18\dot{q}^{0.216}T_i^{0.739} \quad [R^2=0.911] \quad (6.5)$$

$$\phi = 45^\circ h_{ei} = 15.78\dot{q}^{0.477}T_i^{0.152} \quad [R^2=0.954] \quad (6.6)$$

$$\phi = 90^\circ h_{ci} = 2243\dot{q}^{-0.09}T_i^{0.066} \quad [R^2=0.353] \quad (6.7)$$

$$\phi = 45^\circ h_{ei} = 6621.47\dot{q}^{-0.141}T_i^{0.003} \quad [R^2=0.557] \quad (6.8)$$

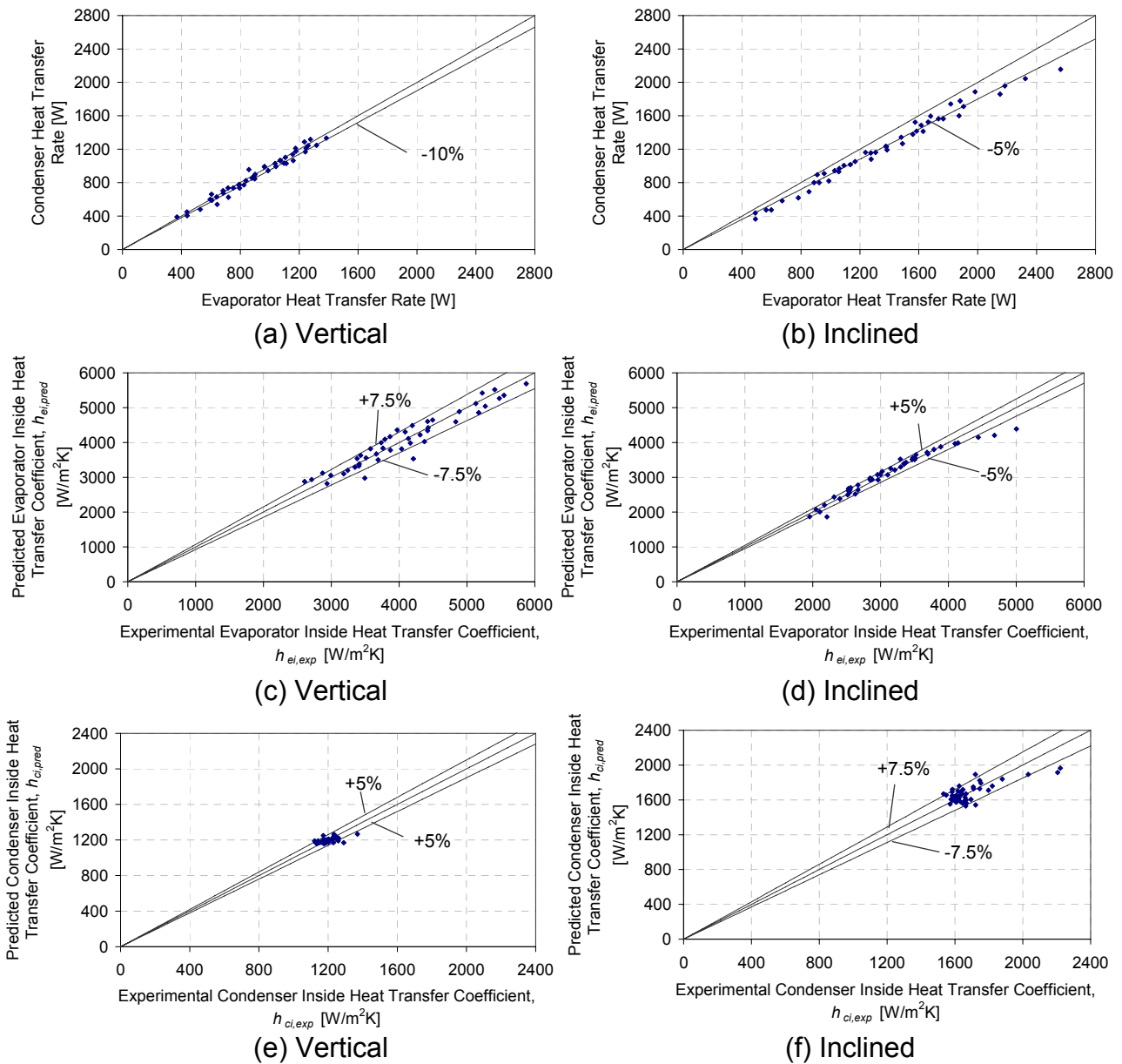


**Figure 6.6** Energy balances and inside evaporator and condenser heat transfer coefficients for the 3/4"-Thermosyphon operating with R134a charged at 50 % and operating vertically and at 45°

### 6.2.3 7/8"-Thermosyphon Results: R134a

Figure 6.7a and 6.7b illustrate energy balances of 15 % and 20 % between the evaporator and condenser heat transfer rates for both the vertical and inclined operations, respectively. For these experiments, the heat fluxes ranged from 4100-43500 W/m<sup>2</sup> and the liquid fill charge ratio was 50 %. The maximum heat transfer rate for the vertical operation yielded a value of 2068.82 W at a  $\Delta T = 32$  °C whilst the inclined operation



yielded a heat transfer rate of 1231.75 W at the same  $\Delta T$ . The maximum heat transfer rate for the inclined operation was 3129.65 W at a  $\Delta T= 44.14$  °C.

Figure 6.7c and 6.7d illustrate the comparison between the experimentally and predicted inside evaporator heat transfer coefficients for the vertical and inclined operation, respectively. For the vertical operation (Figure 6.7c), 97.7 % of the predicted values fell within 5 % of the experimentally determined values, whilst for the inclined operation (Figure 6.7d), 97.7 % of the predicted values fell to within 10 % of the experimental values.

Figure 6.7e and 6.7f illustrate the comparison between the experimentally and predicted inside condenser heat transfer coefficients for vertical and inclined operation, respectively. For the vertical operation, 97.7 % of the predicted values fell within 5 % of the experimental values and for the inclined operation, 95.5 % fell within 7.5 %. Again, it is noticed that the condenser heat transfer coefficients remain relatively constant throughout the thermosyphon operation.

The following correlations for the evaporator and condenser inside heat transfer coefficients were obtained for the vertical and inclined operation

$$\phi = 90^\circ \quad h_{ei} = 90.157\dot{q}^{0.179}T_i^{0.572} \quad [R^2=0.965] \quad (6.9)$$

$$\phi = 45^\circ \quad h_{ei} = 16.33\dot{q}^{0.281}T_i^{0.591} \quad [R^2=0.936] \quad (6.10)$$

$$\phi = 90^\circ \quad h_{ci} = 2129.59\dot{q}^{-0.066}T_i^{-0.007} \quad [R^2=0.293] \quad (6.11)$$

$$\phi = 45^\circ \quad h_{ci} = 2937.16\dot{q}^{-0.111}T_i^{0.098} \quad [R^2=0.340] \quad (6.12)$$

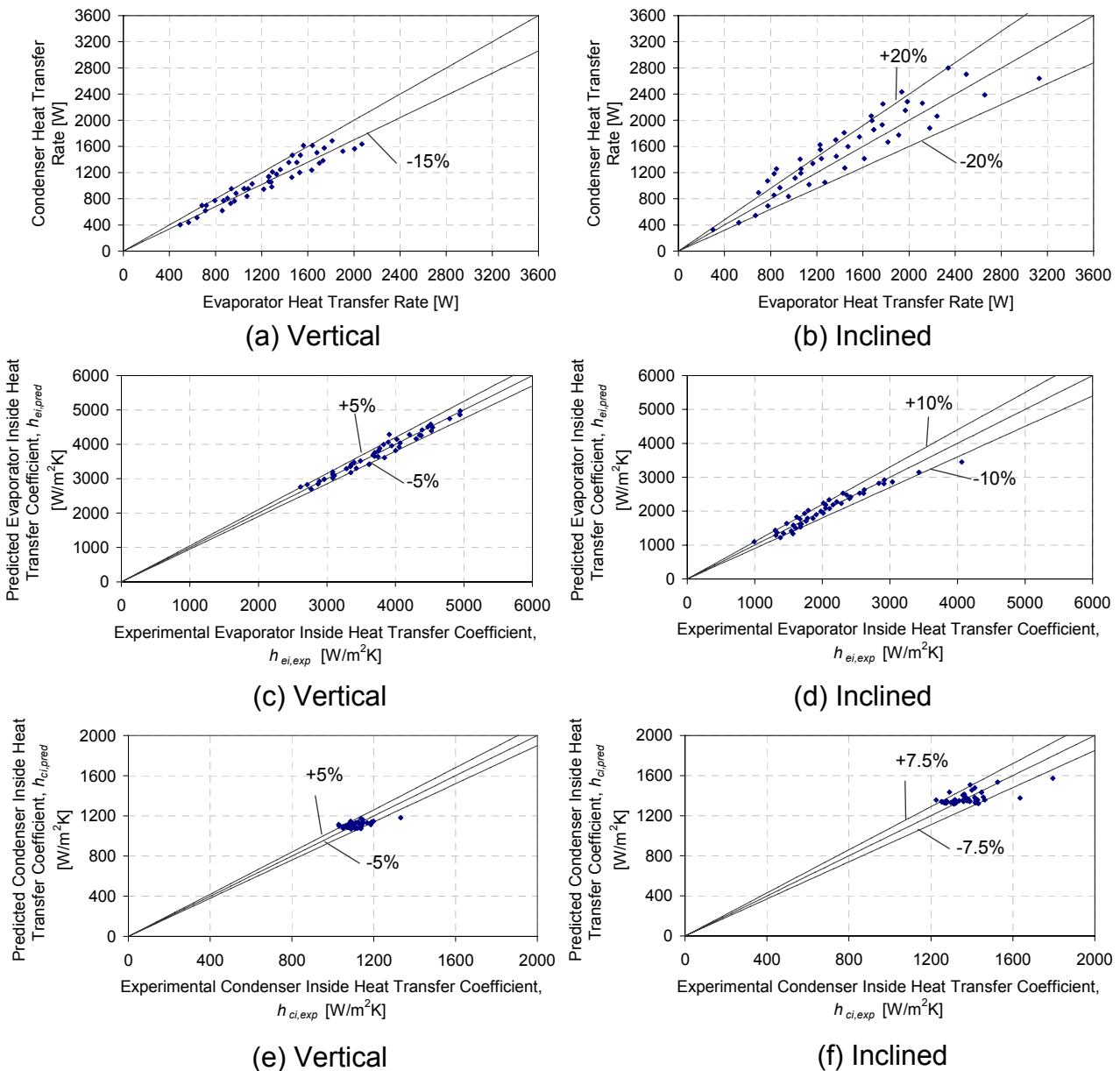


**Figure 6.7** Energy balances and inside evaporator and condenser heat transfer coefficients for the 7/8"-Thermosyphon operating with R134a charged at 50 % and operating vertically and at 45°

### 6.2.4 5/4"-Thermosyphon Results: R134a

Figure 6.8a and 6.78b illustrates energy balances of 10 % between the evaporator and condenser heat transfer rates for both the vertical and inclined operation. For these experiments, the heat fluxes ranged from 4100-43500 W/m<sup>2</sup> and the liquid fill charge ratio was 50 %. The maximum heat transfer rate for the vertical operation yielded a value of 4907.48 W at a  $\Delta T = 26$  °C whilst the inclined operation yielded a heat transfer rate of

2835.55 W at the same  $\Delta T$ . The maximum heat transfer rate for the inclined operation was 7763.95 W at a  $\Delta T = 51.27$  °C.

Figure 6.8c and 6.8d illustrate the comparison between the experimentally and predicted inside evaporator heat transfer coefficients for the vertical and inclined operation, respectively. For the vertical operation (Figure 6.8c), 97.7 % of the predicted values fell well within 7.5 % of the experimentally determined values, whilst for the inclined operation (Figure 6.8d), all of the predicted values fell within 7.5 % of the experimental values.

Figure 6.8e and 6.8f illustrate the comparison between the experimentally and predicted inside condenser heat transfer coefficients for vertical and inclined operation, respectively. For the vertical and inclined operations, all of the predicted values fell within 5 % of the experimental values. The condenser heat transfer rates are seen to remain relatively constant.

The following correlations for the evaporator and condenser inside heat transfer coefficients were obtained for the vertical and inclined operations

$$\phi = 90^\circ \quad h_{ei} = 12.85\dot{q}^{0.403}T_i^{0.718} \quad [R^2=0.973] \quad (6.13)$$

$$\phi = 45^\circ \quad h_{ei} = 3.35\dot{q}^{0.545}T_i^{0.217} \quad [R^2=0.992] \quad (6.14)$$

$$\phi = 90^\circ \quad h_{ci} = 241.4\dot{q}^{0.322}T_i^{-0.467} \quad [R^2=0.821] \quad (6.15)$$

$$\phi = 45^\circ \quad h_{ci} = 1412.42\dot{q}^{0.026}T_i^{0.07} \quad [R^2=0.481] \quad (6.16)$$

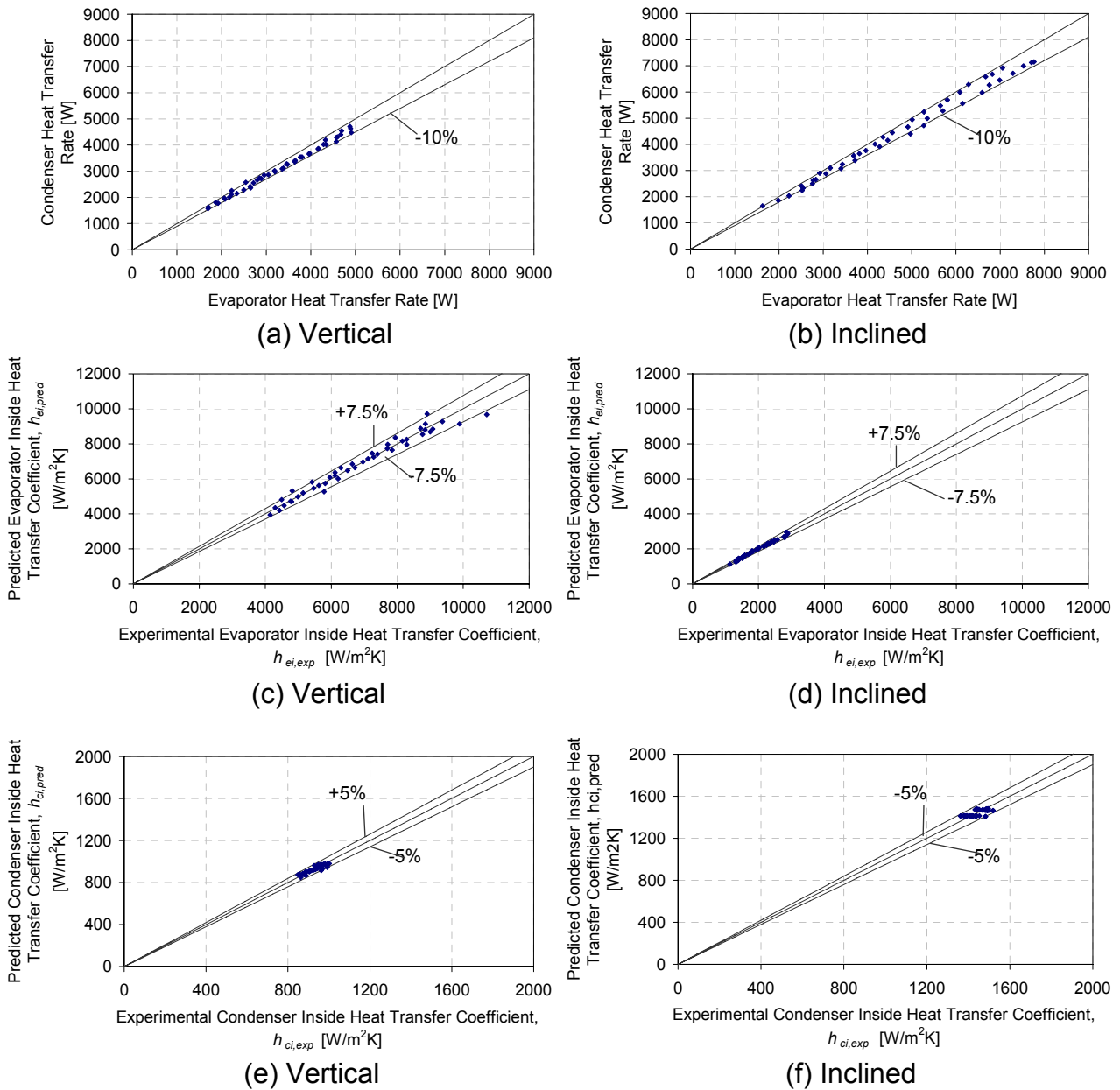


**Figure 6.8** Energy balances and inside evaporator and condenser heat transfer coefficients for the 5/4” -Thermosyphon operating with R134a charged at 50 % and operating vertically and at 45°.

### 6.2.5 5/8”-Thermosyphon Results: Butane

Figure 6.9a and 6.9b illustrate energy balances 35 % and 30 % between the evaporator and condenser heat transfer rates for the vertical and inclined operations, respectively. For these experiments, the heat fluxes ranged from 5700-25000 W/m<sup>2</sup> and the liquid fill charge ratio was 50 %. This charge ratio was not decreased (as with the R134a charged 5/8”-Thermosyphon). The maximum heat transfer rate for the vertical operation yielded a value of 730.08 W at a  $\Delta T = 22$  °C whilst the inclined operation yielded a heat transfer rate of

748.22 W at the same  $\Delta T$ . The maximum heat transfer rate for the inclined operation was 1243.66 W at a  $\Delta T= 30.29\text{ }^{\circ}\text{C}$ .

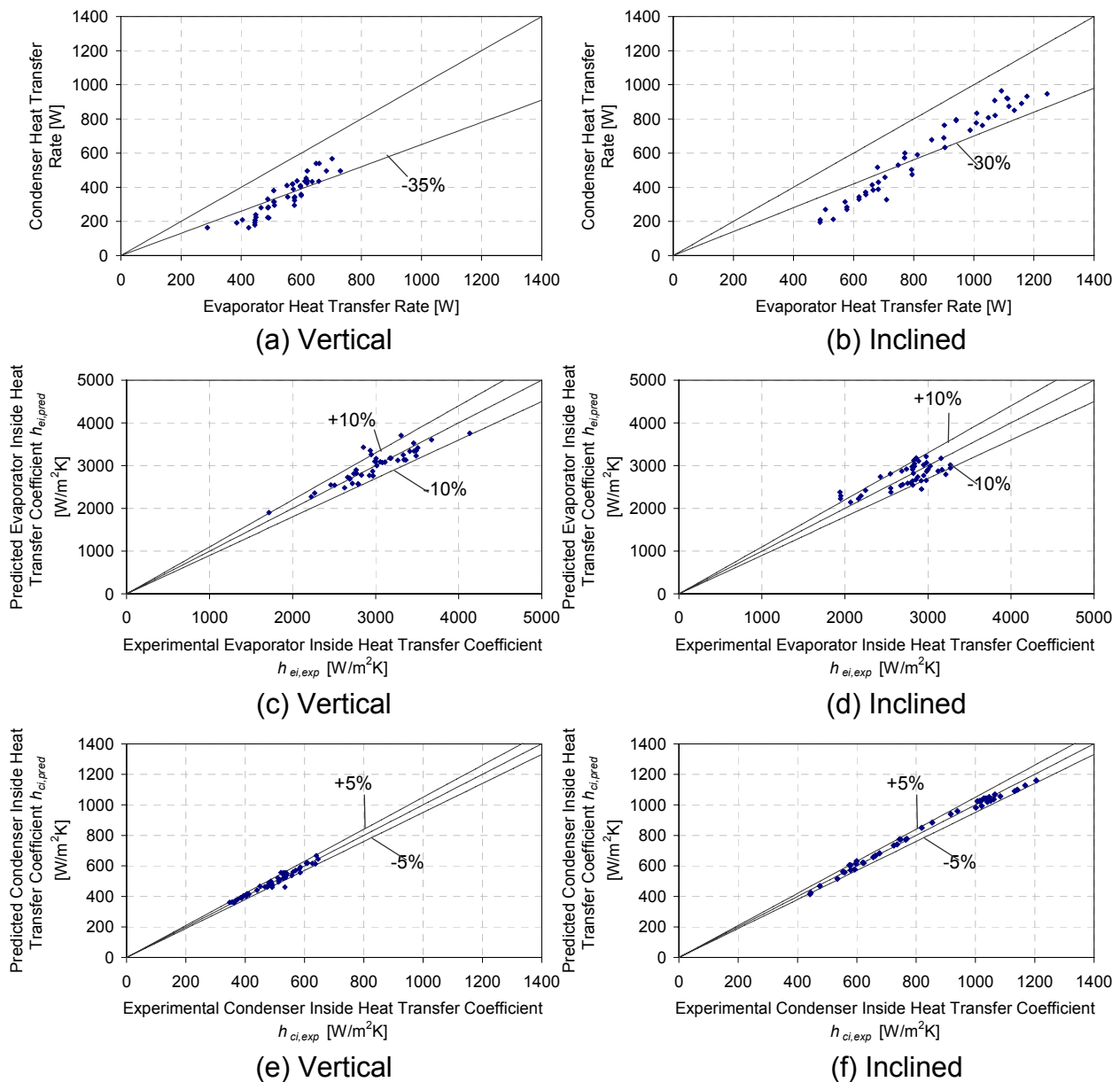


**Figure 6.9** Energy balances and inside evaporator and condenser heat transfer coefficients for the 5/8"-Thermosyphon operating with Butane charged at 50 % and operating vertically and at  $45^{\circ}$

Figure 6.9c and 6.9d illustrate the comparison between the experimentally and predicted inside evaporator heat transfer coefficients for the vertical and inclined operation, respectively. For the vertical operation (Figure 6.9c), 91.1 % of the predicted values fell within 10 % of the experimentally determined values, whilst for the inclined operation (Figure 6.9d), 86.6 % of the predicted values fell within 10 % of the experimental values.

Figures 6.9e and 6.9f illustrate the comparison between the experimentally and predicted inside condenser heat transfer coefficients for vertical and inclined operation. At minimum, 97.7 % of the predicted values fell well within 5 % of the experimental values for both the vertical and inclined operation.

The following correlations for the evaporator and condenser inside heat transfer coefficients were obtained for the vertical and inclined operation

$$\phi = 90^\circ h_{ei} = 2.725\dot{q}^{0.677}T_i^{0.205} \quad [R^2=0.842] \quad (6.17)$$

$$\phi = 45^\circ h_{ei} = 72.78\dot{q}^{-0.09}T_i^{1.285} \quad [R^2=0.608] \quad (6.18)$$

$$\phi = 90^\circ h_{ci} = 3.171\dot{q}^{0.372}T_i^{0.512} \quad [R^2=0.959] \quad (6.19)$$

$$\phi = 45^\circ h_{ci} = 51\dot{q}^{0.989}T_i^{-1.832} \quad [R^2=0.991] \quad (6.20)$$

## 6.2.6 3/4"-Thermosyphon Results: Butane

Figure 6.10a and 6.10b illustrate energy balances of 15 % and 10 % between the evaporator and condenser heat transfer rates for the vertical and inclined operations, respectively. For these experiments, the heat fluxes ranged from 4500 - 33000 W/m<sup>2</sup> and the liquid fill charge ratio was 50 %. The maximum heat transfer rate for the vertical operation yielded a value of 1417.16 W at a  $\Delta T = 32$  °C whilst the inclined operation yielded a heat transfer rate of 1518.79 W at the same  $\Delta T$ . The maximum heat transfer rate for the inclined operation was 2049.06 W at a  $\Delta T = 42.03$  °C.

Figure 6.10c and 6.10d illustrate the comparison between the experimentally and predicted inside evaporator heat transfer coefficients for the vertical and inclined operation. For the vertical operation (Figure 6.10c), 77.7 % of the predicted values fell within 7.5 % of the experimentally determined values, whilst for the inclined operation (Figure 6.10d), 95.5 % of the predicted values fell within 7.5 % of the experimental values.

Figure 6.10e and 6.10f illustrate the comparison between the experimentally and predicted inside condenser heat transfer coefficients for vertical and inclined operation. At minimum, 95.5 % of the predicted values fell well within 5 % of the experimental values for both the vertical and inclined operation.

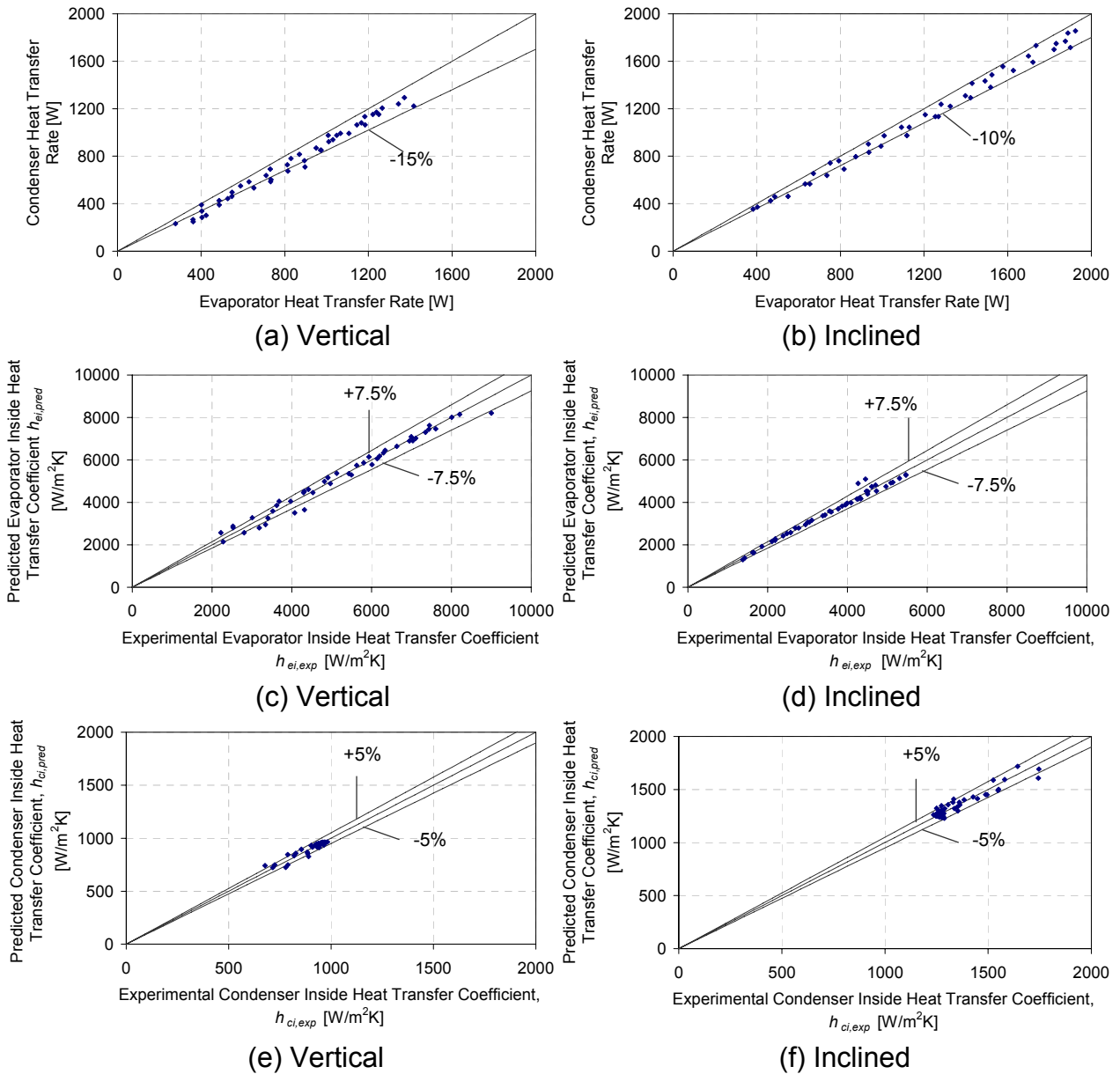


**Figure 6.10** Energy balances and inside evaporator and condenser heat transfer coefficients for the 3/4"-Thermosyphon operating with Butane charged at 50 % and operating vertically and at 45°

The following correlations for the evaporator and condenser inside heat transfer coefficients were obtained for the vertical and inclined operation

$$\phi = 90^\circ \quad h_{ei} = 1.68\dot{q}^{0.581}T_i^{0.682} \quad [R^2=0.968] \quad (6.21)$$

$$\phi = 45^\circ \quad h_{ei} = 0.608\dot{q}^{1.267}T_i^{-1.025} \quad [R^2=0.989] \quad (6.22)$$

$$\phi = 90^\circ \quad h_{ci} = 408.35\dot{q}^{0.593}T_i^{-1.30} \quad [R^2=0.880] \quad (6.23)$$

$$\phi = 45^\circ \quad h_{ci} = 11328.69\dot{q}^{-0.45}T_i^{0.605} \quad [R^2=0.893] \quad (6.24)$$

## 6.2.7 7/8"-Thermosyphon Results: Butane

Figure 6.11a and 6.11b illustrate energy balances of 15 % and 10 % between the evaporator and condenser heat transfer rates for the vertical and inclined operations, respectively. For these experiments, the heat fluxes ranged from 3400 - 35300 W/m<sup>2</sup> and the liquid fill charge ratio was 50 %. The maximum heat transfer rate for the vertical operation yielded a value of 1696.25 W at a  $\Delta T= 41\text{ }^{\circ}\text{C}$  whilst the inclined operation yielded a heat transfer rate of 1825.91 W at the same  $\Delta T$ . The maximum heat transfer rate for the inclined operation was 2538.42 W at a  $\Delta T= 51.6\text{ }^{\circ}\text{C}$ .

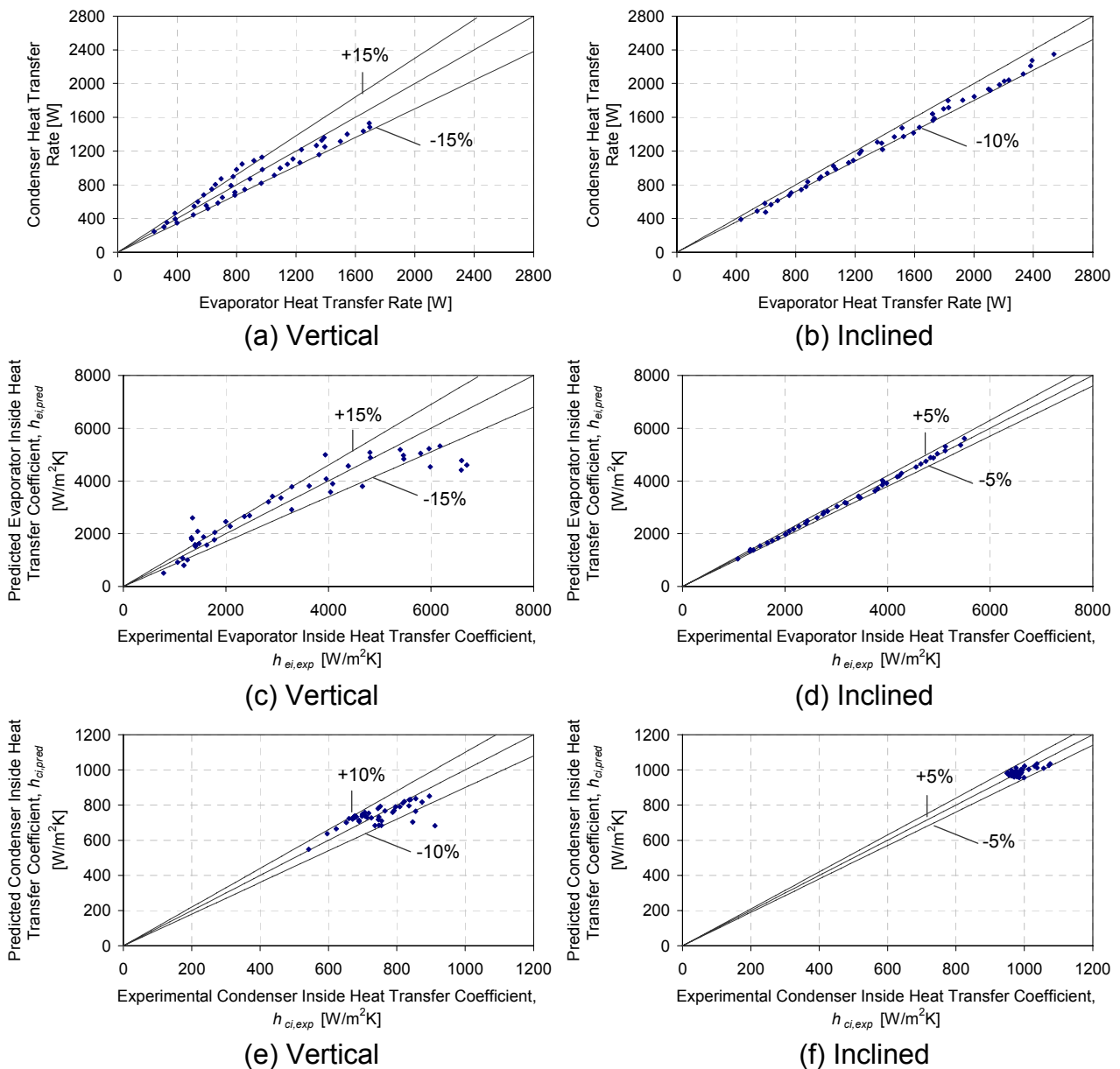


**Figure 6.11** Energy balances and inside evaporator and condenser heat transfer coefficients for the 7/8"-Thermosyphon operating with Butane charged at 50 % and operating vertically and at 45°



Figure 6.11c and 6.11d illustrate the comparison between the experimentally and predicted inside evaporator heat transfer coefficients for the vertical and inclined operation. For the vertical operation (Figure 6.11c), 66.7 % of the predicted values fell within 15 % of the experimentally determined values, whilst for the inclined operation (Figure 6.11d), all of the predicted values fell well within 5 % of the experimental values.

Figure 6.11e and 6.11f illustrate the comparison between the experimentally and predicted inside condenser heat transfer coefficients for vertical and inclined operation. For the vertical operation (Figure 6.11e), 93.3 % of the predicted values fell within 10 % of the experimental values and for the inclined operation (Figure 6.11f), all the values fell within 5 %. The condenser heat transfer coefficients are again seen to remain relatively constant

The following correlations for the evaporator and condenser inside heat transfer coefficients were obtained for the vertical and inclined operation

$$\phi = 90^\circ h_{ei} = 0.219\dot{q}^{2.42}T_i^{-3.513} \quad [R^2=0.879] \quad (6.25)$$

$$\phi = 45^\circ h_{ei} = 0.436\dot{q}^{0.778}T_i^{0.316} \quad [R^2=0.998] \quad (6.26)$$

$$\phi = 90^\circ h_{ci} = 403.43\dot{q}^{0.801}T_i^{-1.83} \quad [R^2=0.521] \quad (6.27)$$

$$\phi = 45^\circ h_{ci} = 1705.27\dot{q}^{-0.095}T_i^{0.098} \quad [R^2=0.508] \quad (6.28)$$

## 6.2.8 5/4"-Thermosyphon Results: Butane

Figure 6.12a and 6.12b illustrate energy balances of 10 % between the evaporator and condenser heat transfer rates for both the vertical and inclined operations. However, for the inclined operation, it is apparent that more heat is being recovered from the condenser than is being supplied to the evaporator. This is erroneous and it is felt that a consistent error is being achieved at this inclination angle. However, as this balance is within 10 %, it is felt that the effect of this error influences the results to a lesser extent. For these experiments, the heat fluxes ranged from 1800 - 42000 W/m<sup>2</sup> and the liquid fill charge ratio was 50 %. The maximum heat transfer rate for the vertical operation yielded a value of 4487.59 W at a  $\Delta T = 27^\circ\text{C}$  whilst the inclined operation yielded a heat transfer rate of 3885.19 W at the same  $\Delta T$ . The maximum heat transfer rate for the inclined operation was 5535.27 W at a  $\Delta T = 33.41^\circ\text{C}$ .

Figure 6.12c and 6.12d illustrate the comparison between the experimentally and predicted inside evaporator heat transfer coefficients for the vertical and inclined operation. For the vertical operation (Figure 6.12c), 97.7 % of the predicted values fell within 7.5 % of the experimentally determined values, whilst for the inclined operation (Figure 6.12d), 95.5 % of the predicted values fell within 7.5 % of the experimental values.

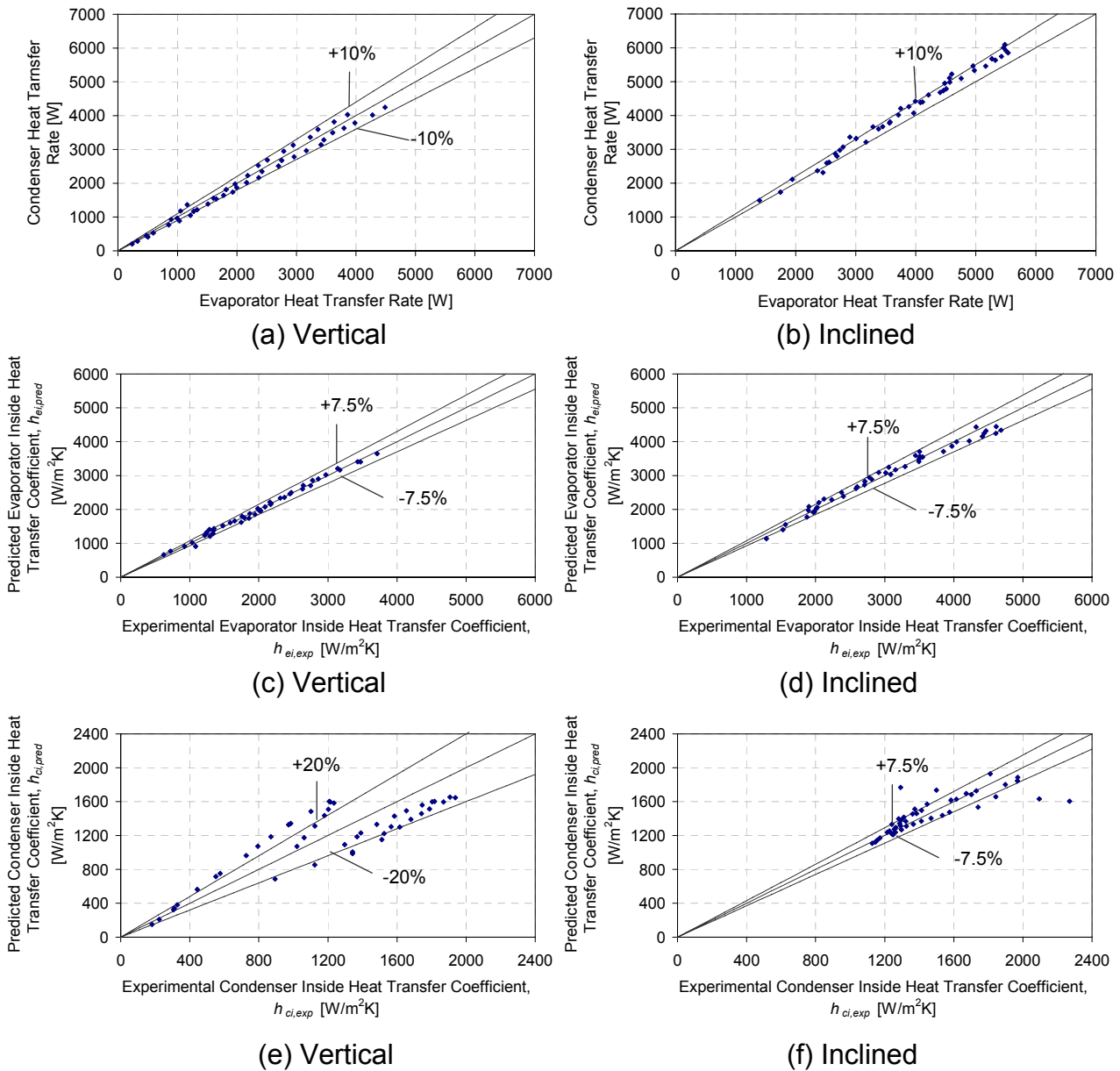


**Figure 6.12** Energy balances and inside evaporator and condenser heat transfer coefficients for the 5/4"-Thermosyphon operating with Butane charged at 50 % and operating vertically and at 45°

Figure 6.12e and 6.12f illustrate the comparison between the experimentally and predicted inside condenser heat transfer coefficients for vertical and inclined operation. For the

vertical operation, 60 % of the predicted values fell within 20 % of the experimental values and for the inclined operation, 84.4 % the values fell within 7.5 %.

The following correlations for the evaporator and condenser inside heat transfer coefficients were obtained for the vertical and inclined operation

$$\phi = 90^\circ h_{ei} = 0.752\dot{q}^{0.343}T_i^{1.473} \quad [R^2=0.989] \quad (6.29)$$

$$\phi = 45^\circ h_{ei} = 1.33\dot{q}^{0.906}T_i^{0.222} \quad [R^2=0.980] \quad (6.30)$$

$$\phi = 90^\circ h_{ci} = 30293\dot{q}^{1.4}T_i^{-4.767} \quad [R^2=0.874] \quad (6.31)$$

$$\phi = 45^\circ h_{ci} = 21195\dot{q}^{-0.044}T_i^{0.724} \quad [R^2=0.699] \quad (6.32)$$

### 6.3 Performance Correlating Equations for Thermosyphons

From the data sets used for the regression analysis in Section 6.2, two new data sets were generated. These new data sets included 360 data points for the thermosyphons operating vertically and 360 data points for the thermosyphons operating at 45°. Both data sets represented the thermosyphons operating with R134a and Butane as the working fluids and are given in Appendix E. In generating the various heat transfer coefficient equations in Section 6.2, it was assumed that the heat flux and the inside temperature influenced the heat transfer coefficients the most significantly. However, this section presents equations for the thermosyphons based on the physical properties and behaviour of the working fluids.

The equations presented in Section 3.1 were investigated to determine the variables most commonly used in heat transfer correlations. The variables that were of common occurrence in researchers' results were then grouped as the independent variables for the two new data sets. For the evaporator heat transfer coefficients, heat flux was a common variable in most of the equations. Other variables that were also deemed important included: orientation angle, diameter, Prandtl number, Jacob number, liquid fill charge ratio, Weber number, Froude number, Bond number, Kutateledze number, bubble length scale, Rayleigh number, Merrit number, latent heat of vaporisation and the density ratio. However, it would be cumbersome to generate equations using all these variables.

Multilinear regression techniques, using the 'least squares' method, were then used on the data sets with all of the aforementioned variables. The objective was to statistically eliminate variables that did not influence the evaporator inside heat transfer coefficients. For the statistical analysis, a confidence level of 95 % was chosen. The probabilities (p-value) of each of the aforementioned variables were then evaluated using the analysis of variance (ANOVA) table such that if the p-value of each variable was less than the confidence level, the null hypothesis could be rejected and the variable deemed influential. The further the p-value of the variable from the confidence level, the more dependent the variable. From this statistical analysis, the inside evaporator heat transfer coefficient is given as some function of the variables identified to be the most influential

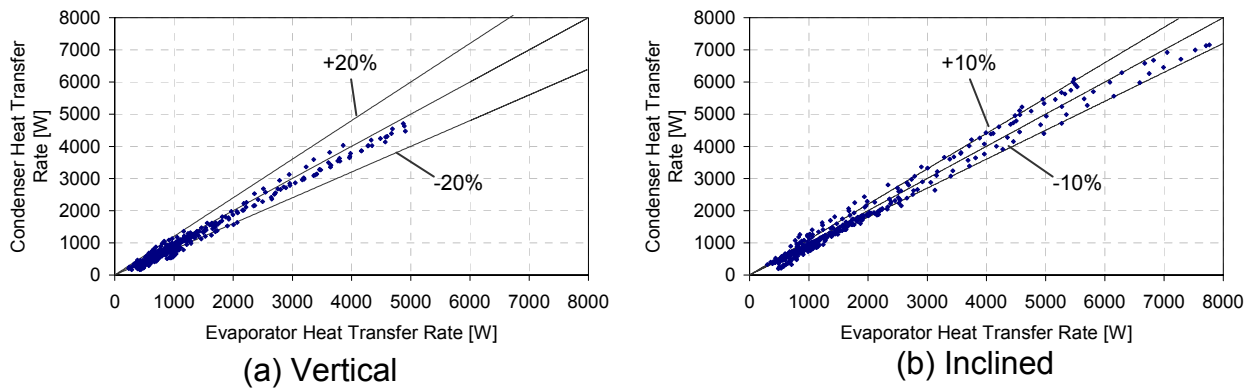
$$h_{ei} = f(\dot{q}, Ja, We, Fr, Ku, M) \quad (6.33)$$

Groups of these variables were then investigated using regression techniques such that the group with the best correlation coefficient ( $R^2$ ) was chosen. As the  $Ku$  is a well known heat transfer variable, it was decided to include it and leave out the heat flux (as the heat flux is included in the  $Ku$  number). A significant finding was that over the diameter range of 15–34 mm, the diameter did not give a good p-value and hence did not influence the heat transfer coefficient as would have been expected. The following correlations were generated for the inside evaporator heat transfer coefficients

$$\phi = 90^\circ \quad h_{ei} = 3.4516 \times 10^5 Ja^{-0.855} Ku^{1.344} \quad [R^2=0.794] \quad (6.34)$$

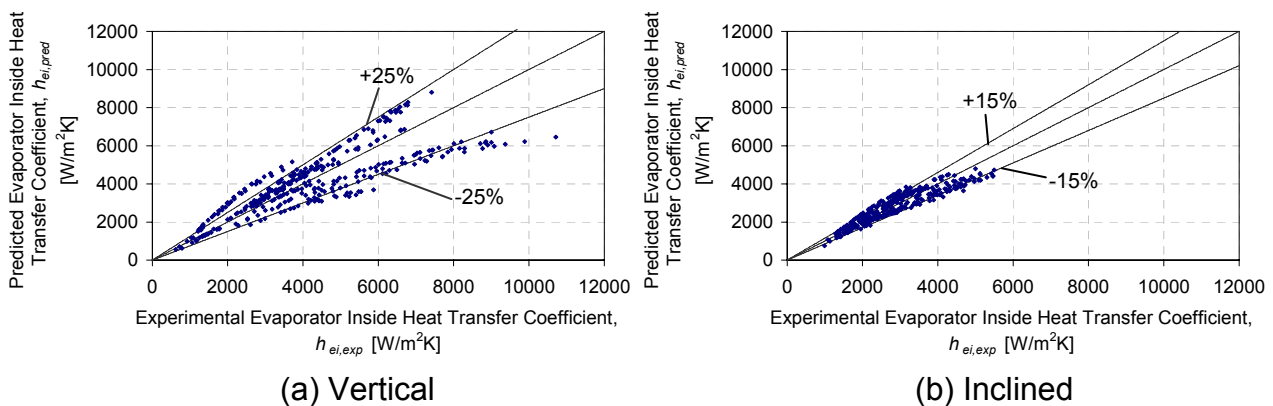
$$\phi = 45^\circ \quad h_{ei} = 1.4796 \times 10^5 Ja^{-0.993} Ku^{1.3} \quad [R^2=0.895] \quad (6.35)$$

Figure 6.13 illustrates the energy balances obtained for the evaporator and condenser heat transfer rates for both the vertical and inclined operations for the data sets created in Section 6.3. For the vertical operation (Figure 6.13a), the energy balance fell well within 20 % and for the inclined operation (Figure 6.13b) the balances fell within 10 %. These values were deemed acceptable and the heat transfer coefficients could therefore be analysed with confidence.



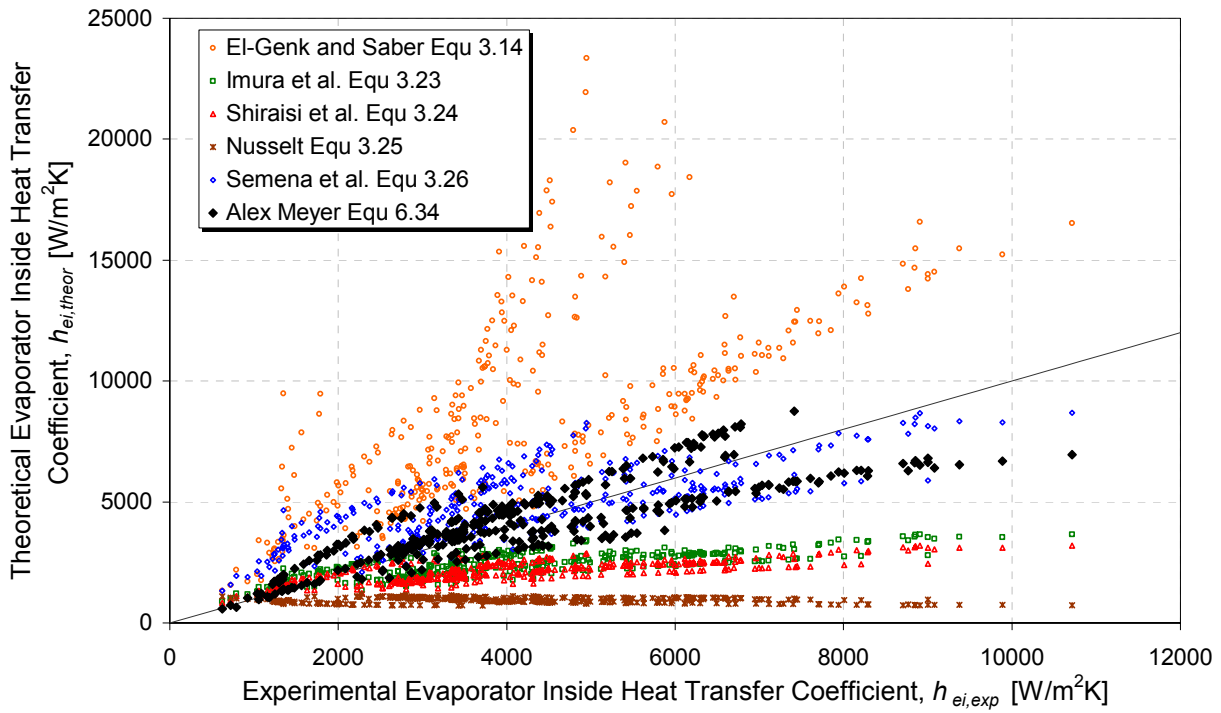
**Figure 6.13** Energy balances for the combined thermosyphon data sets operating vertically and inclined

Figure 6.14 illustrates the comparison between the predicted and experimentally determined inside evaporator heat transfer coefficients for vertical and inclined operation. For the vertical operation (Figure 6.14a), 78 % of the predicted values fell within 25 % of the experimental values and for the inclined operation (Figure 6.14b), 82.2 % the values fell within 15 %.



**Figure 6.14** Evaporator inside heat transfer coefficients for the combined thermosyphon data sets operating vertically and inclined

Figure 6.15a and 6.15b illustrate a comparison of the theoretically predicted evaporator inside heat transfer coefficients to that of the experimentally determined heat transfer coefficients. From both figures, it is evident that El-Genk and Saber's correlation over predict the heat transfer coefficients. The other researchers' correlations fall to within acceptable percentage differences of equations 6.34 and 6.35 and these percentage differences are illustrated in Table 6.1.



**Figure 6.15a** Comparison between theoretically determined evaporator inside heat transfer coefficients for vertical operation

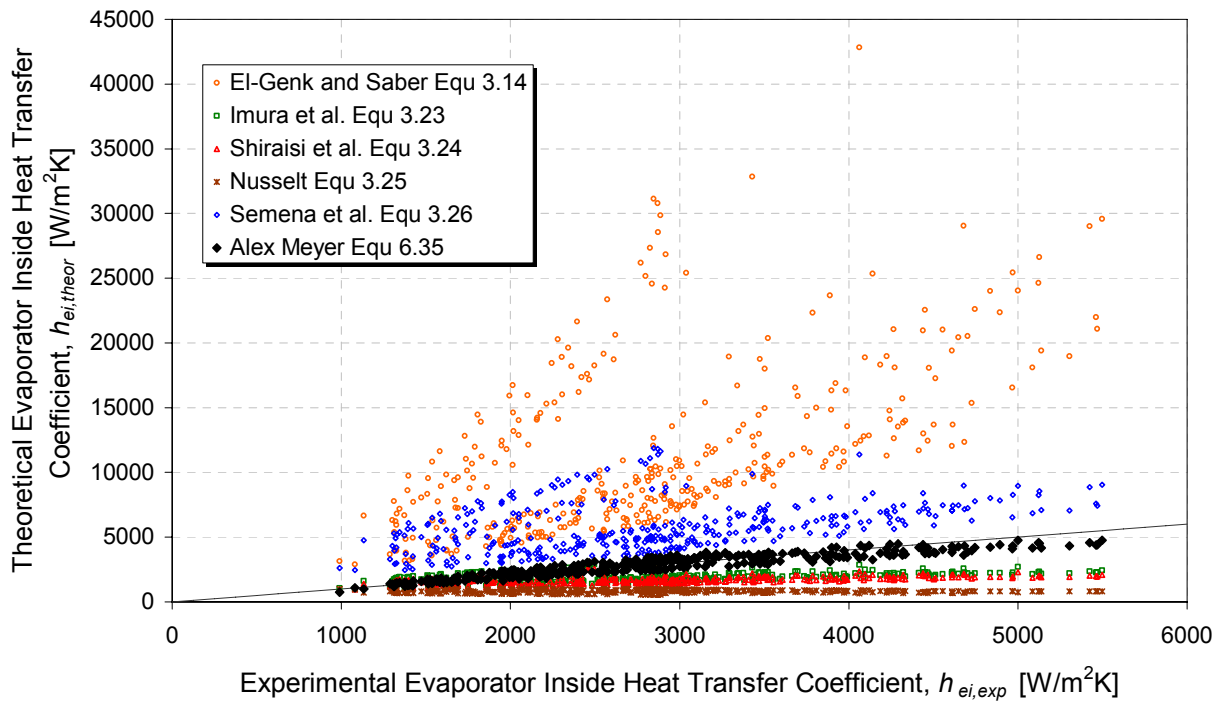


**Figure 6.15b** Comparison between theoretically determined evaporator inside heat transfer coefficients for inclined operation

**Table 6.1** Average percentage differences of equation 6.34 and 6.35 with respect to correlations presented in Section 3.1

	% Difference $\phi = 90^\circ$	% Difference $\phi = 45^\circ$
El-Genk and Saber (Equation 3.14)	-120	-316.84
Imura et al. (Equation 3.23)	33.75	26.59
Shiraishi et al. (Equation 3.24)	41.05	35.1
Nusselt (Equation 3.25)	70.95	66.97
Semena et al. (Equation 3.26)	-27	-117.82

To determine the condenser inside heat transfer coefficients, statistical techniques were used. For this, the various equations presented in Section 3.1 were investigated. The variables that were of common occurrence in previous researcher's correlations were then grouped as the independent variables to be investigated. The variables that were of common occurrence included: The Reynolds number, latent heat of vaporisation, diameter, thermal conductivity and the density ratio.

Multilinear regression techniques were used on the data sets with all of the aforementioned variables included in the regression analysis. A confidence level of 95 % was chosen and the probabilities of each of the aforementioned variables were investigated. This regression gave a correlation coefficient,  $R^2$  of 0.462, which is not a very good correlation, but as the condenser heat transfer coefficients remained relatively constant for each thermosyphon, it could be accepted. It was then decided to use the modified Nusselt number and the Reynolds number to predict the condenser inside heat transfer coefficient and compare this correlation coefficient value to that obtained using all the variables. This coefficient based on the Reynolds and modified Nusselt numbers yielded a correlation coefficient of 0.425. As the difference between the two correlation coefficients is minimal, it was decided to use the condenser heat transfer coefficient correlation based on the Reynolds and modified Nusselt numbers. The modified Nusselt number is given by equation 3.33 as

$$\bar{Nu}^* = \frac{\bar{h}}{k_l} \left[ \frac{v_l^2 \left( \frac{\rho_l}{\rho_l - \rho_v} \right)}{g} \right]^{\frac{1}{3}} \quad (6.36)$$

Which can be re-written to yield the inside condenser heat transfer coefficient as a function of

$$h_{ci} = f \left( \text{Re}_i, \frac{k_l}{\left[ \frac{v_l^2}{g} \left( \frac{\rho_l}{\rho_l - \rho_v} \right) \right]^{1/3}} \right) \quad (6.37)$$

The following equations were generated using multi-linear regression techniques on the combined data sets using the variables given in equation 6.37

$$\phi = 90^\circ \quad h_{ci} = 4.61561 \times 10^9 \text{Re}_i^{0.364} \left[ k_l / \left[ \frac{v_l^2}{g} \left( \frac{\rho_l}{\rho_l - \rho_v} \right) \right]^{1/3} \right]^{-2.05} \quad [R^2=0.425] \quad (6.38)$$

$$\phi = 45^\circ \quad h_{ci} = 3.7233 \times 10^{-5} \text{Re}_i^{0.136} \left[ k_l / \left[ \frac{v_l^2}{g} \left( \frac{\rho_l}{\rho_l - \rho_v} \right) \right]^{1/3} \right]^{1.916} \quad [R^2=0.121] \quad (6.39)$$

Figure 6.16 illustrates the comparison between the theoretically predicted inside condenser heat transfer coefficients and the experimentally determined heat transfer coefficients for the vertical and inclined operations. For the vertical operation (Figure 6.16a), 61.1 % of the predicted values fell within 25 % of the experimental values and for the inclined operation (Figure 6.16b), 74.4 % the values fell within 25 %.

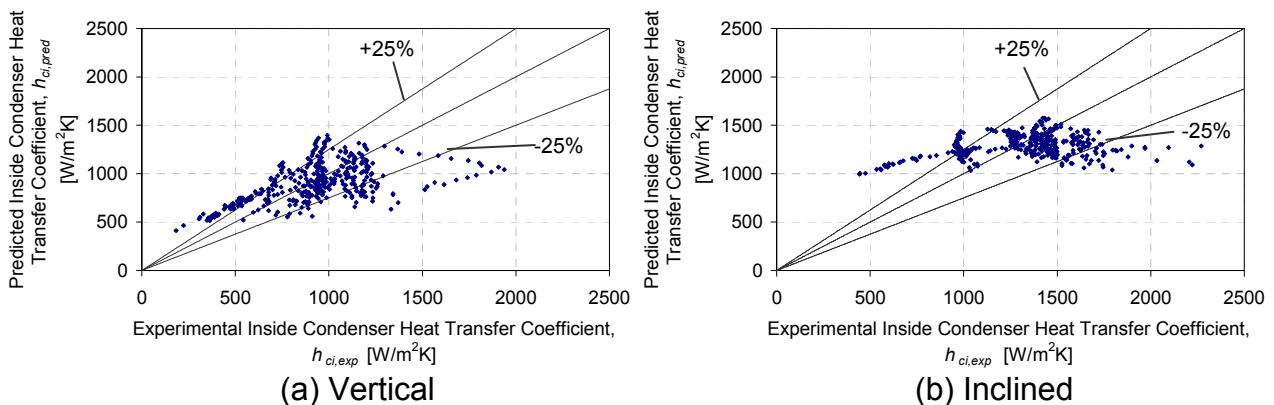


**Figure 6.16** Condenser inside heat transfer coefficients for the combined thermosyphon data sets operating vertically and inclined

Figure 6.17a and 6.17b illustrate the comparison of the theoretically predicted condenser inside heat transfer coefficients and the experimentally determined condenser heat transfer coefficients. The various correlations presented by researchers in Section 3.1 are



plotted against the experimentally determined condenser inside heat transfer coefficient. The theoretical correlations given by equations 6.38 and 6.39 compare relatively well with those of previous research. However, the Wang and Ma correlation yields much larger values for the heat transfer coefficient. Reasons for this are unknown and it can only be assumed that their correlation does not simulate the use of R134a or Butane.

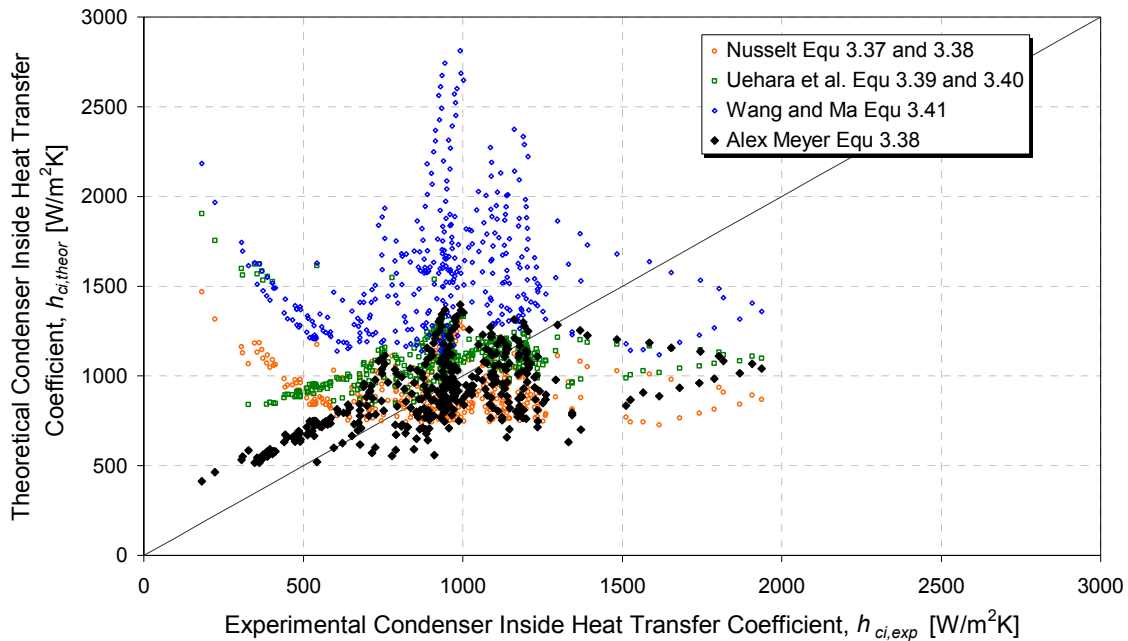


**Figure 6.17a** Comparison between theoretically determined condenser inside heat transfer coefficients for vertical operation

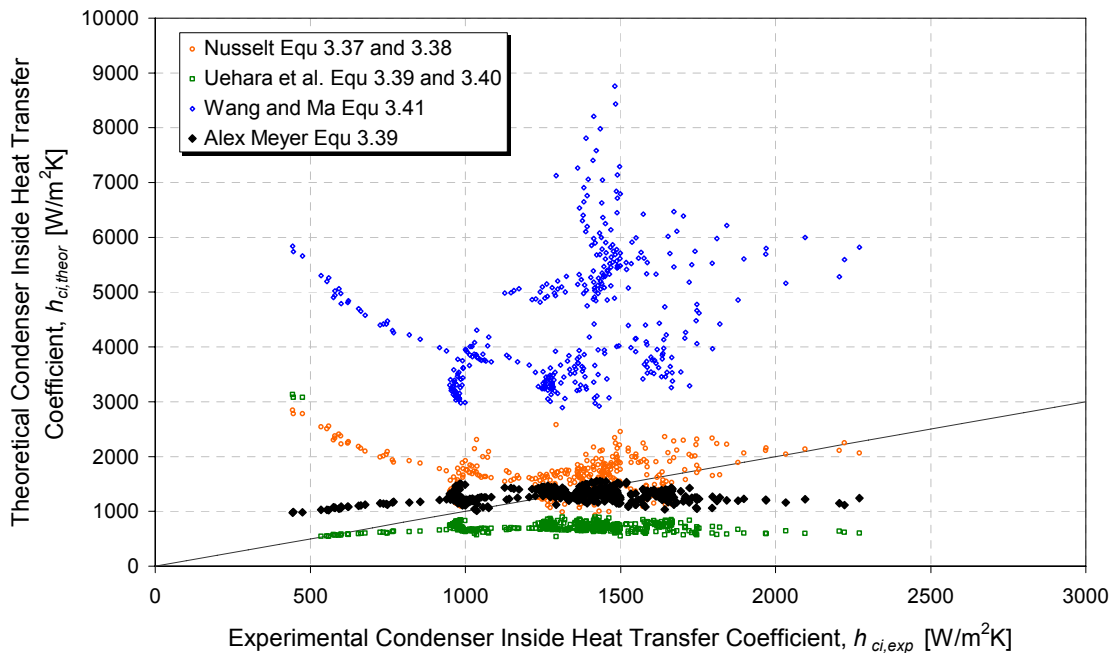


**Figure 6.17b** Comparison between theoretically determined condenser inside heat transfer coefficients for inclined operation

Flooding is a precursor for the maximum heat transfer rate. The maximum heat transfer rates for the thermosyphons were then calculated assuming that at the flooding point, the maximum heat transfer rate is obtained. Section 2.2.2 gives a correlation for the maximum heat transfer rate. From this correlation, the Kutateladze and Bond numbers are seen to be important variables. The Bond number includes the diameter and it is clear that the smaller the diameter, the greater the chance of flooding occurring. The following equations were generated using multi-linear regression techniques

$$\phi = 90^\circ \quad \dot{Q}_{\max} = 1.6553 \times 10^6 Bo^{0.3156} Ku^{1.6040} \quad [R^2=0.928] \quad (6.40)$$

$$\phi = 45^\circ \quad \dot{Q}_{\max} = 7.4685 \times 10^6 Bo^{0.2101} Ku^{1.9189} \quad [R^2=0.962] \quad (6.41)$$

Figure 6.18 illustrates the comparison between the theoretically predicted maximum heat transfer rates and the experimentally determined maximum heat transfer rates for the vertical and inclined operations. For the vertical and inclined operations, 76.5 % of the predicted values fell within 15 % of the experimental values. Equations 6.40 and 6.41 could however not be compared to the correlation given in Section 2.2.2 as the constants used in equation 2.10 are not documented for R134a and Butane.

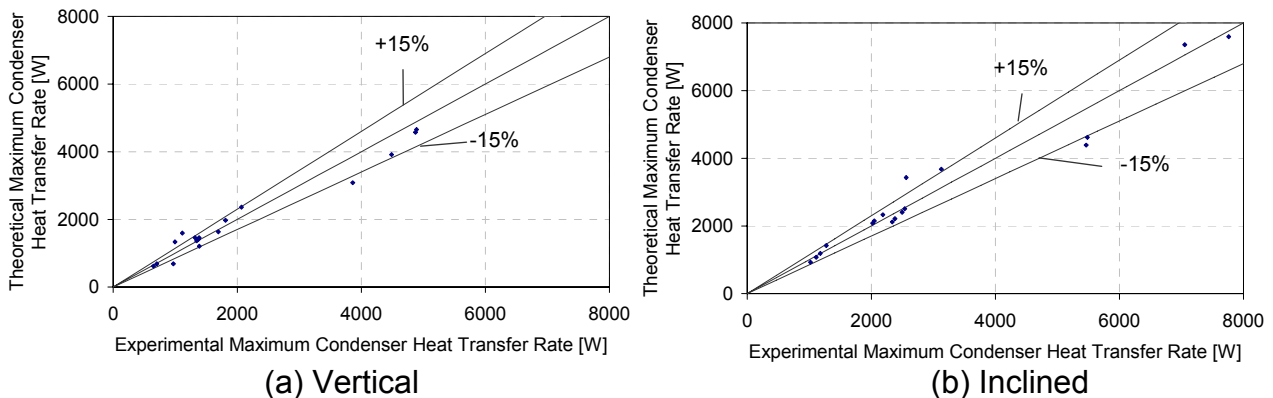
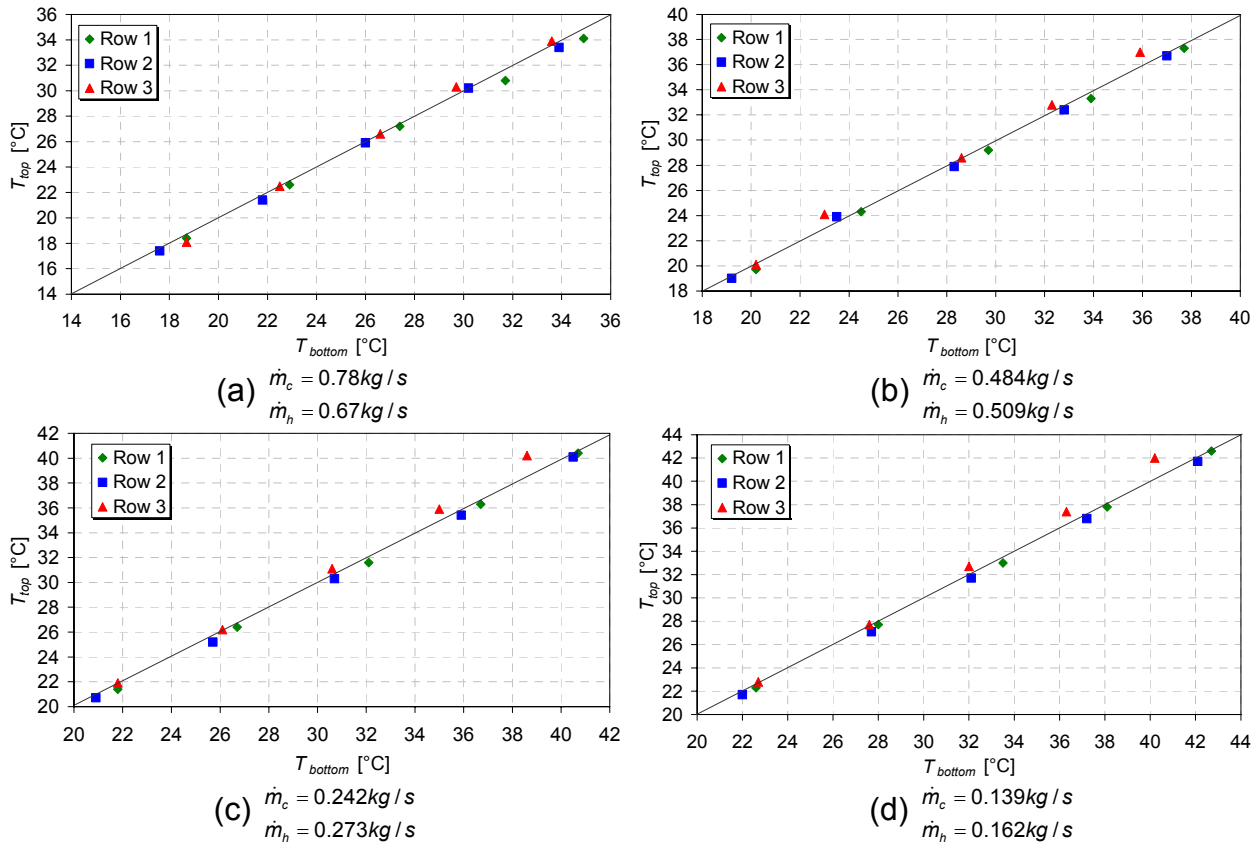


**Figure 6.18** Maximum heat transfer rates for the combined thermosyphon data sets operating vertically and inclined charged

## 6.4 Inside Temperature Distribution of a HPHE and Comparison with the Mathematical Model

Figure 6.19 illustrates the inside top and bottom temperatures of the manifolded rows of the HPHE described in Section 5.2 operating at different air mass flow rates. As would be expected, the inside measured temperatures at the top are similar to the inside

temperatures measured at the bottom. It is also noticed that in all the experiments, the inside temperature measured at the top for row 3, is slightly higher than the bottom temperature. This might be as a result of the thermocouple touching the side wall of the manifold.



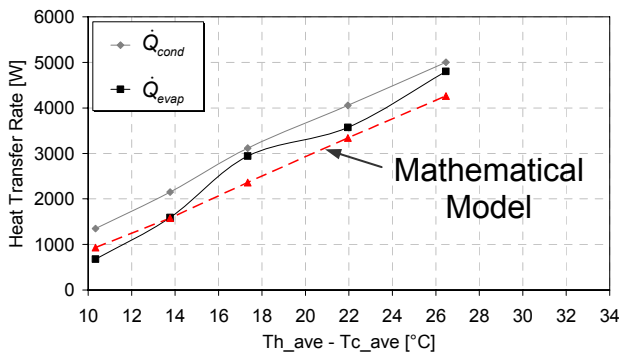
**Figure 6.19** Inside temperature distributions of the manifolded rows of the laboratory tested HPHE at different hot and cold air mass flow rates

Figure 6.20 illustrates the different heat transfer rates for the condenser and evaporator sections of the HPHE as a function of  $T_{h\_ave} - T_{c\_ave}$ . These are then compared with the values obtained from the mathematical model used in the computer simulation code given in Appendix C. It can be seen that the condenser heat transfer rates are slightly lower than the evaporator heat transfer rates even though the theoretically calculated heat losses were taken into account. Reasons for these differences might be attributed to the fact that the anemometer measurements for the velocities might have been inaccurate as the anemometer might not have been directly perpendicular to the flow field when the measurements were taken. The fact that only the losses from the HPHE were calculated and not the losses from the un-insulated tunnel sections (see Section 5.2.2), might also have influenced the evaporator values being higher than the condenser sections' values.

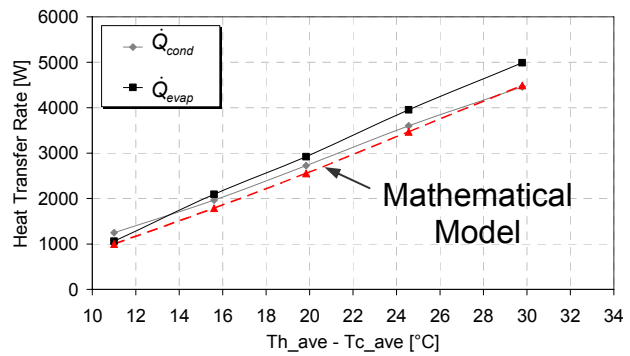
It can also be seen from Figure 6.20 that the mathematical model under predicts the actual heat transfer rate that is being obtained. For the mathematical model, the heat transfer resistances were calculated using the Colburn j-factor (as described in Section 3.2.2). The Colburn j-factors are however empirically determined and therefore allow for inaccuracies. It should however be noted that on average, the percentage difference between the actual laboratory experiments as undertaken per Section 5.2, and the mathematical model are only in the order of 8 % lower than the actual heat transfer rates obtained.

From Figure 6.20b, it can be seen that for the given mass flows, a heat recovery ( $\dot{Q}_{cond}$ ) of 4.5 kW can be achieved with an input heat source ( $\dot{Q}_{evap}$ ) of 5 kW, yielding an efficiency

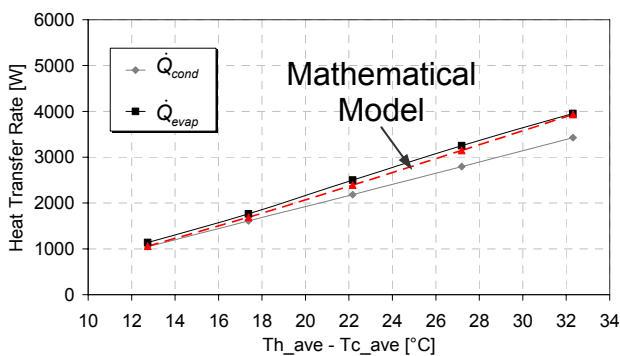
$$\text{based on these values of } \eta = \frac{\dot{Q}_{cond}}{\dot{Q}_{evap}} \times 100 = \frac{4500}{5000} = 90\%.$$



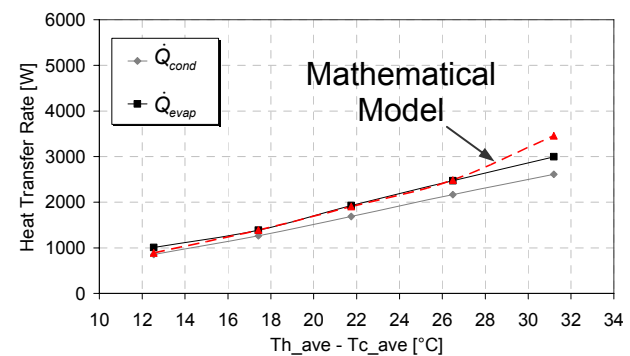
(a)  $\dot{m}_c = 0.78 \text{ kg / s}$   
 $\dot{m}_h = 0.67 \text{ kg / s}$



(b)  $\dot{m}_c = 0.484 \text{ kg / s}$   
 $\dot{m}_h = 0.509 \text{ kg / s}$



(c)  $\dot{m}_c = 0.242 \text{ kg / s}$   
 $\dot{m}_h = 0.273 \text{ kg / s}$



(d)  $\dot{m}_c = 0.139 \text{ kg / s}$   
 $\dot{m}_h = 0.162 \text{ kg / s}$

**Figure 6.20** Comparison between the evaporator and condenser heat transfer rates and the mathematical model of the laboratory tested HPHE at different mass flow rates

## 6.5 Demonstration Experiments on the CFW/Yucon HPHE

The CFW/Yucon HPHE described in Section 4 was used as the demonstration model to ascertain the economic viability of using such a HPHE in an industrial type drying application. Figure 6.21 illustrates an experiment on the air-drier unit with the CFW/Yucon HPHE. To illustrate the heat that can be recovered from the system, consider the values at a time of 35 minutes. Table 6.2 illustrates the values at this time.

**Table 6.2** Demonstration of the attainable heat recovery

Inlet Hot Temperature [°C]	Exit Hot Temperature [°C]	Inlet Cold Temperature [°C]	Exit Hot Temperature [°C]
51.64	35.9	14.85	30.63

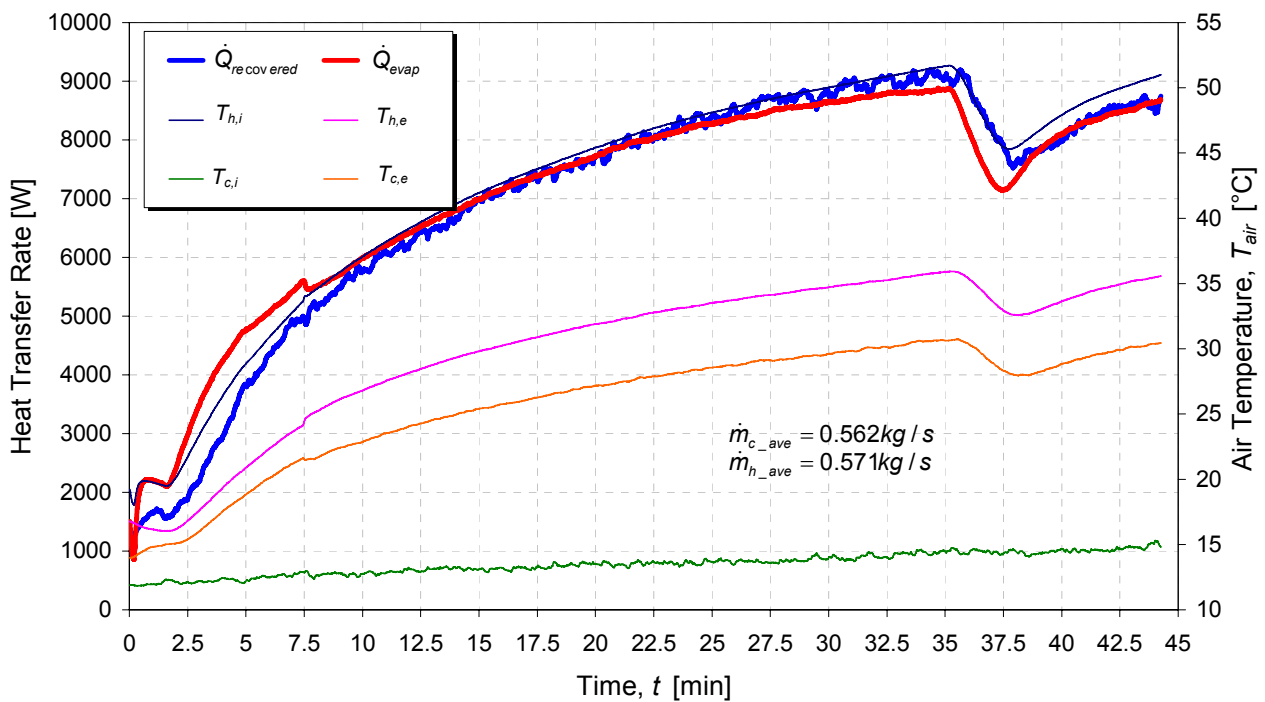


**Figure 6.21** Heat recovery of the demonstration HPHE

The heat input to the drier is given by the heat transfer rate in the evaporator section of the HPHE, calculated as  $\dot{Q}_{evap} = \dot{Q}_{in} = 0.557 \times 1007.69 \times (51.64 - 35.9) = 8834.59 \text{ W}$ . The heat that is recovered from the CFW/Yucon HPHE is the fresh air that enters the HPHE and

leaves at a higher temperature where it is then passed back into the drier unit. This heat recovery is given by  $\dot{Q}_{cond} = \dot{Q}_{recovered} = 0.556 \times 1006.80 \times (30.63 - 14.85) = 8833.34 \text{ W}$ .

The heat recovered is  $\frac{(\dot{Q}_{evap} - \dot{Q}_{recovered})}{\dot{Q}_{evap}} = \frac{8834.59 - 8833.34}{8834.59} \times 100 = 0.014\%$

higher than the heat that is actually supplied to the HPHE ( $\dot{Q}_{in}$ ). This small error is attributed to the anemometer not measuring the velocities in the ducting accurately enough.

Figure 6.22 illustrates the kWh-meter readings over a five hour time period with and without the HPHE installed onto the air-drier unit. As can be seen, 52.2 kWh is obtained when the drier unit operates as it normally would. A kWh reading of 35.4 kWh is obtained when the HPHE is installed onto the drier unit, yielding a saving of  $\frac{52.2 - 35.4}{52.2} \times 100 = 32.18\%$  over a 5 hour time period. To analyse the recovery in financial terms, the initial costs of the CFW/Yucon HPHE along with the running costs are considered. The costs to operate the drier unit with and without the HPHE are then evaluated from which the payback period and savings each year can be calculated. Where necessary, values were estimated as CFW installed the demonstration HPHE themselves and the ducting and reducer sections were sourced in-house.

From Table 6.3, it can be seen that it will take approximately 3.2 years to pay the HPHE off. Thereafter, a saving of 29.51 % can be obtained. It should however be noted that the CFW/Yucon HPHE was coated with a special anti-corrosive coating which increased the HPHE's initial cost by nearly 50 % and hence a shorter payback period could have been achieved without this protective coating. Should the HPHE be mass produced, the manufacturing costs could further decrease and the payback period appropriately reduced. It should also be noted that as this installation was a retrofit to the existing drier unit, the installation costs were higher than if the HPHE was designed into the drier unit system from the start. Should the HPHE be designed into the drier system from the start, costs such as the reducer costs, connector piping and labour could be reduced as there is a smaller scope of supply. Table 6.3 also illustrates different installation scenarios. The experiments were undertaken in winter and it is however expected that the savings could be improved in summer as higher new inlet temperatures into the drier unit can be obtained as the ambient air temperature (that enters the HPHE) will be higher.

In addition to the energy savings from the HPHE, drier inside temperatures can be reached faster than what would normally be the case. Figure 6.23 illustrates the drier unit temperature with respect to time with and without the HPHE installed. For the experiment, the drier temperature was set to 50 °C. As can be seen from Figure 6.23, the inside drier temperature is reached after 30 minutes when the HPHE is installed onto the drier unit. It is also noticed that the drier never reaches 50 °C operating without the HPHE under the specified operating conditions given in Section 5.3.2. It should be noted that these operating conditions were not ideal but were used merely to compare the operation of the drier unit with and without the HPHE, directly.

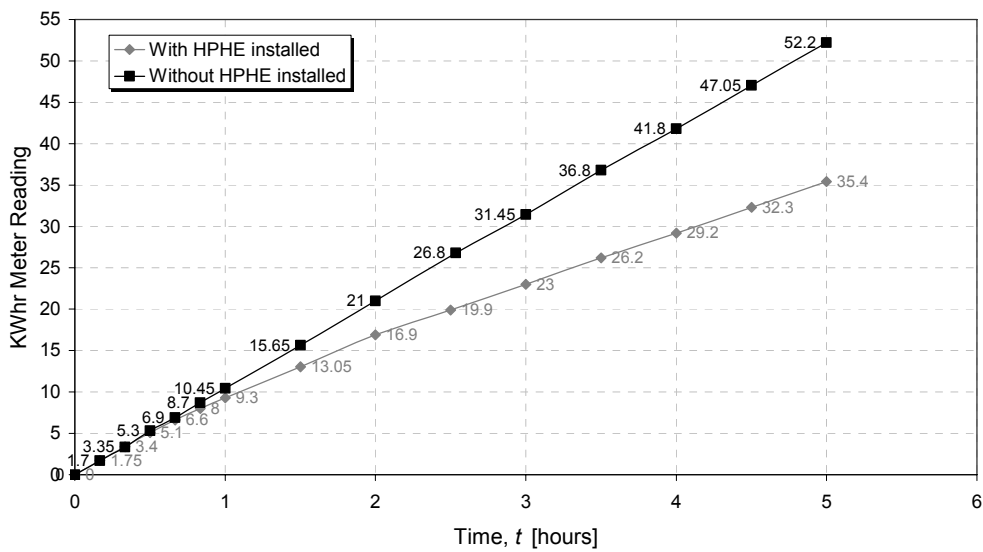


**Figure 6.22** kWhr Meter Readings for the drier unit operation with and without the demonstration HPHE installed

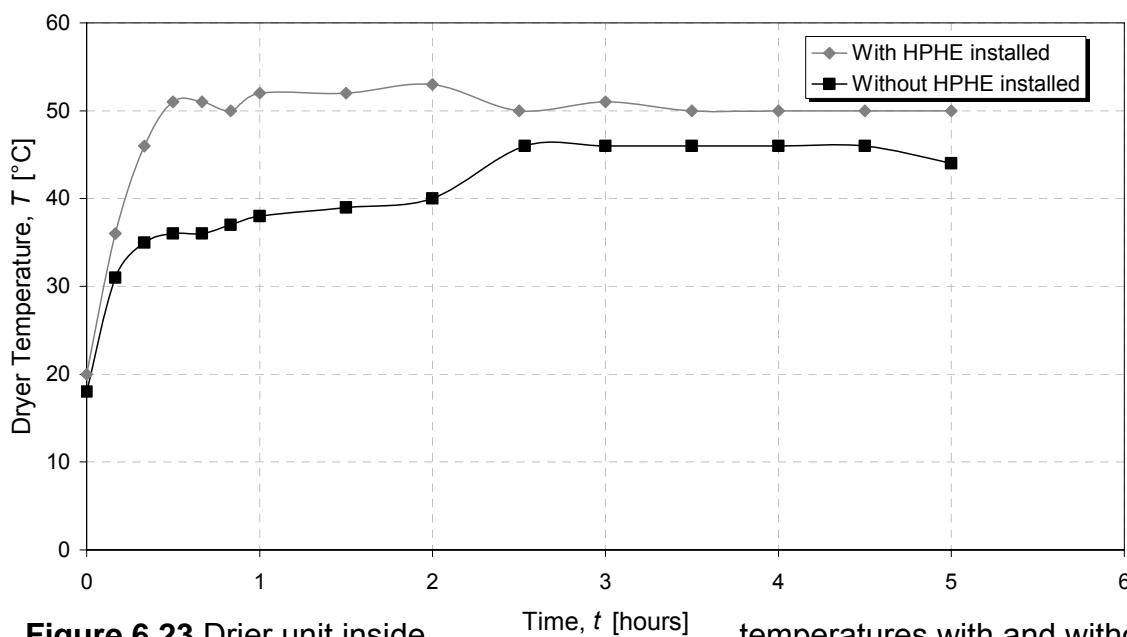


**Figure 6.23** Drier unit inside temperatures with and without the HPHE installed

**Table 6.3** Energy savings for the installed CFW/Yucon HPHE

<b>Initial costs for the CFW/Yucon HPHE</b>	<b>Retrofit</b>	<b>New Installation</b>	
CFW/Yucon HPHE with protective coating [R]	2660	2660	2660
Protective coating	2230.6	2230.6	-
Variable speed fan [R]	1000	1000	1000
Ducting @ R7.75/m	77.5	-	-
Reducer sections to HPHE [R]	500	-	-
Labour [R]	1000	-	-
<b>Total Initial Costs [R]</b>	<b>7468.1</b>	<b>5890.6</b>	<b>3660</b>
<b>Running Costs/year</b>			
Maintenance [R]	400	400	400
<b>Total Running Costs [R]</b>	<b>400</b>	<b>400</b>	<b>400</b>
<b>Total Initial Cost</b>	<b>7868.1</b>	<b>6290.6</b>	<b>4060</b>
<b>Energy usage without HPHE</b>			
kWh Reading over 5 hours [kWh]	52.2	52.2	52.2
kWh Reading over 1 hour [kWh]	10.44	10.44	10.44
Operating shifts	250	250	250
Hours per shift [h]	18	18	18
Energy cost [R/kWh]	0.18	0.18	0.18
<b>Total Energy [R/year]</b>	<b>8456.4</b>	<b>8456.4</b>	<b>8456.4</b>
<b>Energy usage with HPHE</b>			
kWh Reading over 5 hours [kWh]	35.4	35.4	35.4
kWh Reading over 1 hour [kWh]	7.08	7.08	7.08
Operating shifts	250	250	250
Hours per shift [h]	1	18	18
Energy cost [R/kWh]	0.18	0.18	0.18
<b>Total Energy [R/year]</b>	<b>5734.8</b>	<b>5734.8</b>	<b>5734.8</b>
<b>HPHE Saving/Year - Running Costs [R/year]</b>	<b>2321.6</b>	<b>2321.6</b>	<b>2321.6</b>
<b>Payback period [Years]</b>	<b>3.2</b>	<b>2.5</b>	<b>1.57</b>



Figure 6.24 illustrates the comparison between the mathematical model used in the computer simulation code to that of a set of data points taken from the experimental run represented by Figure 6.21. It can be seen that the mathematical model under predicts the actual heat transfer rate that is being obtained for lower temperature differences between the hot and cold air but this error decreases with an increase in the aforementioned temperature difference. Reasons for the under prediction could be as a result of the Colburn j-factors being used as discussed in Section 6.4. It should however be noted that on average, the percentage difference between the experimental results and the mathematical model are only in the order of 11.7 % and it is felt that the computer code can therefore be used with confidence bearing in mind that the heat transfer resistances are calculated using empirically determined correlations.

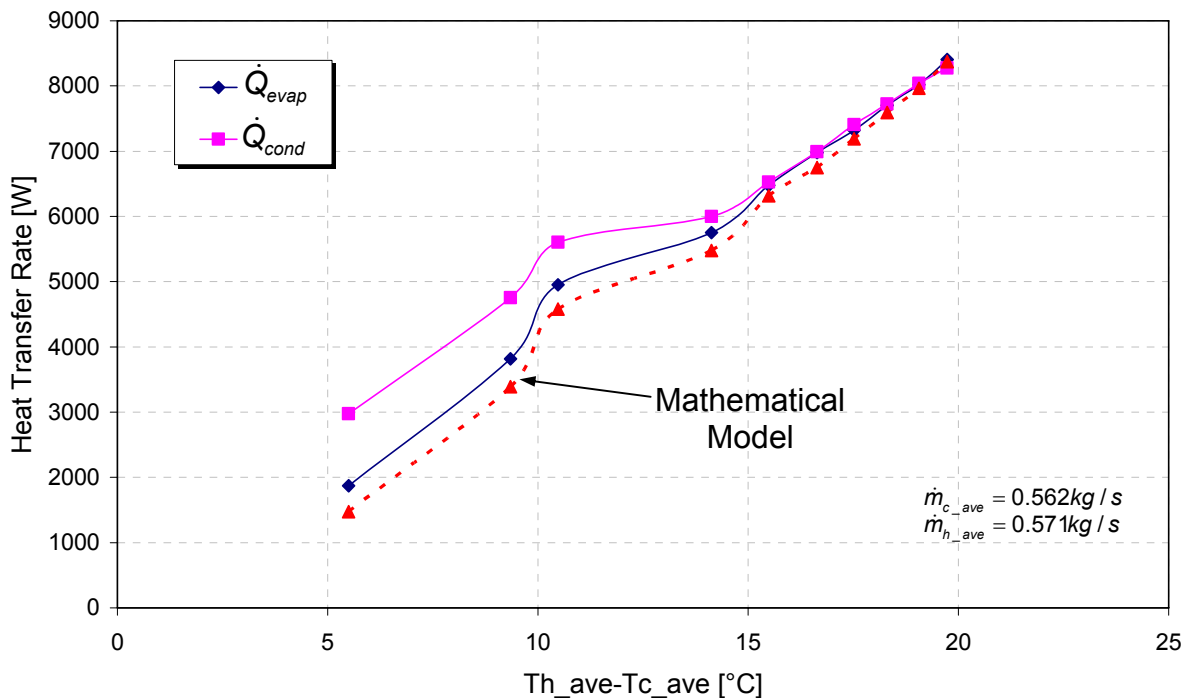


**Figure 6.24** Comparison between the mathematical model and experimentally determined heat transfer rates using the in-field CFW/Yucon HPHE

## 7 DISCUSSIONS AND CONCLUSIONS

A literature study helped in understanding the performance parameters and the characteristics for thermosyphon and heat pipe operations. From the literature study, performance parameters such as the evaporator to condenser length ratios, the diameter and the orientation angle of the thermosyphons were identified to be primary parameters. The evaporator and condenser inside heat transfer coefficients and the maximum heat transfer rate were identified as the most important characteristics for thermosyphon operation and were therefore identified as one of the focal areas of this thesis.

Owing to the chaotic behaviour of two-phase flow, the modelling of the inside evaporator and condenser heat transfer coefficients is difficult to simulate. As a result, it is common practice to model these heat transfer coefficients based on experimental data. Numerous correlations for these heat transfer coefficients have been proposed for different working fluids and thermosyphon geometries. However, these correlations fail to include adequate modelling of R134a and Butane as working fluids. One of the main focus areas of this thesis was therefore to develop heat transfer coefficients ( $h$ -values) for R134a and Butane as working fluids for different thermosyphon geometries and orientations.

To develop the evaporator and condenser inside heat transfer coefficients, three different diameter copper thermosyphons of the same total lengths of 1.03 m were used. The evaporator to condenser length ratios were 1 and remained constant for the experiments. Furthermore, a stainless steel thermosyphon with a total length of 6.2 m was used and which had an evaporator to condenser length ratio of 0.24. The diameter of this stainless steel thermosyphon also varied from those of the copper thermosyphons. A liquid fill charge ratio of 50 % based on the evaporator length of the thermosyphons was used throughout the experiments. The thermosyphons operated vertically and at an inclination angle of 45 ° to the horizontal.

For the thermosyphon experiments, the heat fluxes ranged from 1800-43500 W/m<sup>2</sup> and energy balances between the condenser and evaporator heat transfer rates were found to be typically between 5 % and 20 % (see Section 6.2). The validity of the experiments did however provide for some uncertainties. These uncertainties were evident in some of the energy balances between the evaporator and condenser heat transfer rates even though

losses to the environment were taken into account. Possible reasons might have been inaccurate mass flow and temperature measurements. The mass flows measurements were repeated and different thermocouples utilized in the experiments in an attempt to curb this inaccuracy problem. However, the same results were obtained in which the energy balances did not satisfy the conservation of energy. Reasons for these uncertainties have as yet not been identified.

Where the energy balances were deemed unsatisfactory owing to large percentage differences between the condenser and evaporator sections, the liquid fill charge ratio was investigated. For example, the 5/8"-Thermosyphon experiments charged with R134a with a liquid fill charge ratio of 50 % (see Section 6.2.1). It was found that for smaller thermosyphon diameters, large liquid fill charge ratios of 50 % resulted in the working fluid being 'blasted' to the top of the thermosyphon where the fluid would 'sit' and prevent the two-phase cycle from continuing. By reducing the fill charge ratio to 25 %, typical energy balances were improved from 40 to 30 % and from 60 to 10 % for the vertical and inclined operations.

It was found that the orientation angle of the thermosyphon influenced the heat transfer capabilities significantly. For the copper thermosyphons with R134a as the working fluid, the evaporator inside heat transfer coefficients ( $h_{ei}$ ) for the inclination angle of 45° were shown to be 29 % lower on average than for the vertical operation. The condenser inside heat transfer coefficients ( $h_{ci}$ ) however, were shown to be 29.67 % higher. For the stainless steel thermosyphon,  $h_{ei}$  values of 72 % lower and  $h_{ci}$  values of 50 % higher on average were obtained for the inclined operation compared to the vertical operation. When the copper thermosyphons were charged with Butane, similar results occurred with the  $h_{ei}$  values shown to be on average 24 % lower and the  $h_{ci}$  values 53.5 % higher for the inclined operation compared to the vertical operation. For the stainless steel thermosyphon,  $h_{ei}$  values of 35 % lower and  $h_{ci}$  values of 53 % higher on average were obtained for the inclined operation compared to the vertical operation.

The use of R134a and Butane as working fluids was also found to influence the results significantly. It was found that higher heat transfer rates were obtained for the thermosyphons charged with R134a as the working fluid than those charged with Butane for similar temperature differences. For example, the 5/8"-Thermosyphon charged with R134a yielded a heat transfer rate of 1160.461 W at a temperature difference of 23.24 °C

whilst the Butane charged thermosyphon yielded a value of 730.08 W at a temperature difference of 22.46 °C. This phenomenon was evident despite the fact that Butane has a higher latent heat of vaporization on average than that of R134a (at 30 °C  $h_{fg-Butane} = 341827.4$  J/kg and  $h_{fg-R134a} = 173290$  J/kg). A possible reason for this is that a mixture of commercial gas-lighter fuel was used to simulate Butane (see Appendix A) for reasons of availability, cost and convenience. The mixture properties as supplied by the manufacturer are: 54 % n-butane, 24 % iso-butane and 22 % propane. It is suggested that only the n-butane is boiling whilst the propane and iso-butane components might be hindering the boiling for instance, but improving the 'splashing factor' in the evaporator. This 'splashing' factor is proposed by Groenewald (2001) and involves introducing a factor in the heat transfer coefficient to account for the 'splashing' nature of the working fluid inside the thermosyphon.

Inside heat transfer coefficients were formulated for each thermosyphon with R134a and Butane as the working fluids and at vertical and inclined orientation angles. These predicted  $h$ -values were generated using multi-linear regression techniques and it was found that the predicted  $h$ -values correlated the experimental  $h$ -values typically between 5-15 % for the respective thermosyphons as can be seen in Section 6.2. Equations were then formulated for the thermosyphons whereby the physical behaviour of the working fluids could be simulated. For the evaporator inside heat transfer coefficients, the equations included the dimensionless Kutateledze and Jacob numbers as variables. These numbers were used as they include important two-phase flow parameters such as the heat flux, the liquid and vapour densities and the latent heat of vaporisation. The evaporator inside heat transfer coefficients for different inclination angles are given by equation 6.34 and 6.35 and are repeated for convenience by

$$\phi = 90^\circ \quad h_{ei} = 3.4516 \times 10^5 Ja^{-0.855} Ku^{1.344} \quad (7.1)$$

$$\phi = 45^\circ \quad h_{ei} = 1.4796 \times 10^5 Ja^{-0.933} Ku^{1.3} \quad (7.2)$$

Figure 7.1 illustrates theoretically predicted evaporator inside heat transfer coefficients against those determined experimentally. From the figure, it can be seen that grossly inaccurate correlations with the El-Genk and Saber (1997) correlations are achieved. Reasons for this are attributed to their experimental data not including R134a and Butane as working fluids. The thermosyphons from which the correlations were generated might also have had grossly differing geometries to those of this thesis. It is however found that

equations 7.1 and 7.2 correlate well with the other proposed correlations found in Section 3.

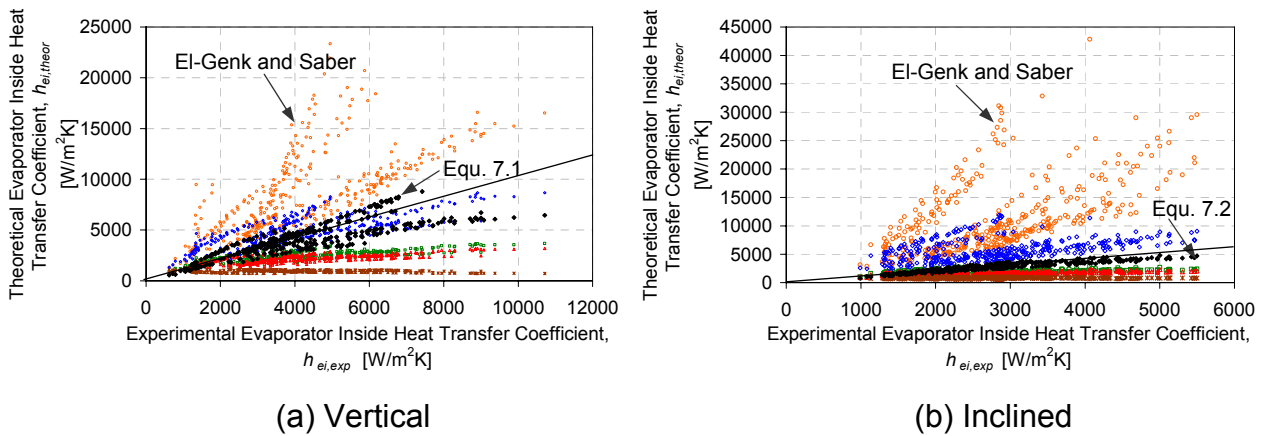


**Figure 7.1** Comparison between theoretically determined evaporator inside heat transfer coefficients (smaller copy of Figure 6.15)

Inside condenser heat transfer coefficients were also formulated using multi-linear regression techniques. Low correlation coefficients ( $R^2$ ) for the regression were found for the vertical and inclined data sets. These low correlation coefficients are a result of the condenser inside heat transfer coefficients remaining relatively constant for an increase in temperature difference (see Figure 6.16). Multi-linear regression techniques to formulate these condenser inside heat transfer coefficients are therefore not appropriate and formulating these coefficients with a power series is a suggestion. Figure 7.2 illustrates the comparison between the theoretically predicted condenser inside heat transfer coefficients and the experimentally determined inside condenser heat transfer coefficients. The condenser inside heat transfer coefficients for different inclination angles are given by equation 6.36 and 6.37 and are repeated for convenience by

$$\phi = 90^\circ \quad h_{ci} = 4.61561 \times 10^9 \text{ Re}_l^{0.364} \left[ k_l / \left[ \frac{v_l^2}{g} \left( \frac{\rho_l}{\rho_l - \rho_v} \right) \right]^{1/3} \right]^{-2.05} \quad (7.3)$$

$$\phi = 45^\circ \quad h_{ci} = 3.7233 \times 10^{-5} \text{ Re}_l^{0.136} \left[ k_l / \left[ \frac{v_l^2}{g} \left( \frac{\rho_l}{\rho_l - \rho_v} \right) \right]^{1/3} \right]^{1.916} \quad (7.4)$$

Comparison of equations 7.3 and 7.4 show reasonable accuracy with those of proposed correlations given in Section 3. It is however found that the Wang and Ma (1991)

correlation grossly over-predicts the theoretical correlation proposed by equation 7.3 and 7.4 for both the vertical and inclined operations.

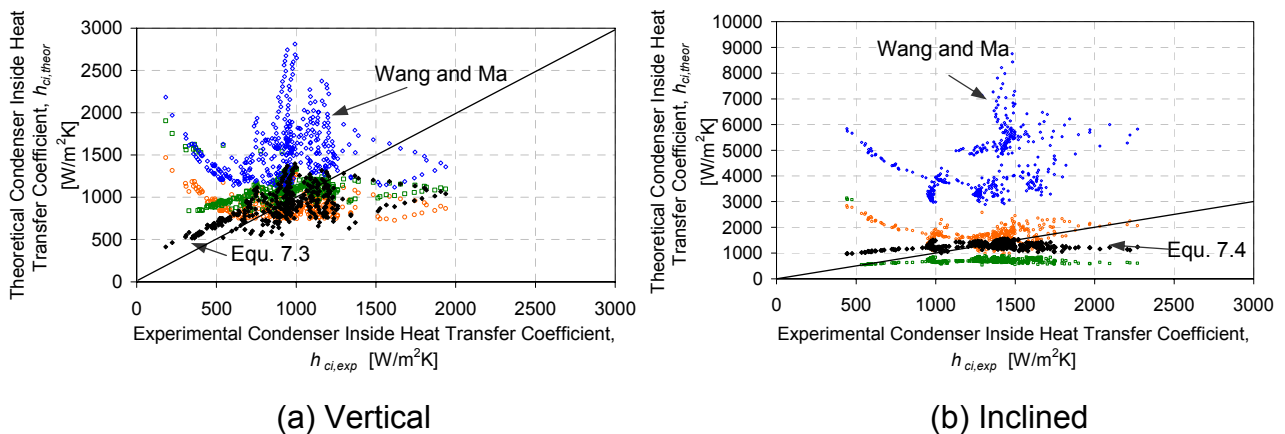


**Figure 7.2** Comparison between theoretically determined evaporator inside heat transfer coefficients (smaller copy of Figure 6.17)

Equations representing the maximum heat transfer rates of thermosyphons operating vertically and inclined were also generated. However, these equations could not be compared with those proposed by Faghri (1995) in Section 2.2.2 as constants for the proposed equations were not available for R134a and Butane. The maximum heat transfer rates for different inclination angles are given by equation 6.40 and 6.41 and repeated for convenience by

$$\phi = 90^\circ \quad \dot{Q}_{\max} = 1.6553 \times 10^6 Bo^{0.3156} Ku^{1.6040} \quad (7.5)$$

$$\phi = 45^\circ \quad \dot{Q}_{\max} = 7.4685 \times 10^6 Bo^{0.2101} Ku^{1.9189} \quad (7.6)$$

Using the heat transfer mechanisms operating inside and across the walls of the thermosyphon, a simulation model could be developed for a single thermosyphon. From this single model, a HPHE model was developed utilizing thermosyphons as the primary heat transfer mechanism in the exchanger with different thermosyphon tube bank configurations. These tube bank configurations were modelled using theories proposed by Kröger (1998) which incorporate Colburn j-factors in the resistance models. This modelling technique was found to be sufficient as the theory used is well documented and has been in use for many years.

A HPHE was then designed using the mathematical simulation model in which the evaporator and condenser lengths were 0.204 m and the width was 0.306 m. Inside

temperature distribution experiments were conducted on this HPHE to investigate the effect that the individually manifolded rows would have on the HPHE operation. It was found that the temperatures at the top of the manifolded rows were on average 1.21 % lower than those temperatures at the bottom of the manifolded rows (see Figure 6.19). This indicates that the manifolding did in fact not influence the operation of the HPHE as the two-phase flow mechanisms were allowed to operate without hindrances. Uncertainties in the experimental results were found for an isolated experiment on this HPHE. Reasons for the errors might be incorrectly measured air stream velocities were the anemometer might not have been directly perpendicular to the flow field when measurements were taken. Thermocouple errors are ignored as additional experiments at different mass flow rates yielded satisfactory results. Figure 7.3 illustrates typical heat recoveries that can be obtained from the HPHE were  $\dot{Q}_{cond}$  represents the heat recovery and  $\dot{Q}_{evap}$  represents the heat input into the HPHE. These values are compared to those calculated using a mathematical model and a computer simulation code. The results showed that on average, the model under predicts the experimental values by 8 %. This error can be attributed to the fact that the model uses empirically determined values in order to calculate the heat transfer resistances.

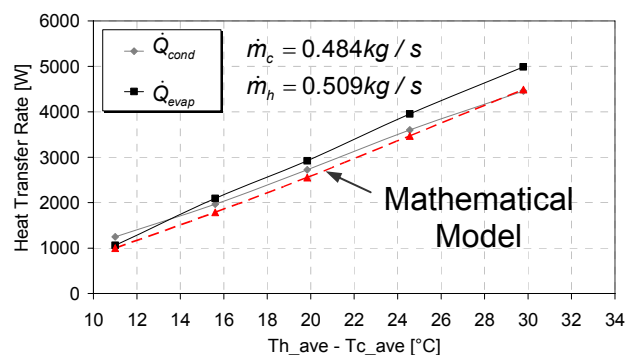


**Figure 7.3** Heat transfer rates for a HPHE at specified air mass flow rates compared to the mathematical model (copy of Figure 6.20b)

A demonstration HPHE was also designed using the mathematical model in which the evaporator and condenser lengths were 0.35 m and the width was 0.42 m. This demonstration HPHE was installed onto an existing air drier unit. Approximately 8.8 kW could be recovered from the CFW/Yucon HPHE for the hot waste stream of 0.55 kg/s at an inlet temperature of 51.64 °C with an outlet temperature of 35.9 °C in an environment of 20°C. It was also found that energy savings of 32.18 % could be achieved based on this heat recovery. The initial cost of the installation and manufacture of the HPHE was however higher than predicted and a payback period of 3.3 years for the demonstration

HPHE was calculated. This payback period will however decrease substantially should the HPHE be incorporated into the drier unit and mass production of this drier set-up be commenced.

Figure 7.4 illustrates the comparison between the mathematical model used in the computer simulation code to that of a set of data points taken from an experimental run on the demonstration HPHE. It was found that the mathematical model under predicted the actual heat transfer rate for lower temperature differences between the hot and cold air but that the error decreases with an increase in the aforementioned temperature difference. The percentage difference between the experimental results and the mathematical model were in the order of 11.7 % and it is felt that the computer code can therefore be used with confidence bearing in mind that the heat transfer resistances are calculated using empirically determined correlations.

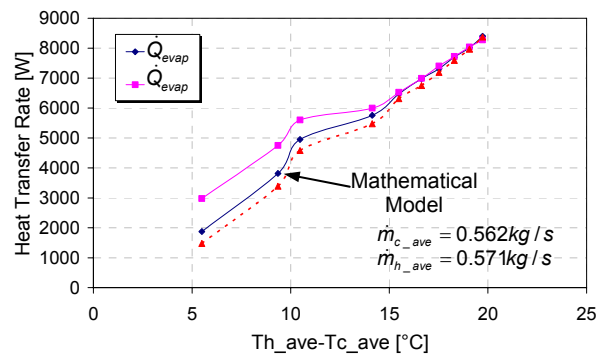


**Figure 7.4** Comparison between the mathematical model and the experimentally determined heat transfer rates for the CFW/Yucon HPHE (Copy of Figure 6.24)

A significant engineering contribution may be ascribed to the thesis in formulating equations for the heat transfer coefficients of R134a and Butane which were previously either non-existent or confined to specific situations. The demonstration HPHE yielded acceptable energy savings and the market is encouraged to utilize this heat exchanger type, to not only increase company profits, but also to protect and sustain the environment.



## 8 RECOMMENDATIONS

This section discusses the recommendations made for future work to be undertaken relating to this thesis. These recommendations are intended to serve as a starting point for further studies into thermosyphons and HPHEs. The following recommendations are made

1. The heat transfer coefficients formulated for this thesis were based on the variables such as the evaporator to condenser length ratio, the total length of the thermosyphon, the diameter and the liquid fill charge ratio which remained constant for all the experiments. Two orientation angles of vertical and  $45^\circ$  to the horizontal were investigated. It is recommended that different liquid fill charge ratios be investigated such that an optimum fill charge ratio can be determined. It is also recommended that a wider range of orientation angles and evaporator to condenser length ratios be investigated especially at inclination angles tending to zero.
2. The liquid fill charge ratios for the 5/8"-Thermosyphons should be re-evaluated as questionable results were obtained. It is suggested that numerous liquid fill charge ratios be used and the effect of this variable be identified specifically for the 5/8"-Thermosyphon and other thermosyphon of small diameters.
3. Two working fluid charging procedures were used in the experimental work. It is recommended that a device similar to the charging meter device described in Section 5.2.1 be used in future. Experimental experience verifies that this charging procedure provides for accurate liquid fill charge ratios.
4. The effect of different working fluids needs to be evaluated. It would be ideal if water were used as a working fluid and experimental procedures to charge the thermosyphon correctly with the water need to be investigated.
5. Adjustments need to be made to the HPHE computer program such that it will be user-friendly for a company such that a range of HPHE can be developed.

6. Inclining the HPHE at an optimum orientation angle needs to be investigated such that higher heat transfer rates can be achieved and hence greater energy savings be achieved.
7. A computational fluid dynamics (CFD) analysis can be used to investigate and predict the boiling nature of the working fluid inside thermosyphons. The CFD results can then be compared with the results presented in this thesis.

## 9 REFERENCES

Abou-Ziyan H.Z, Helali A, Fatouh M, Abo El-Nasr M.M, *Performance of a stationary and vibrated thermosyphon working with water and R134a*, Applied Thermal Engineering Vol. 21 (2001), pp 813-830

Akbarzadeh A, Johnson P, Nguyen T, Mochizuki M, Mashiko M, Sauciuc I, Kusaba S, Suzuki H, *Formulation and analysis of the heat pipe turbine for production of power from renewable sources*, Applied Thermal Engineering Vol. 21 (2001), pp 1551-1563

*ASHRAE Handbook Fundamentals*, American Society of Heating, Refrigeration and Air Conditioning Engineers, Inc, Atlanta, Ga, 2001

Colmac Coil Manufacturing Inc., Bulletin 2100, March 1, 2000, Revised

Dobson R.T and Kröger D.G, *Evaporator heat transfer coefficient and maximum heat transfer rate of an ammonia-charged inclined two-phased closed thermosyphon*, 11<sup>th</sup> Intl. Heat Pipe Conference, Tokyo, 12-16 September, 1999

Dobson R.T and Kröger D.G, *Thermal characterization of an ammonia charged two-phase closed thermosyphon*, 10<sup>th</sup> Int. Air Conditioning, Refrigeration & Ventilation Congress, Midrand, South Africa, 8-10 March 2000

Dobson R.T and Pakkies S.A, *Development of a heat pipe (two-phased closed thermosyphon) heat recovery heat exchanger for a spray drier*, Journal of Energy in Southern Africa, Vol. 13 No 4, November 2002

Dobson R.T and Pakkies S.A, *Development of an air-to-air R134a refrigerant charged two-phased closed thermosyphon heat exchanger*, 11<sup>th</sup> Int. Air Conditioning, Refrigeration & Ventilation Congress, Midrand, South Africa, 13-15 March 2002

Dobson R.T, *Design, manufacturing and testing of two-phased closed thermosyphons*, Refrigeration and Airconditioning, March 2000

Dobson R.T, *Fundamentals of Food Engineering for Food Scientists and Technologies*, Faculty of Engineering, University of Stellenbosch, 2001

Dobson R.T, *The features of two-phase closed thermosyphons*, Refrigeration and Airconditioning, September 1999

Dobson R.T, *The uses of closed two-phase thermosyphons*, Refrigeration and Airconditioning, September 1999

Dobson R.T, *Thermal characteristics of a two-phased closed thermosyphon*, Refrigeration and Airconditioning, January 2000, pp 55-59

Dunn D.P and Reay D, *Heat pipes*, 4<sup>th</sup> Edition, Pergamon, 1994

El-Genk M and Saber H.H, *Flooding limit in closed, two-phase flow thermosyphons*, Int. J. Heat Mass Transfer, Vol. 40 (1997), pp 2147-2164

Faghri A, *Heat pipe science and technology*, Taylor and Francis, 1995

Goldstick R, *The waste heat recovery handbook*, Fairmont Publishers, Atlanta, Ga, 1983

Groenewald A, *Thermal management of casting moulds using heat pipes*, University of Stellenbosch, 2001

Ivanovskii M.N, Sorokin V.P, Yagodkin I.V, *The physical principles of heat pipes*, Oxford University Press, New York, 1982

Johannsen A, *Equations and procedures for plotting psychometric charts in SI units by computer*, CSIR Report, ME 1711, Pretoria, May 1981

Joudi K.A and Witwit A.M, *Improvements of gravity assisted wickless heat pipes*, Energy Conversion and Management, Vol. 41 (2000), pp 2041-2061

Kays W.M and London A.L, *Compact heat exchangers*, McGraw-Hill Book Co., New York, 1984

Kröger D.G, *Air-cooled heat exchangers and cooling towers*, Department of Mechanical Engineering, University of Stellenbosch, 1998

Lock G.S.H, *The tubular thermosyphon—variations on a theme*, Oxford Science Publications, 1992

Lukitobudi A.R, Akbarzadeh A, Johnson P.W and Hendy P, *Design, construction and testing of a thermosyphon heat exchanger for medium temperature heat recovery in bakeries*, Heat Recovery Systems and CHP, Vol. 15, No. 5, pp 481-491, 1995

Maidment G.G and Eames I.W, *A summary of the proceedings of the UK Institute of Refrigeration 1998/1999*, International Journal of Refrigeration Vol. 24 (2001), pp 137-147

Mills A.F, *Heat and Mass Transfer*, Richard D. Irwin, Inc, 1995

Noie-Baghban S.H and Majideian G.R, *Waste heat recovery using a heat pipe heat exchanger (HPHE) for surgery rooms in hospitals*, Applied Thermal Engineering 20 (2000), pp 1271-1282

Nozu S, *Studies related to the heat pipe*, Trans. Soc. Mech. Engrs. Japan, 1969, 35 (2), pp 392-401

Nuntaphan A, Tiansuwan J, Kiatsiriroat T, *Enhancement of heat transport in thermosyphon air preheater at high temperature with binary working fluid: A case study of TEG-water*, Applied Thermal Engineering Vol. 22 (2002), pp251-266

Pan Y, *Condensation heat transfer characteristics and concept of sub-flooding in a two-phase closed thermosyphon*, Int. Comm. Heat Mass Transfer, Vol. 28 (2001), No. 3, pp 311-322

Pan Y and Wu C, *Numerical investigations and engineering applications on freezing expansion of soil restrained two-phase closed thermosyphons*, Int. J. Therm. Sci, Vol. 41 (2002), pp 341-347

Park Y.J, Kang H.K, Kim C.J, *Heat transfer characteristics of a two-phase closed thermosyphon to the fill ratio*, International Journal of Heat and mass transfer, Vol. 45 (2002), pp 4655-4661

Payakaruk T, Terdtoon P, Ritthidech S, *Correlations to predict heat transfer characteristics of an inclined closed two phase thermosyphon at normal operating conditions*, Applied Thermal Engineering Vol. 20 (2000), pp 781-790

Peterson G.P, *An introduction to heat pipes – modelling, testing and applications*, John Wiley and Sons, Inc, 1994

Pirol L.S, Pirol I.L, *Industrial two-phase thermosyphons*, Begell House, Inc, 1997

Russwurm A.E, *Q-pipes add a new dimension to waste heat recovery, Part 1*, Heating, Air Conditioning & Refrigeration (Now Refrigeration and Airconditioning, pp 27-39), January 1980

Sharma S.K, Mulvaney S.J, Rizvi S.S.H, *Food process engineering – theory and laboratory experiments*, John Wiley and Sons, Inc, 2000

Webb R.L, *Principles of enhanced heat transfer*, John Wiley and Sons, Inc, 1994

Whalley P.B, *Boiling, Condensation, and Gas-Liquid Flow*, Clarendon Press, Oxford, 1987

Wu X.P, Johnson P, Akbarzadeh A, *Application of heat pipe heat exchangers to humidity control in air-conditioning systems*, Applied Thermal Engineering, 17, (6), 1997, pp 561-568

Yang F, Yuan X, Lin G, *Waste heat recovery using heat pipe heat exchanger for heating automobile using exhaust gas*, Applied Thermal Engineering Vol. 23 (2003), pp 367-372

Yun J and Krolczek E, *Operation of capillary pumped loops and loop heat pipes*, Cooling zone online magazine, Vol 2, No 6, June 2002

Zhang H and Zhuang J, *Research, development and industrial application of heat pipe technology in China*, Applied Thermal Engineering Vol. 23 (2003), pp 1067-1083

# APPENDIX A: FLUID AND MATERIAL PROPERTIES

## A.1 Fluid Properties

In this thesis, two working fluids were utilized in the thermosyphons and the HPHE, namely, R134a and Butane. The properties of these fluids are temperature dependant in this thesis and equations describing their thermophysical properties follow. Properties for air and water are also given.

### A.1.1 R134a Refrigerant:

The properties for the refrigerant were obtained by providing trendlines that best fit data supplied by the ASHRAE Handbook (2001) and are evaluated with  $T$  in °C.

$$P = 1.27336 \times 10^{-5} T^3 + 1.33670 \times 10^{-3} T^2 + 1.04574 \times 10^{-1} T + 2.97586 \text{ [bar]} \quad (\text{A.1})$$

$$\rho_l = -2.20291 \times 10^{-7} T^5 + 3.00515 \times 10^{-5} T^4 - 9.62735 \times 10^{-4} T^3 - 2.55746 \times 10^{-2} T^2 - 2.67391 T + 1.29563 \times 10^3 \quad (\text{A.2})$$

$$\rho_v = 5.2867 \times 10^{-9} T^6 - 9.3605 \times 10^{-7} T^5 + 4.5222 \times 10^{-5} T^4 + 2.0343 \times 10^{-4} T^3 - 3.1541 \times 10^{-2} T^2 + 6.4911 \times 10^{-1} T + 18.605 \quad (\text{A.3})$$

$$h_{fg} = -6.1162 \times 10^{-7} T^6 + 1.0156 \times 10^{-4} T^5 - 4.6310 \times 10^{-3} T^4 - 4.1424 \times 10^{-2} T^3 + 1.3931 T^2 - 7.6453 \times 10^2 T + 1.9826 \times 10^5 \quad (\text{A.4})$$

$$Cp_l = 4.1336 \times 10^{-8} T^6 - 6.3941 \times 10^{-6} T^5 + 2.5375 \times 10^{-4} T^4 + 2.8582 \times 10^{-3} T^3 - 2.0274 \times 10^{-1} T^2 + 3.1241 T + 1.3576 \times 10^3 \quad (\text{A.5})$$

$$Cp_v = 6.5205 \times 10^{-8} T^6 - 1.0059 \times 10^{-5} T^5 + 3.9695 \times 10^{-4} T^4 + 4.5632 \times 10^{-3} T^3 - 3.2304 \times 10^{-1} T^2 + 4.5075 T + 9.1926 \times 10^2 \quad (\text{A.6})$$

$$\mu_l = 7.8165 \times 10^{-14} T^4 - 1.6631 \times 10^{-10} T^3 + 2.9178 \times 10^{-8} T^2 - 3.6401 \times 10^6 T + 2.8761 \times 10^{-4} \quad (\text{A.7})$$

$$\mu_v = 1.6052 \times 10^{-16} T^6 - 2.7076 \times 10^{-14} T^5 + 1.2383 \times 10^{-12} T^4 + 8.2196 \times 10^{-12} T^3 - 9.5238 \times 10^{-10} T^2 + 4.9261 \times 10^{-8} T + 1.1056 \times 10^{-5} \quad (\text{A.8})$$

$$k_i = 8.0932 \times 10^{-9} T^2 - 4.6109 \times 10^{-4} T + 9.3417 \times 10^{-2} \quad (\text{A.9})$$

$$k_v = 4.5014 \times 10^{-9} T^3 + 7.7319 \times 10^{-8} T^2 + 8.5865 \times 10^{-5} T + 1.1789 \times 10^{-2} \quad (\text{A.10})$$

$$\sigma = 1.6465 \times 10^{-9} T^3 + 8.8657 \times 10^{-8} T^2 - 1.4345 \times 10^{-4} T + 1.1735 \times 10^{-2} \quad (\text{A.11})$$

## A.1.2 Butane

Lighter fluid is used to represent butane for the experiments. The idea is that the lighter fluid would best approximate the properties of butane as butane in its purest form is expensive and difficult to obtain. The lighter fluid (manufactured by Newport Gas) however consists of a n-butane, iso-butane and propane mixture. The following table illustrates some of the differences in the thermophysical properties of these constituents and their mass fractions in the mixture at 30 °C.

**Table A.1** Thermophysical properties of lighter fluid mixture

	n-butane	iso-butane	Propane
$mf$ [%]	54	24	22
$P_{sat@30^\circ}$ [bar]	2.84	4.04	10.789
$\rho_l$ [kg/m <sup>3</sup> ]	566.8	544.3	484.4
$\rho_v$ [kg/m <sup>3</sup> ]	7.157	10.46	23.479
$h_{fg}$ [kJ/kg]	356.1	324.03	326.21
$C_{p_l}$ [kJ/kg]	2.479	2.489	2.803
$C_{p_v}$ [kJ/kg]	1.835	1.859	2.114
Molar Mass [kg/kmol]	58.124	58.12	44.097
Gas Constant, $R$ [kJ/(kmol.K)]	0.143	0.143	0.1885

To evaluate the mixture properties, gas mixture theory is used (Cengel and Boles, 1998). The mass of the fluid inside the container is weighed by weighing the can with and without



fluid in it, from which the weight of each component is determined as the mass fractions of each constituent are known. The mass of the fluid inside the container was measured to be 0.219 kg. The volumes of each of the constituents is then determined using

$$V_i = \frac{m_i R_i T}{P_i} \quad (\text{A.12})$$

Where  $i$  represents the individual fluids in the mixture. From these volumes, the total volume of the mixture is obtained

$$V_{tot} = \sum V_i \quad (\text{A.13})$$

The moles of each component are then calculated using

$$N_i = \frac{m_i}{M_i} \quad (\text{A.14})$$

From which the total number of moles for the mixture is obtained

$$N_{tot} = \sum N_i \quad (\text{A.15})$$

The mixture pressure is then obtained by

$$P_m = \frac{N_{tot} R_u T}{V_{tot}} \quad (\text{A.16})$$

The density, specific heat, enthalpies, dynamic viscosity and surface tensions of the mixture were all evaluated based on the mass fractions of the individual fluids. The thermal conductivity was based on the volume fractions of the individual fluids, where the volume fraction is given by

$$mv = \frac{\frac{mf_i}{\rho_i}}{\sum \frac{mf_i}{\rho_i}} \quad (\text{A.17})$$

And the density is calculated from (Dobson, )

$$\rho = \frac{1}{\sum \frac{mf_i}{\rho_i}} \quad (\text{A.18})$$

The properties for the lighter fluid were then obtained by providing trendlines that best fit the mixture data calculated from the thermophysical data sheets supplied by the ASHRAE handbook (2001). The properties are evaluated with  $T$  in °C.

$$P = 6.129 \times 10^{-6} T^3 + 6.728 \times 10^{-4} T^2 + 5.535 \times 10^{-2} T + 1.442 \text{ [bar]} \quad (\text{A.19})$$

$$\rho_l = -1.388 \times 10^{-4} T^3 + 1.077 \times 10^{-2} T^2 - 1.530 T + 5.807 \times 10^2 \quad (\text{A.20})$$

$$\rho_v = 3.310 \times 10^{-5} T^3 - 2.580 \times 10^{-4} T^2 + 1.758 \times 10^{-1} T + 3.377 \quad (\text{A.21})$$

$$h_{fg} = -1.063 \times 10^{-1} T^3 + 5.834 T^2 - 1.270 \times 10^3 T + 3.773 \times 10^5 \quad (\text{A.22})$$

$$Cp_l = 1.238 \times 10^{-4} T^4 - 1.745 \times 10^{-2} T^3 + 8.384 \times 10^{-1} T^2 - 7.533 T + 2.408 \times 10^3 \quad (\text{A.23})$$

$$Cp_v = 1.733 \times 10^{-4} T^4 - 2.434 \times 10^{-2} T^3 + 1.160 T^2 - 11.68 T + 1.743 \times 10^3 \quad (\text{A.24})$$

$$k_l = 1.105 \times 10^{-8} T^3 - 8.569 \times 10^{-7} T^2 - 4.047 \times 10^{-4} T + 1.116 \times 10^{-1} \quad (\text{A.26})$$

$$k_v = 2.186 \times 10^{-8} T^3 - 1.599 \times 10^{-6} T^2 + 1.54 \times 10^{-4} T + 1.394 \times 10^{-2} \quad (\text{A.25})$$

$$\mu_l = -5.800 \times 10^{-11} T^3 + 1.215 \times 10^{-8} T^2 - 1.882 \times 10^{-6} T + 1.783 \times 10^{-4} \quad (\text{A.26})$$

$$\mu_v = 3.515 \times 10^{-12} T^3 - 2.335 \times 10^{-10} T^2 + 3.573 \times 10^{-8} T + 6.991 \times 10^{-6} \quad (\text{A.27})$$

$$\sigma = 1.786 \times 10^{-7} T^2 - 1.267 \times 10^{-4} T + 1.339 \times 10^{-2} \quad (\text{A.28})$$

### A.1.3 Saturated Water Properties

The saturated water properties are used as functions of temperature in the thesis and are given by Kröger (1998). The temperatures are in degrees Kelvin.

$$cp_w = 8.15599 \times 10^3 - 2.80627 \times 10^1 T + 5.11283 \times 10^{-2} T^2 - 2.17582 \times 10^{-13} T^6 \quad (\text{A.29})$$

$$\rho_w = \left[ 1.49343 \times 10^{-3} - 3.7164 \times 10^{-6} T + 7.09782 \times 10^{-9} T^2 - 1.90321 \times 10^{-20} T^6 \right]^{-1} \quad (\text{A.30})$$

$$k_w = -6.14255 \times 10^{-1} + 6.9962 \times 10^{-3} T - 1.01075 \times 10^{-5} T^2 + 4.74737 \times 10^{-12} T^4 \quad (\text{A.31})$$

$$\mu_w = 2.414 \times 10^{-5} \times 10^{\frac{247.8}{(T-140)}} \quad (\text{A.32})$$

## A.1.4 Air Properties

The air properties were calculated at standard atmospheric pressure by fitting trendlines to the thermophysical properties of the air given by property tables in Mills (1995). The temperatures are given in Kelvin.

$$v_{air} = -8.473 \times 10^{-15} (T)^3 + 9.02 \times 10^{-11} (T)^2 + 3.942 \times 10^{-8} (T) - 3.993 \times 10^{-6} \quad (\text{A.33})$$

$$k_{air} = 1.714 \times 10^{-12} (T)^3 - 1.153 \times 10^{-8} (T)^2 + 7.049 \times 10^{-5} (T) - 6.476 \times 10^{-3} \quad (\text{A.34})$$

The specific heat of the of the air is given by Kröger (1998) and is evaluated in degrees Kelvin

$$cp_{air} = 1.045356 \times 10^3 - 3.16783 \times 10^{-1} T + 7.083814 \times 10^{-4} T^2 - 2.705209 \times 10^{-7} T^3 \quad (\text{A.35})$$

## A.2 Material Properties

The material properties were evaluated from Mills (1995) and were assumed to remain constant throughout the experiments.

### **A.2.1 Copper**

$$k_{copper} = 386$$

$$\varepsilon = 0.03$$

### **A.2.2 Stainless Steel**

$$k_{s/s} = 15$$

$$\varepsilon = 0.15$$

## APPENDIX B: SAMPLE CALCULATIONS

### B.1 Determination of the Inside Heat Transfer Coefficients

The experimental inside heat transfer coefficients are determined from the raw data values obtained for an experiment using a thermosyphon charged with a working fluid. For the sample calculations, a 3/4"-Thermosyphon is analysed at a data point having the readings given in Table B.1. The analysis for the heat transfer coefficients is given by Mills (1995).

**Table B.1** Data values for a 3/4"-Thermosyphon experiment

$T_{bottom}$	34.43	°C
$T_{top}$	33.479	°C
$T_{h,i}$	38.39	°C
$T_{h,e}$	38.02	°C
$T_{c,i}$	22.09	°C
$T_{c,e}$	22.458	°C
$\dot{m}_h$	0.435	kg/s
$\dot{m}_c$	0.3497	Kg/s
$d_i$	0.017272	m
$d_o$	0.01905	m
$d_{i,annulus}$	0.026543	m
$L_{evap}$	1.03	m

Dobson (2002) gives the equations formulated from a resistance model diagram to calculate the inside heat transfer coefficients for the evaporator and condenser sections

$$h_{ei} = \left[ A_{evap} \left( \frac{(T_{hw} - T_i)}{\dot{Q}_{evap}} - \frac{1}{h_{hw} A_o} - \frac{\ln(d_o/d_i)}{2\pi k L_{evap}} \right) \right]^{-1} \quad (B.1)$$

$$h_{ci} = \left[ A_{cond} \left( \frac{(T_i - T_{cw})}{\dot{Q}_{cond}} - \frac{1}{h_{cw} A_o} - \frac{\ln(d_o/d_i)}{2\pi k L_{cond}} \right) \right]^{-1} \quad (B.2)$$

Where  $A_{evap} = A_{cond} = \pi d_i L_{evap,cond} = \pi \times 0.017272 \times 1.03 = 5.59 \times 10^{-2} \text{ [m}^2\text{]}$

$$\text{And } A_o = \pi d_o L_{\text{evap,cond}} = \pi \times 0.01905 \times 1.03 = 6.16 \times 10^{-2} \text{ [m}^2\text{]}$$

The heat transferred to the thermosyphon and the heat removed from the thermosyphon are calculated from

$$\dot{Q} = \dot{m} c_p \Delta T \quad (\text{B.3})$$

With the values given in Table B.1

$$\dot{Q}_{\text{evap}} = 0.435 \times 4176 \times (38.39 - 38.02) = 660.9334 \text{ [W]}$$

$$\dot{Q}_{\text{cond}} = 0.3497 \times 4183 \times (22.458 - 22.09) = 532.145 \text{ [W]}$$

The heat loss from the thermosyphon to the atmosphere is then calculated using equation 5.4. For this calculation, the wall temperature is given as the average between the inlet and outlet water streams calculated to be 38.2 °C. From this, the heat loss is calculated as

$$Q_{\text{loss}_{-3/4''}} = 1.852 \times 10^{-3} (38.2 - 20)^2 + 0.3493 (38.2 - 20) - 0.6079 = 6.362 \text{ [W]}$$

The actual evaporator heat transfer rate is then given by

$$\dot{Q}_{\text{evap,actual}} = \dot{Q}_{\text{evap}} - \dot{Q}_{\text{loss}} = 660.933 - 6.362 = 654.56 \text{ [W]}$$

It is then necessary to calculate the heat transfer coefficients of the hot and cold water streams that flow through the heating and cooling jackets surrounding the thermosyphons. For this, the properties of the water streams must first be calculated. These properties are calculated at the bulk temperature between the inlet and outlet temperatures of the respective hot and cold water streams.

For the hot water temperature, the bulk temperature is given as

$$T_{\text{bulk,c}} = \frac{T_{h,i} + T_{h,e}}{2} \quad (\text{B.4})$$

$$T_{\text{bulk,c}} = \frac{38.39 + 38.02}{2} = 38.2 \text{ [}^\circ\text{C]}$$

And for the cold water temperature, the bulk temperature is given as

$$T_{\text{bulk,c}} = \frac{T_{c,i} + T_{c,e}}{2} \quad (\text{B.5})$$

$$T_{bulk,c} = \frac{22.09 + 22.458}{2} = 22.27 \text{ [}^\circ\text{C]}$$

The specific heats are then calculated using equation A.29 where the temperatures are in Kelvin. The values are calculated as

$$\begin{aligned} cp_{hw} &= 8.15599 \times 10^3 - 2.80627 \times 10^1 (38.20 + 273.15) + 5.11283 \times 10^{-2} (38.20 + 273.15)^2 \\ &\quad - 2.17582 \times 10^{-13} (38.20 + 273.15)^6 \\ &= 4176 \text{ [J/kg]} \end{aligned}$$

$$\begin{aligned} cp_{cw} &= 8.15599 \times 10^3 - 2.80627 \times 10^1 (22.27 + 273.15) + 5.11283 \times 10^{-2} (22.27 + 273.15)^2 \\ &\quad - 2.17582 \times 10^{-13} (22.27 + 273.15)^6 \\ &= 4183 \text{ [J/kg]} \end{aligned}$$

The densities of the hot and cold water streams are calculated using equation A.30 as

$$\begin{aligned} \rho_{hw} &= \left[ \frac{1.49343 \times 10^{-3} - 3.7164 \times 10^{-6} (38.2 + 273.15) + 7.09782 \times 10^{-9} (38.2 + 273.15)^2}{-1.90321 \times 10^{-20} (38.2 + 273.15)^6} \right]^{-1} \\ &= 993 \text{ [kg/m}^3\text{]} \end{aligned}$$

$$\begin{aligned} \rho_{cw} &= \left[ \frac{1.49343 \times 10^{-3} - 3.7164 \times 10^{-6} (22.27 + 273.15) + 7.09782 \times 10^{-9} (22.27 + 273.15)^2}{-1.90321 \times 10^{-20} (22.27 + 273.15)^6} \right]^{-1} \\ &= 997.67 \text{ [kg/m}^3\text{]} \end{aligned}$$

The thermal conductivities are calculated using equation A.31 as

$$\begin{aligned} k_{hw} &= -6.14255 \times 10^{-1} + 6.9962 \times 10^{-3} (38.2 + 273.15) - 1.01075 \times 10^{-5} (38.2 + 273.15)^2 \\ &\quad + 4.74737 \times 10^{-12} (38.2 + 273.15)^4 \\ &= 0.628 \text{ [W/mK]} \end{aligned}$$

$$\begin{aligned} k_{cw} &= -6.14255 \times 10^{-1} + 6.9962 \times 10^{-3} (22.27 + 273.15) - 1.01075 \times 10^{-5} (22.27 + 273.15)^2 \\ &\quad + 4.74737 \times 10^{-12} (22.27 + 273.15)^4 \\ &= 0.606 \text{ [W/mK]} \end{aligned}$$

The viscosities of the cold and hot water streams are calculated using equation A.32 as

$$\begin{aligned} \mu_{hw} &= 2.414 \times 10^{-5} \times 10^{\frac{247.8}{(38.2+273.15)-140}} \\ &= 0.000674 \end{aligned}$$

$$\begin{aligned}\mu_{cw} &= 2.414 \times 10^{-5} \times 10^{\frac{247.8}{(22.27+273.15)-140}} \\ &= 0.000949\end{aligned}$$

To calculate the hot and cold water stream heat transfer coefficients, the Nusselt numbers are given by the Dittus-Boelter and Gnielinski equations (Mills, 1995)

$$Nu_{Dh} = \frac{\left(\frac{f}{8}\right)(Re_{Dh} - 1000)Pr}{1 + 12.7\left(\frac{f}{8}\right)^{0.5}\left(Pr^{\frac{2}{3}} - 1\right)} \quad (B.6)$$

Where the Reynolds number is given by

$$Re_{Dh} = \frac{\rho V D_h}{\mu} \quad (B.7)$$

The velocities and hydraulic diameters are given by

$$V = \frac{\dot{m}}{\rho A} \quad (B.8)$$

$$D_h = 2(d_{i,annulus} - d_o) \quad (B.9)$$

$$D_h = 2(0.026543 - 0.01905) = 1.5 \times 10^{-2} \text{ [m]}$$

The area of the water flowing through the cooling jackets is then given by

$$A_w = \frac{\pi}{4} [d_{i,annulus}^2 - d_o^2] \quad (B.10)$$

$$A_w = \frac{\pi}{4} [0.026543^2 - 0.01905^2] = 2.68 \times 10^{-4} \text{ [m}^2\text{]}$$

The velocity values are then calculated as

$$V_h = \frac{0.435}{993 \times 2.68 \times 10^{-4}} = 1.632 \text{ [m/s]}$$

$$V_c = \frac{0.3497}{997.67 \times 2.68 \times 10^{-4}} = 1.306 \text{ [m/s]}$$

From which the Reynolds number are calculated as

$$Re_{Dh,h} = \frac{993 \times 1.632 \times 1.5 \times 10^{-2}}{0.000674} = 36033.2$$

$$Re_{Dh,c} = \frac{997.67 \times 1.632 \times 1.5 \times 10^{-2}}{0.000949} = 20590.94$$



The friction factor  $f$ , is given by

$$f = (0.79 \ln \text{Re}_{Dh} - 1.64)^{-2} \quad (\text{B.11})$$

And calculated as

$$f_h = (0.79 \ln 36033.2 - 1.64)^{-2} = 0.022$$

$$f_c = (0.79 \ln 20590.94 - 1.64)^{-2} = 0.025$$

The Prandtl numbers are calculated from

$$\text{Pr} = \frac{c_p \mu}{k} \quad (\text{B.12})$$

From which the values are calculated as

$$\text{Pr}_h = \frac{4176 \times 0.000674}{0.628} = 4.478$$

$$\text{Pr}_c = \frac{4183 \times 0.000949}{0.606} = 6.54$$

The Nusselt numbers are then calculated using equation B.6 as

$$\text{Nu}_{Dh,h} = \frac{\left(\frac{0.022}{8}\right)(36033.2 - 1000)4.478}{1 = 12.7 \left(\frac{0.022}{8}\right)^{0.5} \left(4.478^{\frac{2}{3}} - 1\right)} = 205.435$$

$$\text{Nu}_{Dh,c} = \frac{\left(\frac{0.025}{8}\right)(20590.94 - 1000)6.54}{1 = 12.7 \left(\frac{0.025}{8}\right)^{0.5} \left(6.54^{\frac{2}{3}} - 1\right)} = 148.14$$

The water heat transfer coefficients are then calculated from

$$h_w = \frac{\text{Nu}_{Dh} k_w}{D_h} \quad (\text{B.13})$$

With the values calculated as

$$h_{hw} = \frac{205.435 \times 0.628}{1.5 \times 10^{-2}} = 8620.248 \text{ [W/m}^2\text{K]}$$

$$h_{hw} = \frac{148.14 \times 0.606}{1.5 \times 10^{-2}} = 5996.591 \text{ [W/m}^2\text{K]}$$

Manipulating the above calculated values into equations B.1 and B.2, yields the inside heat transfer coefficients for the evaporator and condenser sections as

$$h_{ei} = \left[ 5.59 \times 10^{-2} \left( \frac{(38.2 - 33.95)}{654.56} - \frac{1}{8620.248 \times 6.16 \times 10^{-2}} - \frac{\ln(0.01905/0.017272)}{2\pi \times 386 \times 1.03} \right) \right]^{-1}$$

$$= 3914.05 \text{ [W/m}^2\text{K]}$$

$$h_{ci} = \left[ 5.59 \times 10^{-2} \left( \frac{(33.95 - 22.27)}{532.145} - \frac{1}{5996.591 \times 6.16 \times 10^{-2}} - \frac{\ln(0.01905/0.017272)}{2\pi \times 386 \times 1.03} \right) \right]^{-1}$$

$$= 931.492 \text{ [W/m}^2\text{K]}$$

## B.2 Determination of the Theoretical Thermosyphon Heat Losses

The theoretical thermosyphon heat losses are calculated using natural convection and radiation theory (Mills, 1995). For the analysis, the thermosyphon is assumed to be a vertical wall. The heat losses were calculated at an ambient temperature of 20 °C. The wall temperature was calculated as the average between the inlet and outlet temperatures of the hot water flowing through the cooling jacket and is given by

$$T_w = \frac{T_{h,i} + T_{h,e}}{2} \quad (\text{B.14})$$

The mean temperature is given by the average between the wall and ambient temperatures

$$T_m = \frac{T_w + T_{amb}}{2} \quad (\text{B.15})$$

For the heat loss calculations, the data values for the 3/4" thermosyphon given by Table B.1 are used. From this, the wall and mean temperatures are calculated using equations B.13 and B.14, respectively. The air properties are calculated at the mean temperature.

$$T_w = \frac{38.39 + 38.02}{2} = 38.2 \text{ [}^\circ\text{C]}$$

$$T_m = \frac{38.02 + 20}{2} = 29.1 \text{ [}^\circ\text{C]}$$

For the natural convective heat transfer coefficients, equations 3.45 and 3.46 are used were for laminar flow,  $R_{aL} \leq 10^9$

$$\bar{N}_{uL} = 0.68 + 0.67(R_{aL}\psi)^{1/4} \quad (\text{B.16})$$

And for turbulent flow  $10^9 \leq R_{aL} < 10^{12}$

$$\bar{N}_{uL} = 0.68 + 0.67(R_{aL}\psi)^{1/4} (1 + 1.6 \times 10^{-8} R_{aL}\psi)^{1/12} \quad (\text{B.17})$$

With

$$\psi = \left[ 1 + \left( \frac{0.492}{Pr} \right)^{9/16} \right]^{-16/9} \quad (\text{B.18})$$

The Rayleigh number is given by

$$Ra = \frac{\beta(T_w - T_{amb})gL_{evap}^3}{\nu^2} Pr \quad (\text{B.19})$$

The dynamic viscosity of the air is calculated using equation A.33 as

$$\begin{aligned} \nu_{air} &= -8.473 \times 10^{-15} (29.1 + 273.15)^3 + 9.02 \times 10^{-11} (29.1 + 273.15)^2 \\ &\quad + 3.942 \times 10^{-8} (29.1 + 273.15) - 3.993 \times 10^{-6} \\ &= 1.5927 \times 10^{-5} \text{ [m}^2/\text{s]} \end{aligned}$$

The Rayleigh number is then calculated as

$$\begin{aligned} Ra &= \frac{(1/(29.1 + 273.15))(38.20 - 20) \times 9.81 \times 1.03^3}{(1.5927 \times 10^{-5})^2} \times 0.69 \\ &= 1.755 \times 10^9 \end{aligned}$$

The dimensionless parameter is calculated as

$$\begin{aligned} \psi &= \left[ 1 + \left( \frac{0.492}{0.69} \right)^{9/16} \right]^{-16/9} \\ &= 0.3426 \end{aligned}$$

Where the Prandtl number is given by 0.69. From the Rayleigh number and equation B.17, the Nusselt number is calculated as

$$\begin{aligned}\bar{N}_{uL} &= 0.68 + 0.67 \left( 1.755 \times 10^9 \times 0.3426 \right)^{1/4} \left( 1 + 1.6 \times 10^{-8} 1.755 \times 10^9 \times 0.3426 \right)^{1/2} \\ &= 144.91\end{aligned}$$

The outside convection heat transfer coefficient is then calculated from

$$h_c = \left( \frac{k_{air}}{L_{evap}} \right) \bar{N}_{uL} \quad (\text{B.20})$$

Where the thermal conductivity of air is calculated using equation A.34 as

$$\begin{aligned}k_{air} &= 1.714 \times 10^{-12} (29.1 + 273.15)^3 - 1.153 \times 10^{-8} (29.1 + 273.15)^2 \\ &\quad + 7.049 \times 10^{-5} (29.1 + 273.15) - 6.476 \times 10^{-3} \\ &= 0.0267 \text{ [W/mK]}\end{aligned}$$

The convective heat transfer coefficient is calculated as

$$h_c = \left( \frac{0.0138}{1.03} \right) 144.91 = 3.338 \text{ [W/m}^2\text{K]}$$

For the radiative heat transfer coefficient, the following equation is used

$$h_r = 4\varepsilon\sigma(T)^3 \quad (\text{B.21})$$

Where  $\varepsilon$  is the emissivity of the wall material and  $\sigma = 5.67 \times 10^{-8}$ . The heat transfer coefficient is then calculated as

$$h_r = 4 \times 0.03 \times 5.67 \times 10^{-8} (29.1 + 273.15)^3 = 0.187 \text{ [W/m}^2\text{K]}$$

The heat loss to the environment is then calculated using

$$\begin{aligned}\dot{Q}_{loss} &= \left[ \frac{1}{UA} \right]^{-1} (T_w - T_{amb}) \\ &= \left[ \frac{1}{(h_c + h_r)A} \right]^{-1} (T_w - T_{amb})\end{aligned} \quad (\text{B.22})$$

With the necessary convective and radiative heat transfer coefficients, the heat loss is calculated as

$$\dot{Q}_{loss} = \left[ \frac{1}{(3.338 + 0.187)\pi \times 0.026} \right]^{-1} (38.2 - 20) = 3.956 \text{ [W]}$$

### B.3 Determination of the Theoretical HPHE Heat Losses

For the determination of the HPHE heat losses to the environment, similar convection theories are used as those in Section B.2. Radiative heat losses were omitted from these calculations as it was felt that the effect of the radiative heat transfer coefficient in this analysis is negligible. For this analysis, the heat losses were divided into those from the manifolds and those from the side walls of the casing of the HPHE. This theoretical heat loss determination is also used for the heat loss calculations on the CFW/Yucon HPHE with the adjustments made for the different geometries. Table B.2 illustrates the temperatures and geometries for the calculation of the heat loss from the laboratory tested HPHE. For the heat loss calculations, the ambient temperature is given as 20 °C.

**Table B.2** Data values for the laboratory HPHE experiments

$T_{h,i}$ [°C]	47.81	$V_{cold}$ [m/s]	3.28
$T_{h,e}$ [°C]	38.64	$V_{hot}$ [m/s]	3.86
$T_{c,i}$ [°C]	16.57	$L_{casing}$ [m]	0.2345
$T_{c,e}$ [°C]	25.54	$W_{casing}$ [m]	0.100

The wall and mean temperatures are calculated using equations B.14 and B.15, respectively. The air properties are calculated at the mean temperature.

$$T_w = \frac{47.81 + 38.64}{2} = 43.23 \text{ [°C]}$$

$$T_m = \frac{43.23 + 20}{2} = 31.62 \text{ [°C]}$$

The dynamic viscosity of the air is calculated using equation A.33 as

$$\begin{aligned} \nu_{air} &= -8.473 \times 10^{-15} (31.62 + 273.15)^3 + 9.02 \times 10^{-11} (31.62 + 273.15)^2 \\ &\quad + 3.942 \times 10^{-8} (31.62 + 273.15) - 3.993 \times 10^{-6} \\ &= 1.6145 \times 10^{-5} \text{ [m}^2/\text{s]} \end{aligned}$$

The Rayleigh number is calculated for the manifold using equation B.19 with the evaporator length substituted by the diameter of the manifold

$$Ra = \frac{(1/(31.62 + 273.15))(43.23 - 20) \times 9.81 \times 0.01905^3}{(1.6145 \times 10^{-5})^2} \times 0.69$$

$$= 1.368 \times 10^4$$

The Rayleigh number for the side wall of the HPHE casing is calculated using equation B.19

$$Ra = \frac{(1/(31.62 + 273.15))(43.23 - 20) \times 9.81 \times 0.2345^3}{(1.6145 \times 10^{-5})^2} \times 0.69$$

$$= 2.552 \times 10^7$$

The dimensionless parameter is calculated as

$$\psi = \left[ 1 + \left( \frac{0.492}{0.69} \right)^{9/16} \right]^{-16/9}$$

$$= 0.3426$$

Where the Prandtl number is given by 0.69. The Nusselt number for the manifold is calculated from

$$N_{uD} = 0.36 + \frac{0.518 R_{aD}^{0.25}}{\left[ 1 + \left( \frac{0.559}{Pr} \right)^{9/16} \right]^{4/9}} \quad (B.23)$$

And the Nusselt number for the side walls of the HPHE casing calculated using equation B.16. Manipulating the calculated Rayleigh numbers into equation B.16 and B.23, the Nusselt numbers for the casing walls and manifolds are calculated as

$$\bar{N}_{uL,casing} = 0.68 + 0.67 \left( 2.552 \times 10^7 \times 0.3426 \right)^{1/4} \left( 1 + 1.6 \times 10^{-8} 2.552 \times 10^7 \times 0.3426 \right)^{1/12}$$

$$= 37.51$$

$$N_{uD,manifold} = 0.36 + \frac{0.518 (1.368 \times 10^4)^{0.25}}{\left[ 1 + \left( \frac{0.559}{0.69} \right)^{9/16} \right]^{4/9}}$$

$$= 4.58$$

The outside convection heat transfer coefficient is then calculated from

$$h_c = \left( \frac{k_{air}}{L_{evap}} \right) \bar{N}u_L \quad (B.24)$$

Where the thermal conductivity of air is calculated using equation A.34 as

$$\begin{aligned}
k_{air} &= 1.714 \times 10^{-12} (31.62 + 273.15)^3 - 1.153 \times 10^{-8} (31.62 + 273.15)^2 \\
&\quad + 7.049 \times 10^{-5} (31.62 + 273.15) - 6.476 \times 10^{-3} \\
&= 0.0269 \text{ [W/mK]}
\end{aligned}$$

The convective heat transfer coefficient for the manifolds is calculated as

$$h_c = \left( \frac{0.0269}{0.01905} \right) 4.58 = 6.467 \text{ [W/m}^2\text{K]}$$

And the convective heat transfer coefficient for the casing walls is calculated as

$$h_c = \left( \frac{0.0269}{0.2345} \right) 37.51 = 4.302 \text{ [W/m}^2\text{K]}$$

The heat loss from the manifolds is then calculated using

$$\begin{aligned}
\dot{Q}_{loss, manifold} &= N_r h_c A (T_w - T_{amb}) & \text{(B.25)} \\
&= 3 \times 6.467 \times \pi \times 0.01905 \times 0.362 (43.23 - 20) = 9.76 \text{ [W]}
\end{aligned}$$

The heat loss from the casing walls is then calculated using

$$\begin{aligned}
\dot{Q}_{loss, casing} &= h_c A (T_w - T_{amb}) & \text{(B.26)} \\
&= 4.302 \times 0.2345 \times 0.1 (43.23 - 20) = 2.343 \text{ [W]}
\end{aligned}$$

And there are two side walls, thus the heat loss from the casing walls is 4.686 W. The total heat loss for the laboratory HPHE is then given by

$$\begin{aligned}
\dot{Q}_{loss, total} &= \dot{Q}_{loss, manifold} + \dot{Q}_{loss, casing} & \text{(B.27)} \\
&= 9.76 + 4.686 = 14.44 \text{ [W]}
\end{aligned}$$

# APPENDIX C: COMPUTER SIMULATION PROGRAMS

A HPHE computer simulation program and an air drier simulation program were developed from the theoretical modelling presented in Section 3. The HPHE computer program is used to simulate the sizing of a HPHE such that a required heat recovery can be obtained. The drier computer program is used to simulate a variety of drying applications. The flow diagram for the HPHE computer simulation program is presented in Section 4. The operational procedures for these two computer simulation programs are discussed in this Appendix.

## C.1 HPHE Computer Simulation Program

Once the program has been started, the main window appears. This window consists of the physical inputs window, the tube bank configuration window, the results window and the visualisation of the flow pattern window. Figure C.1 illustrates the main window.

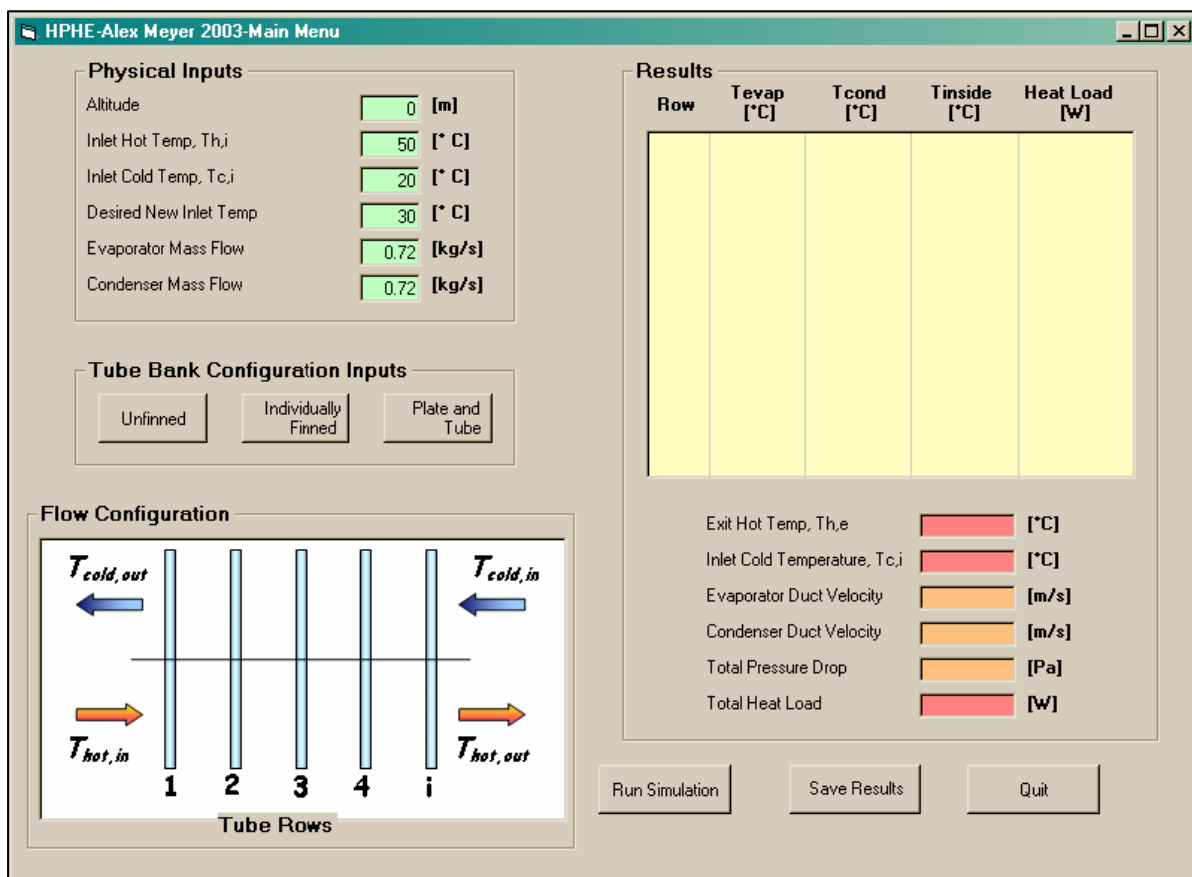


Figure C.1 Main window for the HPHE computer program



The following steps are then followed

## Step 1

This step involves assigning the physical inputs to the flow problem. From Figure C.2, it can be seen that the physical inputs include the inlet hot and cold temperatures that enter the HPHE in °C. The altitude is also entered in such that the correct pressures and densities can be calculated. The desired outlet temperature of the cold air stream is then entered in. This temperature represents the temperature of the air that is being heated by the HPHE. The air mass flows for the hot and cold streams that flow through the evaporator and condenser sections of the HPHE are then entered in. These values are in kg/s.

Physical Inputs		
Altitude	<input type="text" value="0"/>	[m]
Inlet Hot Temp, $T_{h,i}$	<input type="text" value="50"/>	[°C]
Inlet Cold Temp, $T_{c,i}$	<input type="text" value="20"/>	[°C]
Desired New Inlet Temp	<input type="text" value="30"/>	[°C]
Evaporator Mass Flow	<input type="text" value="0.72"/>	[kg/s]
Condenser Mass Flow	<input type="text" value="0.72"/>	[kg/s]

**Figure C.2** Physical inputs for the HPHE computer program

## Step 2

This step involves deciding which tube bank configuration is to be used for the HPHE. The three options include: unfinned thermosyphon tubes, individually finned thermosyphon tubes or a plate-and-tube configuration. For these configurations, it is important to note the transverse and longitudinal pitches of the core configuration. These pitches represent the distances of the tubes from each other in the longitudinal and transverse directions. The unfinned thermosyphon tubes consist of an array of thermosyphon that are either aligned or staggered. Figure C.3 illustrates the window that appears when the “unfinned” button is clicked.

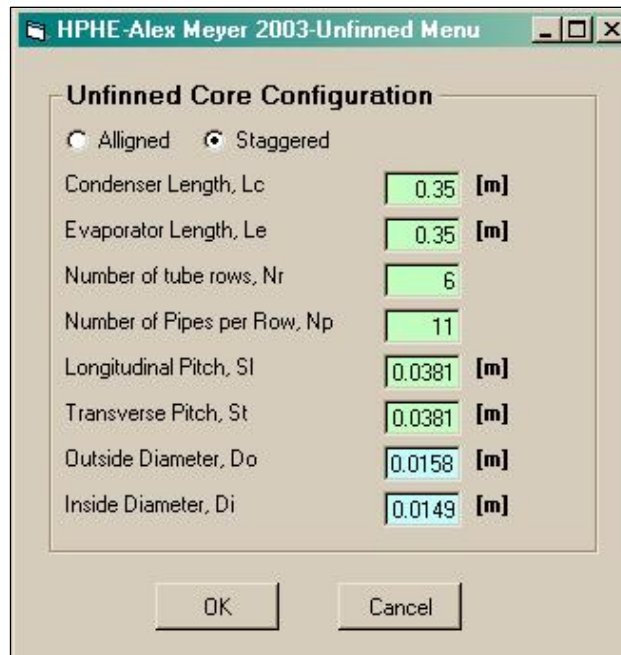


**Figure C.3** Unfinned thermosyphon tube bank configuration for the HPHE computer program

The individually finned thermosyphon configuration consists of an array of individually finned thermosyphons. It is general practice to use the staggered configuration as this yields higher heat transfer rates as a larger surface area is exposed to the flow stream. Figure C.4 illustrates the window that appears when the “Individually Finned” button is clicked.

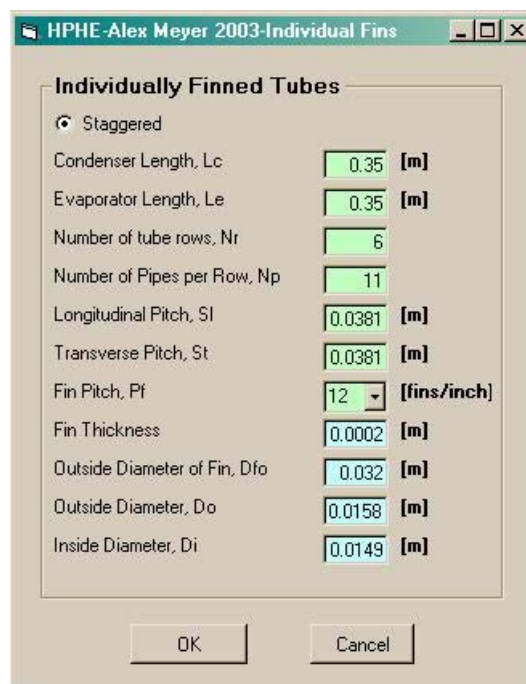


**Figure C.4** Individually finned thermosyphon tube bank configuration for the HPHE computer program

The plate-and-tube configuration consists of an array of annular finned tubes in which the fins are made of plates that are separated by spacers from each other. The array of tubes can be either aligned or staggered, however, only the staggered configuration is considered here as this yields higher heat transfer rates. Figure C.5 illustrates the window that appears when the “Plate-and-Tube” button is clicked.

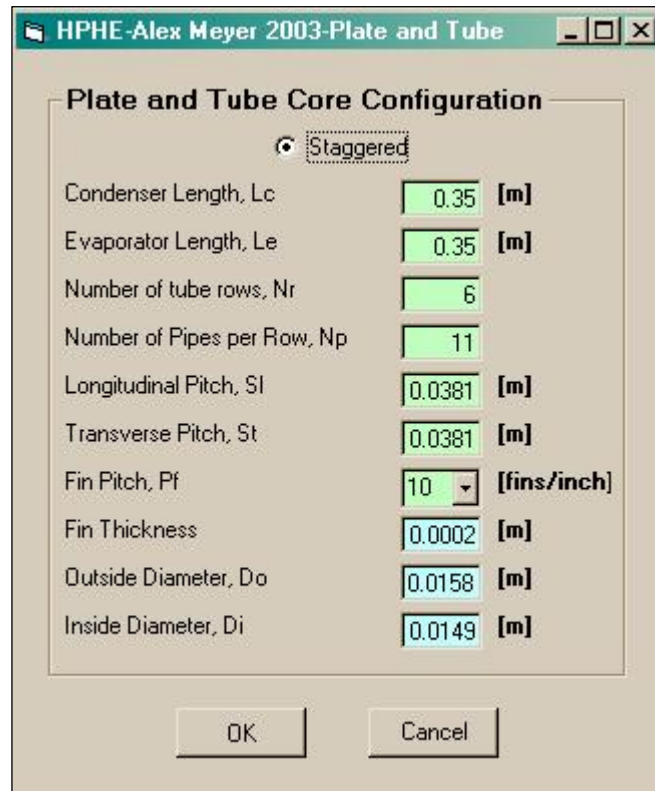


**Figure C.5** Plate-and-tube bank configuration for the HPHE computer program

It is important that a tube bank configuration is chosen for the simulation. Should this not be chosen and the “Run” button entered, a error window appears warning the user that a tube bank configuration has as yet not been chosen. Figure C.6 illustrates the error window.

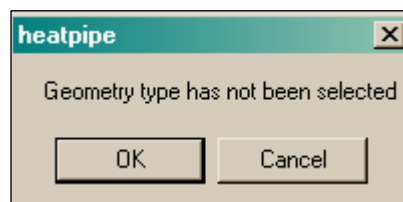


**Figure C.6** Error window for the HPHE computer program

### Step 3

This step involves starting the computer simulation. The “Start” button is then clicked and the simulation begins. This simulation can only commence once the physical inputs have been entered in and the tube bank configuration chosen. Figure C.7 illustrates the window that appears with the results. The row for row temperatures are given with the accompanying heat transfer rates for each row. The total heat transfer rate for the HPHE is then calculated and shown along with the pressure drop across the HPHE. The calculated inlet and outlet temperatures are then also presented. A visual representation of the temperatures is given in the flow configuration window.

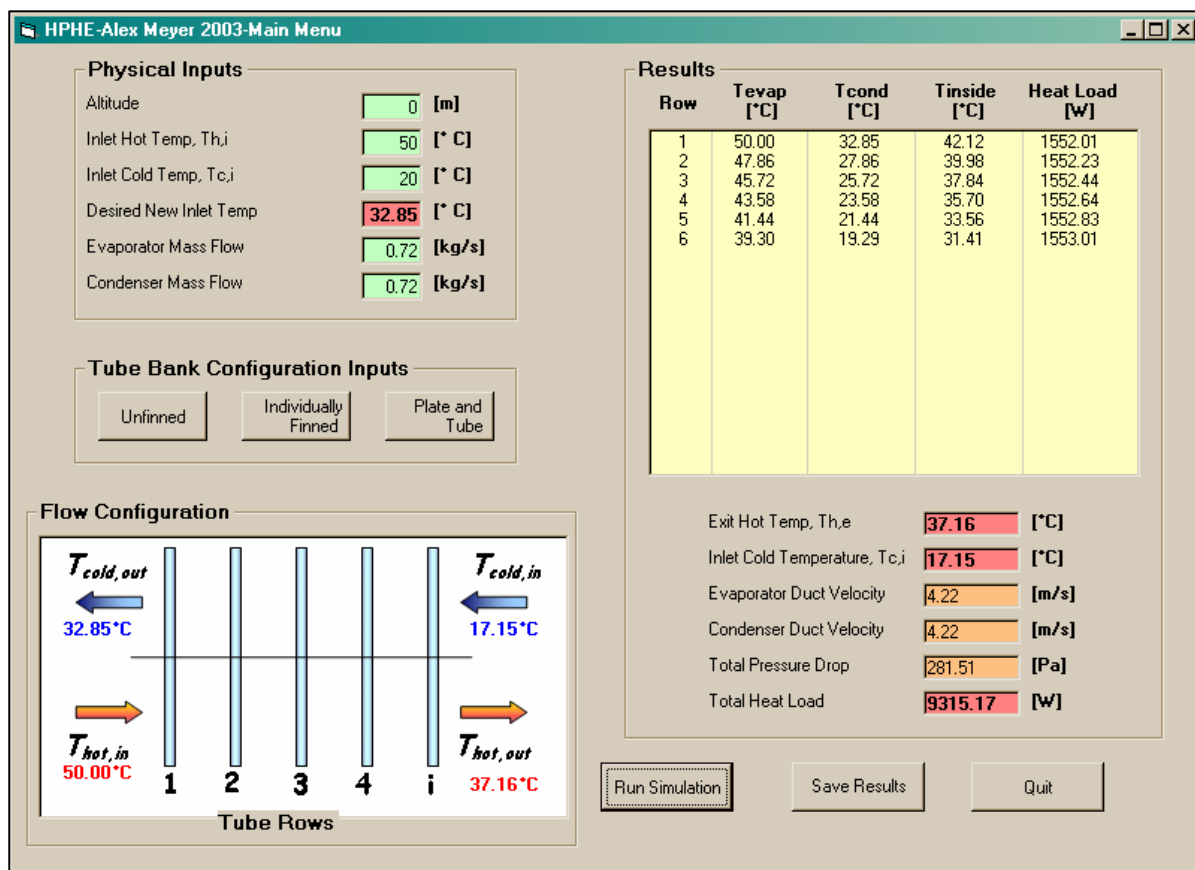
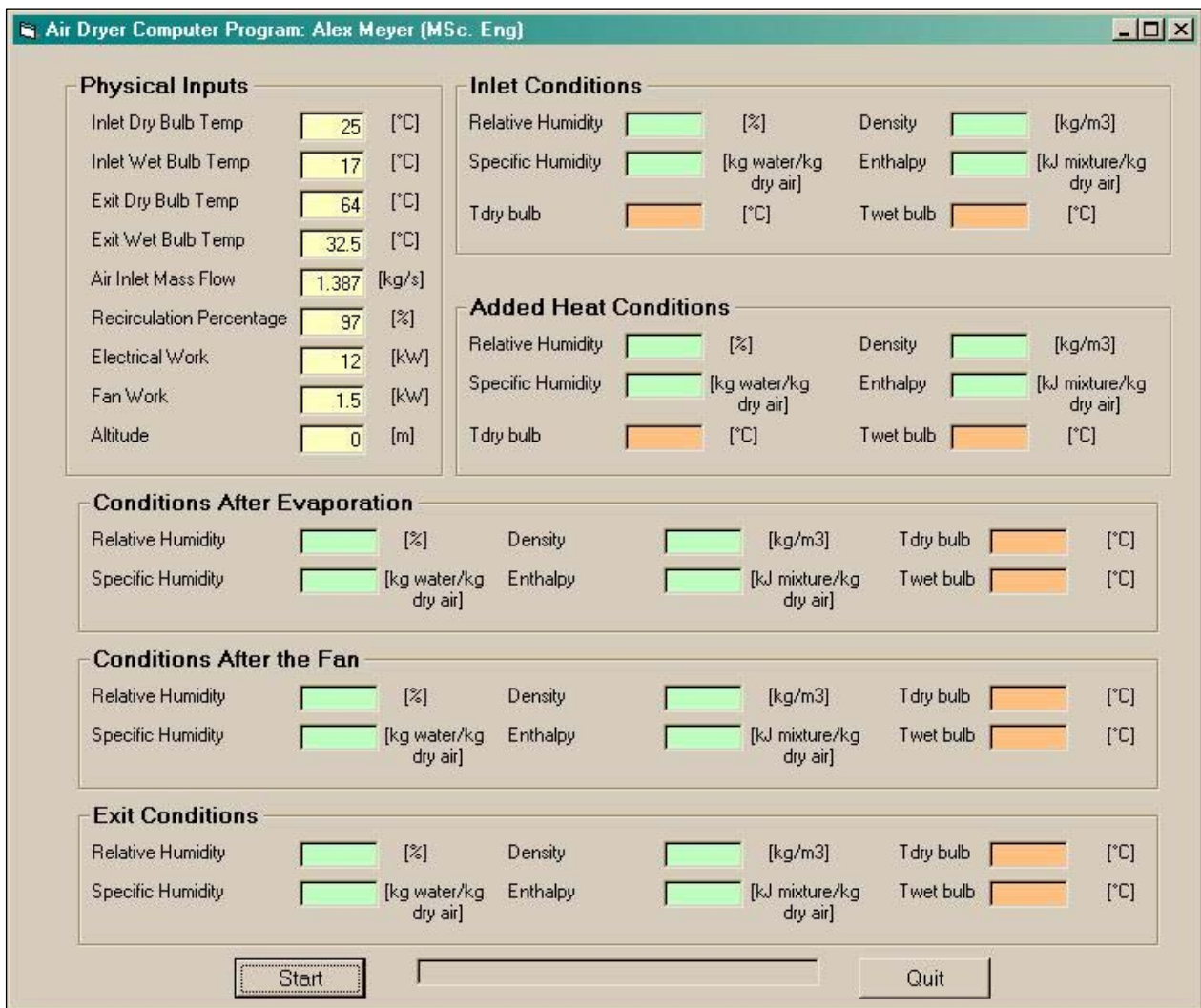


Figure C.7 Results window for the HPHE computer program

Should the temperatures or total heat transfer rate not comply with the design specifications, steps two through three are then repeated with different geometry sizes entered in for the tube bank configuration windows. This is an iteration process to obtain the required heat transfer rate and the user soon develops a feel for the sizes of the HPHE and the time to size a HPHE shortens.

## C.2 Air Drier Computer Simulation Program

Once the program has been started, the main window appears. This window consists of the physical inputs window and the results of the temperatures and relative and specific humidity's at the various stages in the drier unit. These stages are represented in Figure 3.7. Figure C.8 illustrates the main window.



**Figure C.8** Main window for the air drier computer program

The first step and only step in this computer simulation program is to define the physical inputs for the start-up of the drier. These variables include the inlet wet and dry bulb temperatures, the exiting wet and dry bulb temperatures, the inlet air mass flow rate, the recirculation percentage of the air in the drier unit and the electrical and fan work that is supplied to the air stream. The global positioning of the drier with respect to altitude is also

entered in. Figure C.9 illustrates the physical inputs window. The “Start” button is then clicked and the results window appears. From the window, the various properties of the air can be investigated. Figure C.10 illustrates the results window.

Physical Inputs		
Inlet Dry Bulb Temp	25	[°C]
Inlet Wet Bulb Temp	17	[°C]
Exit Dry Bulb Temp	64	[°C]
Exit Wet Bulb Temp	32.5	[°C]
Air Inlet Mass Flow	1.387	[kg/s]
Recirculation Percentage	97	[%]
Electrical Work	12	[kW]
Fan Work	1.5	[kW]
Altitude	0	[m]

Figure C.9 The physical inputs window for the air drier computer program

Physical Inputs		
Inlet Dry Bulb Temp	25	[°C]
Inlet Wet Bulb Temp	17	[°C]
Exit Dry Bulb Temp	64	[°C]
Exit Wet Bulb Temp	32.5	[°C]
Air Inlet Mass Flow	1.387	[kg/s]
Recirculation Percentage	97	[%]
Electrical Work	12	[kW]
Fan Work	1.5	[kW]
Altitude	0	[m]

Inlet Conditions		
Relative Humidity	44.743	[%]
Density	1.167	[kg/m <sup>3</sup> ]
Specific Humidity	0.00887	[kg water/kg dry air]
Enthalpy	47.717	[kJ mixture/kg dry air]
T dry bulb	25.0	[°C]
T wet bulb	17.0	[°C]

Added Heat Conditions		
Relative Humidity	13.277	[%]
Density	1.025	[kg/m <sup>3</sup> ]
Specific Humidity	0.01798	[kg water/kg dry air]
Enthalpy	108.769	[kJ mixture/kg dry air]
T dry bulb	61.47	[°C]
T wet bulb	31.896	[°C]

Conditions After Evaporation		
Relative Humidity	14.074	[%]
Density	1.012	[kg/m <sup>3</sup> ]
T dry bulb	64.087	[°C]
Specific Humidity	0.02159	[kg water/kg dry air]
Enthalpy	120.932	[kJ mixture/kg dry air]
T wet bulb	33.951	[°C]

Conditions After the Fan		
Relative Humidity	9.724	[%]
Density	0.987	[kg/m <sup>3</sup> ]
T dry bulb	72.541	[°C]
Specific Humidity	0.02159	[kg water/kg dry air]
Enthalpy	129.76	[kJ mixture/kg dry air]
T wet bulb	35.39	[°C]

Exit Conditions		
Relative Humidity	12.016	[%]
Density	1.017	[kg/m <sup>3</sup> ]
T dry bulb	64.0	[°C]
Specific Humidity	0.01827	[kg water/kg dry air]
Enthalpy	112.133	[kJ mixture/kg dry air]
T wet bulb	32.5	[°C]

Start [Progress Bar] Quit

Figure C.10 Results window for the air drier computer program

# APPENDIX D: DETAIL HPHE DRAWINGS

# APPENDIX E: RAW DATA SETS